CALIFORNIA STATE UNIVERSITY NORTHRIDGE

FACIES AND DEPOSITIONAL HISTORY OF ARC-RELATED, DEEP-MARINE VOLCANICLASTIC ROCKS IN CORE RECOVERED ON INTERNATIONAL OCEAN DISCOVERY PROGRAM EXPEDITION 351, PHILIPPINE SEA

A thesis submitted in partial fulfillment of the requirements
for the degree of Master of Science
in Geology

By

Kyle E. Johnson

May 2016

The thesis of Kyle E. Johnson is approved:

_____	_____
Philipp A. Brandl, Dr. rer. nat.	Date
_____	_____
Richard V. Heermance, Ph.D.	Date
_____	_____
Kathleen M. Marsaglia, Ph.D., Chair	Date

California State University, Northridge

ACKNOWLEDGMENTS

I would like to extend my sincere thanks to my committee members Dr. Kathleen Marsaglia, Dr. Richard Heermance, and Dr. Philipp Brandl for their time, support, and input through the writing of this thesis.

I especially extend deep gratitude to Dr. Kathleen Marsaglia for accepting me as a graduate student and for her diligence in the procurement of funding. This thesis would not be possible without the guidance she provided and the undying patience she exhibited. I will be forever grateful for the skill sets and behaviors she has helped me develop, including leadership, research and organizations skills, as well as attentiveness to detail and overall professionalism. Without the work of Dr. Philipp Brandl and other shipboard scientists, as well as CSUN student Ryan Waldman, this project would not have been possible. Dr. Richard Heermance's input, patience, and availability are also greatly appreciated.

I would also like to thank the National Science Foundation and the Geological Society of America for their financial support, and the faculty and staff of the CSUN Department of Geological Sciences for sharing their knowledge in the classroom. Last, but not least, I am grateful for all my friends and fellow students at CSUN, my parents, Carol and Mark back home in Oregon, and my sister, Kirsten and her family in North Carolina for providing much needed emotional support and encouragement when I needed it most.

Table of Contents

ABSTRACT

FACIES AND DEPOSITIONAL HISTORY OF ARC-RELATED,
DEEP-MARINE VOLCANICLASTIC ROCKS IN CORE RECOVERED
ON INTERNATIONAL OCEAN DISCOVERY PROGRAM
EXPEDITION 351, PHILIPPINE SEA

By

Kyle E. Johnson

Master of Science in Geology

The Izu-Bonin-Mariana (IBM) Arc System, south of Japan, hosts a multitude of active and extinct (remnant) volcanic arcs and associated basins partly filled with volcanic sediment. Core extracted adjacent to the proto-IBM arc (Kyushu-Palau Ridge; KPR), in the Amami-Sankaku Basin (ASB) during International Ocean Discovery Program (IODP) Expedition 351, contains an incredibly well-preserved record of backarc sedimentation resulting from changing tectonic regimes during arc development and decline. Approximately 1000 meters of Eocene to Oligocene volcaniclastic sedimentary rocks were analyzed via shipboard core photos, core descriptions, and thin sections with the intention of understanding the depositional history at this site. A database of stratigraphic columns, 539 section and 147 core summaries, was created to display grain size trends, sedimentary structures, bedding characteristics, and facies changes. Individual depositional events were classified using existing and slightly modified classification schemes for muddy, sandy, and gravel-rich gravity flow deposits, as well as muddy deposits and tuffs. Analyzing trends and distributions of depositional unit types indicates how the active depositional systems evolved upsection as the arc matured. Following arc initiation, facies deposited were primarily mud-rich; these coarsened-upward into 12 stacked sequences of submarine lobe and channel facies with sediment from one or more volcanic sources. These are

interpreted to represent the building of the arc edifice that began ~41 Ma. Four distinct periods of coarse lobe accumulation created a thick submarine fan over a period of nearly 13 million years. An abrupt shift to muddy turbidites at ~30 Ma represents the onset of rifting of the paleo-IBM arc as backarc spreading in the Shikoku Basin was initiated and volcaniclastic supply to the ASB waned with formation of the KPR remnant arc.

Introduction

The Philippine Sea, south of Japan (Figure 1), hosts a multitude of active and extinct (remnant) arc volcanic sediment sources associated with the Izu-Bonin-Mariana (IBM) Arc System. The IBM Arc, which marks the eastern edge of the Philippine Sea, is the result of subduction of the oceanic Pacific Plate under the oceanic Philippine Sea Plate. Subduction initiation occurred at ~52 Ma, which was concurrent with a major change in Pacific Plate motion (Arculus et al., 2015a). Rifting of the active volcanic arc took place at ~25 Ma and was followed by seafloor spreading and eastward migration of the active volcanic front (Arculus et al., 2015a). In intraoceanic settings, rifting and seafloor spreading produces a basin flanked by a remnant arc and an active arc (e.g., Tamaki and Honza, 1991; and Marsaglia and Devaney, 1995; Figure 2). In the IBM Arc, rifting formed the Shikoku-Parece Vela Basin and the inactive (remnant arc) Kyushu-Palau Ridge (KPR) (Ishizuka et al., 2011).

The backarc basin of the paleo-IBM Arc, prior to rifting, was the Amami Sankaku Basin (ASB) (Tamaki and Honza, 1991), located to the west of the KPR. In 1996, reconnaissance of the seafloor crust of the ASB was the target of a Shinkai 6500 submersible dive. Lithologies were identified and sampled along a one-kilometer-high escarpment along the western boundary of the ASB. Bioturbated ash turbidites, altered tuffs, calcareous chalk, scoria, and basalt breccia were identified and sediment samples were predominantly pelagic mud (Arculus et al., 2015a). Thus the ASB contains a sedimentological record of the paleo-IBM Arc.

In 2014 several IODP expeditions (350, 351, 352) explored the IBM arc system to answer questions about intra-oceanic arc initiation and development utilizing the Joides Resolution ocean-drilling research vessel (e.g., Tamura et al., 2013). In May 2014, Expedition 351 set out to drill and sample oceanic crustal remnants and 1-1.5 km of sediment that preserves development

of the IBM arc from a backarc perspective. The primary objectives of Expedition 351 were to: 1) characterize the oceanic basement to infer mantle geochemistry prior to IBM arc inception, and 2) recover cover-sequence volcaniclastic sediments that contain records of pre-IBM history, IBM arc inception, and arc growth (Arculus et al., 2015a). Objective 2 is the focus of this study.

IODP Expedition 351 drilled at Site U1438 (Figure 1) to a depth of 1.61km through 1.46 km of volcaniclastic sediment overlying oceanic crust in the ASB. Multiple coring methods were utilized during Expedition 351, each denoted by a letter in the core naming scheme (Arculus et al., 2015b): advanced piston corer (H), half-length advanced piston corer (F), extended core barrel (X), and rotary core barrel (R). About 1.15 km of core was recovered from four holes (U1438A, U1438B, U1438D, and U1438E; Figure 3). This sediment, shed from the evolving magmatic arc, contains a record of the earliest stages of arc inception and evolution (Arculus et al., 2015c, 2015d).

Shipboard scientists logged changes in grain size, texture, color, gross lithology, nature of bedding contacts, and sedimentary structures at a cm-scale for each sediment-bearing core. Information was entered into the DESClogik database and exported into a series of Microsoft Excel spreadsheets (Arculus et al., 2015b). These data were used alongside quantitative measurements to define four sedimentary lithostratigraphic units (I, II, III, IV) (Figure 3a; Arculus et al., 2015c). Sedimentary Unit I (0-160.3 meters below the seafloor (mbsf)) comprises mainly hemipelagic mud with minor ash beds, whereas Sedimentary Units II (160.3-309.6 mbsf), III (309.6-1361.4 mbsf) and IV (1361.4-1461.1 mbsf) are dominated by coarser (sand-gravel), marine volcaniclastic sediments. Sediment accumulation rates were estimated as having decreased from ~120 m/my in Units II and III (Eocene to Oligocene) to ~5 m/my in Unit I (Miocene to Holocene) (Arculus et al., 2015c). In sum, Site U1438 represents one of the most

complete deep-marine records of island arc evolution, with sedimentary records from Early Eocene subduction initiation to Late Oligocene and Early Miocene arc rifting.

Background on Backarc Basin Sedimentation

Much of what is known about the sedimentary record of intraoceanic arcs in outcrop comes from a few ancient examples where they have been accreted to continent margins or otherwise uplifted and exposed (e.g., Marsaglia, 1995). For example, Cedros Island, Mexico, contains an unusually well preserved and exposed intraoceanic-backarc basin fill of Jurassic age. Being proximal to the arc front, the section contains a high content of basalt and tuffs and a low content of volcaniclastic turbidites (Busby-Spera, 1987). Northland, New Zealand, provides another good stratigraphic record of the submarine volcaniclastic apron associated with a Tertiary arc volcano (Allen et al., 2007). Allen et al. (2007) divided volcanic and sedimentary units into four categories: proximal apron – comprising breccia-conglomerate, coarse lapillistone, pillow lava, and megabreccia; medial apron – comprising conglomerate, pillow lava, mudstone, and sandstone; distal apron – comprising fine and medium sandstone, tuff, and conglomerate; and channel – comprising pebbly sandstone. Note that neither Busby-Spera (1987) nor Allen et al. (2007) elaborated on distal basinal records.

Backarc basins are among the least-understood basin types due modern counterparts being entirely submarine (Marsaglia, 1995). Our knowledge of modern backarc basins has therefore been obtained through geophysical data (bathymetry, seismic surveys, etc.) and sedimentological data (dredging, piston cores, and deep-sea drilling) (Marsaglia, 1995). Most backarc basins are concentrated on the western side of the Pacific Ocean where ocean drilling has uncovered backarc basin sedimentary sequences that would otherwise be inaccessible; drawbacks include low recovery of volcaniclastic units and poor penetration. Despite these drawbacks, Ocean Drilling Program (ODP) expeditions in backarc basins (starting with Legs 124 to 135, 1988-1991) have greatly expanded knowledge and refinement of previous models based

on Deep Sea Drilling Project (DSDP) coring of the Mariana System (Marsaglia, 1995). For example, Klein (1985) documented characteristics of nine major sediment types from DSDP cores in backarcs of the West Pacific and discovered the following facies proportions: 1.2% debris flows, 20% submarine fan systems, 5.7% basinal turbidites, 22% hemipelagic clays, 4.2% pelagic clays, 4.3% biogenic siliceous sediments, 24% biogenic carbonates, 9.5% resedimented carbonates, and 9.5% pyroclastics. He did not place these facies into a larger-scale depositional model. Later work by ODP Leg 126 shipboard scientists (e.g., Taylor et al., 1990; Hiscott et al., 1992) focused more on arc-axis and forearc successions.

Objectives of This Study

Arculus et al. (2015a) hypothesized that Unit III at Site U1438 represents the post-subduction-initiation arc development and the Unit III-II boundary represents the rifting of the paleo-IBM Arc, which separated the remnant arc (Kyushu Palau Ridge) from the modern IBM via seafloor spreading. This was based on shipboard core descriptions including a rolling-average grain size distribution for the cored interval (Figure 3a), as well as broad age correlations (Arculus et al., 2015a). Detailed facies analyses and depositional process interpretations performed during this study test their hypotheses, as well as provide a complete and detailed picture of arc development during deposition of Unit III. This study, based on a single drill-site perspective, characterizes the depositional unit style and architecture of a distal backarc sedimentary succession, a setting not previously studied in detail.

Methods

Thin Sections

One-hundred-sixty-six quarter-cut core samples of sandy units were selected shipboard, approximately one per core, to represent the stratigraphic section. A rock saw was utilized to create billets that were shipped to National Petrographic Service, Inc. in Houston, Texas in two batches for blue-epoxy impregnation and thin section creation.

Stratigraphic Columns

Illustrated stratigraphic columns were produced from the Unit II-IV sediment recovered at Site U1438 (Figure 3a), first at the section scale (Figure 3c) and then at the core scale (Figure 3b) starting from igneous basement (Core U1438B-69R) and working up the section. Thicker beds present at the top of Unit III and structurally complex intervals at the Unit II/III boundary made the shorter section columns less informative, so starting at Core U1438D-48R (~660 mbsf) and continuing up through Core U1438B-18H, only summaries at the core scale were produced. Hole E cores U1438E-4R to -6R overlap with Hole D cores U1438D-70R to -72R. Due to less core disruption, the latter, Hole D cores, were used for this study.

Stratigraphic columns at the section and core scale were constructed based on slabbed core images taken shipboard, data in the DESClogik database exported to Microsoft Excel and single-page core summaries (Arculus et al., 2015b), as well as shipboard notes taken by Dr. Kathleen Marsaglia during periods when multiple cores were laid out for visual inspection during several shipboard "sampling parties." Shipboard core images may be accessed via the IODP LIMS Report website (http://web.iodp.tamu.edu/UWQ). Cores were scanned, producing images at the ~1.5m section-scale. Recovered core segments within each 9.5 m core interval

were pushed to the top, which means gaps in recovery can be cryptic unless represented by abrupt lithologic changes across a segment gap. Additional textural information at discrete intervals within sandy units was garnered from petrographic examination of the 166 thin sections. Adobe Illustrator CS5.1 was used to combine these data into an easy-to-read page format at the section and core scale (Figure 3b and 3c).

The illustrated width of the core interval (horizontal scale in Figures 3b and 3c) represents grain size within the core. Symbols for depositional unit contacts and sedimentary and tectonic structures were placed in the column; these are defined in Figure 4, in a system modeled after IODP Expedition 351 shipboard descriptions (Arculus et al., 2015b). There are no symbols used for inverse or normal grading as these are indicated by changes in profile (grain size) as illustrated in Figure 4.

Two classification schemes were applied to the core, one broad (facies) and the other more detailed (bedding/depositional units) that are described below. Facies subdivisions and bed-scale intervals were often bounded by bedding planes but in some instances boundary relationships were masked by diagenetic overprinting, drilling deformation and/or gaps in recovery. A column on the left of each diagram (see supplemental material file) includes facies classifications, whereas depositional classifications are indicated on the right at the bottom or middle of individual depositional units. Interpretations were made using core images and, when required, petrographic analysis of thin sections. Distinction between mudstone and siltstone was based primarily on visual interpretations made by shipboard scientists and their input into the DESClogik database.

Facies Classification

Sequences of beds portrayed on the stratigraphic columns were first classified into a number of facies categories (Table 1). The comprehensive deep-water-sediment classification scheme developed by Pickering et al. (1986) and Pickering and Hiscott (2016) was used in a simplified version of its original form. In this scheme, the term disorganized refers to non-laminated and ungraded facies and the term organized refers to laminated or graded facies. Some additional classes were newly defined in Site U1438 cores, such as D2.4 and D2.5. Classes are designated by prefixes associated with grain size: "A" for gravel and pebbly sand classes, "B" for sand classes, "C" for sand and mud couplet classes, "D" for silt classes, and "E" for mud and clay classes (Pickering et al., 1986). Following the prefix is a two-part number code. The first number is a "1" or "2", the former representing disorganized beds and the latter representing organized beds. Next, after a decimal point, is a second number that has different meanings for each prefix (Table 1).

Depositional Unit Description

In addition to intervals of hemipelagic sediment accumulation that dominate Unit I, Site U1438 cores contain several depositional unit types associated with gravity flow or pyroclastic processes (Figure 5). Grain size variations and sedimentary structures were the main criteria used to help differentiate which type of depositional mechanism to which each unit belonged. Once the broad category was determined (e.g., turbidite, sandy/muddy debris flow, or tuff), more specific classification schemes were applied. For example, three turbidite classification options were used, each associated with different grain-size distributions reflecting different flow densities. These classification schemes, which are standards used in the literature, are elaborated on below.

Medium-grained turbidites (classic turbidites) were classified (Figure 5) using the Bouma Sequence (Figure 6b) divisions (Bouma, 1962) as a root with hyphenated supplements for maximum grain size and deposit thickness: T(Bouma divisions)-(maximum grain size)-(deposit thickness). The supplements, maximum grain size (mud, silt, sand, or gravel) and deposit thickness, are defined in Table 2. For example, Tacde-G-5 refers to a deposit exhibiting Bouma divisions a, c, d, and e, with a maximum grain size of granule, and a thickness between 30 centimeters and 100 centimeters.

Fine-grained turbidites, resulting from low-density turbidity currents, were classified (Figure 5) according to Stow and Shanmugam (1980) who separate Bouma's Tc, Td, and Te divisions into nine detailed subdivisions designated T_0-T_8 (Figure 6a). The T_0 division correlates to the Bouma Tc division, the T_1-T_5 divisions correlate with the Bouma Td division, and the T_6-T_8 divisions correlate to the Bouma Te division. The T_0 division contains basal lenticular lamination, and the T_1-T_5 divisions transition up from well-developed convolute bedding, to irregular laminations and regular laminations, then to indistinct laminations. The T_6-T_8 divisions transition from graded mud and silt, up into ungraded mud and silt, and finally into ungraded and bioturbated mud. Above T_8 in section is hemipelagic bioturbated sediment, which in this study is simply grouped with "T_8". The divisions are used in a similar way to those of the classic turbidites described above, where the divisions present are displayed, i.e. T_{3568}, and supplements of maximum grain size and deposit thickness (Table 2) are added: T(divisions)-(maximum grain size)-(deposit thickness). For example, T_{3568}-Si-3 refers to a deposit exhibiting T_3, T_5, T_6, and T_8 divisions, a maximum grain size of silt and a total thickness between 5 centimeters and 10 centimeters. A complete sequence was very rarely observed; instead, partial sequences were

more common, referred to as top-absent, base-absent, and middle-absent based on the absence of Te, Tc, or Td Bouma divisions, respectively, as defined by Pickering et al. (1986).

Coarse-grained turbidites, resulting from high-density turbidity currents, were classified (Figure 5) using the Lowe (1982) "S" or "R" prefixes and divisions (Figure 6c). Bouma division "Ta" is generally equivalent to Lowe division "S_3". S_3 is a massive, graded, and suspension-sourced gravel and sand division with dish structures. S_2 is gravel and sand oriented as a traction carpet. S_1 is also a result of traction but has more organized coarse grains. Below S_3-S_1 is a sequence of gravel-sized divisions, labeled R_3-R_1, that are rarely in sequence with S_3-S_1 due to movement of the flow dispersing gravel-sized clasts more proximally than sand-sized grains. R_3-R_1 are described similar to S_3-S_1 but lack sandy matrix and have larger gravel clasts. In this study coarse-grained turbidites were classified similarly to classic turbidites but using the Lowe divisions instead of Bouma division: S/R(Lowe divisions)-(maximum grain size)-(deposit thickness). For example, S_{12}-G-6 is a coarse-grained turbidite sequence with Lowe divisions S_1 and S_2, maximum grain size of gravel, and a total thickness of greater than 100 centimeters.

Debris flow deposits were classified (Figure 5) based on criteria outlined in Boggs (2012). The scheme developed for this study uses a prefix of "D" followed by a subscripted number denoting characteristics: a "D_1" represents a debris flow that is primarily sand with sparse floating gravel clasts, a "D_2" represents flows that have more gravel than sand but are not necessarily clast-supported (Figure 6e), a "D_3" represents inversely-graded debrites, and a "D_4" represents the normally-graded tops of debris flows. Following the prefix are the two supplements, maximum grain size and bed thickness (Table 2). D($_1$, $_2$, or $_3$)-(maximum grain size)-(bed thickness). For example, D_2-G-4 is an unorganized gravel-rich debris flow deposit with a thickness between 10cm and 30cm. Note that the proportion of mud in these deposits was

very hard to visually estimate by shipboard scientists and in core images owing to post-depositional alteration of volcanic components and cementation.

Mud/mudstone beds were classified (Figure 5) using prefix of "M" followed by a subscripted number that represents bedding characteristics. A "$_1$" denotes structureless mud and a "$_2$" represents structureless mud with unorganized floating gravel-sized clasts (Figure 6d). Following the prefix, the two supplements maximum grain size and bed thickness are added to all previous schemes (Table 2): M(number)-(maximum grain size)-(bed thickness). For example, M_2-G-5 is a bed, 30-100cm thick, that consists of structureless mud with gravel-sized clasts. Note that the M_2 bed designation may be considered a mudflow deposit with an emplacement mechanism more similar to the D units described above. In addition, the structureless M_1 beds may be a product of thorough bioturbation.

Tuff/Lapillistone was classified using the prefix "V" with an added subscripted number that corresponds to grading (Figure 5): "$_1$" represents ungraded (massive), "$_2$" represents normally graded, and "$_3$" represents inversely graded, i.e. V_1, V_2, V_3 (Figure 6f). Akin to the previous schemes, two suffixes are added based on maximum grain size and bed thickness (Table 2), e.g., V($_1$, $_2$, or $_3$ for grading)-(maximum grain size)-(bed thickness). For example, V_1-Si-4 refers to a tuffaceous bed/interval that is ungraded, has a maximum grain size of silt, and has a thickness of 10-30cm.

Lobe and Channel Facies Classification

Using the stratigraphic summary columns, 100 m-scale lobe system charts were constructed by graphically illustrating changes in gravity flow depositional unit type: fine-grained turbidites (no Bouma Ta or Tb divisions present), medium-grained turbidites (Bouma Tb

division present but no Ta division), coarse-grained turbidites (Bouma Ta and/or any Lowe divisions present), and debrites (debris flow deposits). Each depositional unit was assigned a specific grayscale color, where the darker the gray the coarser-grained the depositional unit type. Patterns within the stratigraphic columns and the depositional unit distribution were correlated to submarine channel and lobe facies described by Mutti and Normark (1987; Figure 7) and fan models as summarized by Covault (2011; Figure 8).

Results

Stratigraphic Columns

Section columns, 539 in total ranging up to 150cm in length, were constructed (see Figure 3c for an example) and will be made available via online data report published through IODP (Johnson et al., in prep.). In constructing columns, recognizing bedding planes was problematic in some intervals owing to unrecovered contacts and breaks in cores as described in the Methods section. Several intervals were significantly altered which also impeded column construction. The section columns for each core were combined into core summary columns (147 total) that are presented in a Supplemental Material file. Thirteen Unit IV core summary columns, slightly modified from Waldman (2015), were included here for completeness. They are the focus of a more detailed study in progress (Waldman et al., in prep.). No detailed columns were constructed for Unit I as it consisted mainly of hemipelagic mud.

Grain sizes of individual beds were described in the DESClogik database. Thin section observations made in this study were consistent with shipboard analyses of thin sections, which indicated that the sand to gravel-sized sediment was volcaniclastic in origin. As individual stratigraphic columns were finished, facies classes introduced by Pickering and Hiscott (1986) were applied to the appearance of beds. A simplification was made to better apply to the interpretation of depositional processes in this study. This simplification disregarded specific differences in grading (taken into account by depositional unit classification), and internal structures (taken into account by symbols (Figure 4)). Once depositional unit classification schemes were determined (Figure 5), they were applied to groups of beds using structures, contacts, and lithologies identified within the core images. A few beds and groups of beds did not fit into any scheme and were left out of interpretations. Beds were often too disturbed (by

drilling and/or soft-sediment deformation) to confidently determine deposit type; these were classified as having "disrupted bedding."

Downhole Distributions

To better illustrate downhole trends in these cores, several summary columns were constructed (Figure 9). The grain size distribution for each core was created by tabulating for each core the total length of recovered core comprising each lithology. These proportions were plotted on a 100% stacked plot to visualize distributions. The dominant grain size for each bed was used rather than the largest grain size, which was used in the depositional unit classification scheme. Within Unit IV and between 1460 and 1200 mbsf within Unit III, mud and sand are the dominant grain sizes. Abruptly starting at 1200 mbsf, silt and gravel dominate with a lower sand content and diminished mud content. Above, mud and sand again dominate in Unit II.

To formulate a facies class distribution plot (Figure 9) elements of each facies class (A, B, C, D, and E) listed in Table 1 were grouped as disorganized or organized. Details can be found in the Figure 9 figure caption. The total thickness representing each class present in each core summary column was tabulated and recalculated to 100%; then the plot for each core's distribution was stacked to visualize their distribution in the section. In Unit IV and below 1200 mbsf in Unit III, Facies Classes C (organized sand and mud couplets) and E (mud) dominate, with organized mud more common below 1300 mbsf. This is the only interval where Facies Class C is notable. The lowest half of this interval is rich in Facies Class E2.1 (laminated mud) while the top has significant Facies Class E1.1 (structureless mud). Above 1200 mbsf, Facies Class D (silt), B (sand), and A (gravel) are dominant, and class A yields to class D in fine intervals. From ~ 575-500 mbsf, a high proportion of Facies Class E is again present before the Facies Class A-dominated interval that precedes the Unit III-II boundary. Within Unit II, Facies

Class E (mud) and B (sand) dominate and there is a varying amount of class Facies Class D (silt).

Proportions of depositional unit types were tabulated on a core-by-core basis and plotted on a 100% stacked plot for visualization (Figure 9). In Unit IV and below 1200 mbsf in Unit III, turbidites are dominant. Exceptions are tuff intervals within cores U1438E-47R and U1438E-42R. Above 1200 mbsf debrites and coarse-grained turbidites are introduced and vary in proportion until the Unit III-II boundary. Intervals of solely turbidites exist within intervals that contain debrites. Unit II contains turbidites that progressively yield to a content of tuff and hemipelagic mudstone up section. Overall percentages of each type are as follows: ~57% turbidites (fine- and medium-grained), ~31% debrites, ~3% coarse-grained turbidites, ~2% tuff/lapillistone, and ~1% structureless mud deposits.

Stratigraphic Subunit Designations for Units IV and III

Shipboard scientists placed the Unit IV-III boundary at the first downhole occurrence of a thick mudstone interval below the thick interval of debrite and turbidite in U1438E-55R-3. Unit IV is distinguished by a significant radiolarian content in the top 50 meters of the unit. Waldman et al. (in prep.) distinguished this as Subunit IV-A, which contains thin and medium fine-grained turbidites. The underlying interval (Subunit IV-B) is characterized by fine-grained turbidites that contain minimal sand, while the thin Subunit IV-C is mainly hemipelagic mudstone. Note that Waldman's subunit designators follow the format of IODP where A equals the youngest and then designators progress through the alphabet with increasing relative age. This format was continued into Units III and II.

As the thickest of the Site U1438 units (1052.33 meters), Unit III contains the most variety of depositional unit characteristics. Unit III is distinguished from Unit IV in that it contains fine-, medium-, and coarse- grained turbidites, as well as debrites in coarsening-upward packages.

Whereas shipboard scientists did not attempt to subdivide this thick unit into subunits, the detailed data collected in this study facilitated subunit divisions. Following the illustration and interpretation of all the cores, core summary columns for Units III and II were printed and combined end-to-end forming a 25-m long high-resolution stratigraphic log. Large-scale subunits could then be discerned based on changes in grain size, bedding, facies classes, and depositional unit types present. Unit III is distinguished by periodic pulses of debrites. Debrite-rich and debrite-poor subunits generally alternate. Unit III subunits are broadly based on relative debrite versus turbidite content, where intervals of cores containing debrites were grouped together. Each debrite-rich subunit contains a gradual buildup of debrite content and thickness before dropping abruptly – which defines the upper contact of the subunits. Debrite-poor subunits may contain tuff beds, mudstone beds, and isolated debrites, but the dominant depositional units are turbidites. Throughout Unit III sediment accumulation rate varied but peaked at significant occurrences of debrites. Unit III is divided into twelve subunits, labelled "III-L" to "III-A" from oldest to youngest as summarized in Table 3 and Figure 9. These are described in detail below:

III-L: Cores U1438E-55R to -50R; 1361.88-1312.0 mbsf

Subunit III-L is composed of thin sand to mud turbidites (Figure 10a; Table 3) and scattered intervals of hemipelagic mudstone (Figure 10b). Drilling brecciation and disturbance were common, so intact bedding contacts were not often recognizable. Apparent depositional unit (turbidite) thicknesses are less than ten centimeters, the thinnest of all Unit III subunits. The

dominant facies class, from Pickering et al. (1986) is C-class (Table 1), more specifically C2.2 (sand and mud couplets 10-30 cm thick) and C2.3 (sand and mud couplets <10 cm), with thicknesses decreasing up section within the Subunit. Most turbidites exhibit either Tade or Tbde patterns. Bouma (1962) division Tc is absent aside from rare occurrences of complete and nearly-complete turbidites.

III-K: Cores U1438E-50R to -47R; 1312.0-1283.0 mbsf

Subunit III-K contains a relatively high percentage of tuff/lapillistone. A relatively structureless 11-m thick tuff bed (Figure 11a) occurs at the top of the subunit. The relative content of primary volcanic material (ash) builds up section before dropping from 100% to 0% at the contact with subunit III-J. Between volcanic deposits are fine-grained turbidites and medium-grained turbidites with partial to nearly complete Bouma sequences (Figure 11b). Turbidites are affected by soft sediment deformation at the bottom of the subunit coherent at the top where thicknesses exceed 30 cm. Facies Classes B (sandstone), C, D (siltstone), and E (mudstone) (Table 1) occur in nearly equal proportions.

III-J: Cores U1438E-48R to -37R; 1283.0 - 1202.71 mbsf

Subunit III-J is primarily thin sandy turbidites, with minor isolated basin floor hemipelagic mudstones, debrites, and primary volcanic deposits. Core U1438E-42R is a primary tuff and lapillistone thicker than 2.6 m exhibiting faint lamination (Figure 12a). Turbidites are either fine-grained or are incomplete medium-grained Bouma (1962) sequences (Figure 12b). Turbidite thicknesses increase up section from ~20 cm to >50 cm. In addition, the primary Facies Class is E, corresponding to the abundance of mudstone (Table 1), although B, C, and D are introduced near the top of the subunit.

III-I: Cores U1438E-38R to -21R; 1202.71-1034.5 mbsf

Subunit III-I is a primarily debrite-rich subunit with intermixed fine-, medium-, and coarse-grained turbidites. Two clusters of debrites are separated by a 25 m interval of ~50-cm-thick Tabce turbidites. Both debrite clusters build up to about 85% debrite core percentage before abruptly dropping to 0%. The abrupt top of the second cluster is the boundary with overlying Subunit III-H. Within the debrite clusters are periodic 2 to 5-m thick fine- and medium-grained turbidite intervals (Figure 13a) overlain by debrite intervals (Figure 13b). Facies Classes A and B are dominant, meaning the dominant lithologies are conglomerate, sandstone, and siltstone (Table 1). Depositional unit thicknesses average greater than 30 cm, however contacts were often not recovered.

III-H: Cores U1438E-21R to -16R; 1034.5-983.5 mbsf

Subunit III-H is dominated by fine- to medium-grained turbidites (Figure 14). As an exception, Core U1438E-19R contains isolated thin debrites, a single primary lapillistone bed, and a single coarse-grained turbidite among the dominant thin fine-grained turbidites. Siltstone is the subunit's dominant lithology, meaning Facies Class D1.1 and D2.4 are dominant. Facies Classes A and B exist only within the most complete turbidites. The primary average turbidite thickness is >50 cm however two 2-3m packages of ~10 cm turbidites are present.

III-G: Cores U1438E-16R to D-66R; 983.5-831.2 mbsf

Subunit III-G contains a relatively high percentage of debrites. Debrites build up to a proportion of about 50% in Core U1438D-72R before gradually decreasing to 0%, marking the boundary with the overlying Subunit III-F. A highly faulted zone (Figure 15a) marks the transition from Hole E to Hole D where depositional units cannot be confidently interpreted.

Below the faulted zone gravel-sized clast content is very high and Facies Classes A and B dominate. Similar to Subunit III-I, the bottom of Subunit III-G contains alternating turbidite (Facies Classes C, D, and E; Figure 15b) and debrite (Figure 15c) intervals, with coarsening-upward trends. Debrites are consistently thicker than 1 m.

III-F: Cores U1438D-66R to -64R; 831.2-809.0 mbsf

Subunit III-F is the thinnest subunit in Unit III and is composed entirely of turbidites. The primary lithologies are sandstone and siltstone, which are organized in very thin nearly-complete medium-grained turbidites (Figure 16). No mudstone and minor gravel are present. One tuff bed occurs near the bottom of the subunit within a series of drilling-brecciated turbidites. Thin (<10 cm) turbidites of Facies Class D2.5 are interrupted by short intervals of turbidites thicker than 30 cm (Facies Class B1.1).

III-E: Cores U1438D-63R to -57R; 809.0-743.2 mbsf

Subunit III-E has a relatively high proportion of debrites (Figure 17a) that alternate with fine- and medium-grained turbidite intervals. Most medium-grained turbidites contain the Ta Bouma Division but those that do not are grouped together in relatively thin intervals with depositional unit thicknesses less than 30 cm (Figure 17b). Debrites and Ta-containing turbidites are greater than 1m thick. Intervals of thin fine- and medium-grained turbidites are common at the bottom of the subunit but are thicker and less common near the top. Facies Classes A, B, and D are present, meaning all lithologies are present except mudstone.

III-D: Cores U1438D-57R to -49R; 743.2-665.16 mbsf

Subunit III-D is fine- and medium-grained turbidite-dominated and is the most silt-rich section in Unit III. Fine-grained turbidites overprinted by bioturbation are accompanied by

isolated medium-grained turbidites (Figure 18a). Near the top of the subunit coarse-grained turbidites are introduced (Figure 18b) and transition into the overlying debrite-rich Subunit III-C. Depositional unit thickness ranges from 10 cm for the fine-grained turbidites to 75 cm for the medium- and coarse-grained turbidites at the top. Facies Class D2.5 (disturbed sequences of sand to silt turbidites) is prominent and B1.1 and B2.1, accompany the medium- and coarse-grained turbidites.

III-C: Cores U1438D-49R to -40R; 665.16-583.11 mbsf

Subunit III-C contains two intervals with a high debrite concentration within medium-grained turbidites. Most depositional unit contacts are not recovered, owing to drilling disturbance, but where recovered, depositional units are less than 1-m thick. A 16-m thick debris-flow deposit makes up the bottom of the subunit (Figure 19a) and is the start of the first buildup of debrites that continues into the overlying 30 m of section. Turbidites are sand-to-silt Tbcde varieties (Figure 19b) with zones of soft sediment deformation-disturbed fine-grained turbidites. Mudstone is present between the debrite intervals. Debrite-rich zones contain Facies Classes A and B while intervening turbidites are Facies Class D2.4 and D2.5.

III-B: Cores U1438D-40R to -36R; 583.11-541.0 mbsf

Subunit III-B is made up entirely of fine- to medium-grained turbidites. Turbidites are generally thin (<30 cm) (Figure 20a), and the thickest turbidite is 0.75 meters (Figure 20b). The entire subunit is fairly uniform in character. Exceptions are one tuff bed, one mudstone bed, and a few Ta turbidites at the bottom of the subunit. There is an upsection transition from mudstone-rich (Facies Class E), the highest mudstone content of Unit III, to siltstone-rich (Facies Class D).

III-A: Cores U1438D-36R to -12R; 541.0-309.55 mbsf

Subunit III-A contains a very high proportion of debrites (Figure 21a) with few interbedded turbidites. Debris-flow proportion builds from 0% in Core U1438D-37R to 100% in Core U1438D-31R, and remains high to the top of the subunit (Unit III-II boundary). Cores U1438D-25R and U1438D-16R contain relatively thin-bedded (10-50 cm) fine- and medium-grained siltstone-rich turbidite intervals (Figure 21b) that exhibit abrupt contacts with the surrounding debrite intervals. Debrites range from 1m thick to greater than 20 m thick (in Cores U1438D-22R to -24R) but thickness determinations are different because approximately 20 percent of depositional contacts were not recovered. The primary lithologies are conglomerate and coarse sandstone (Facies Class A).

Stratigraphic Subunit Designations for Unit II

The Unit III-II boundary was placed at 309.55 mbsf, within Core U1438D-12R by shipboard scientists. It is marked by an abrupt shift from the largely gravel-rich Unit III to the sandstone-to-mudstone turbidite- and hemipelagic mud-rich Unit II (Figure 22). The exact boundary was not recovered but was placed at the top of the youngest gravel-rich interval in a drilling-brecciated zone.

Unit II subunits are divided based on lithologic changes and degree of drilling disturbance of variably lithified subunits. This unit is primarily mud and mudstone, with a varying sandstone content that corresponds to the ratio of medium-grained turbidites to fine-grained turbidites. Drilling disturbance and hemipelagic mud proportions increase up section. Unit II is divided into three subunits, labelled “II-C”, “II-B”, and “II-A”, from oldest to youngest (Figure 9 and Table 3):

II-C: Cores U1438D-12R to B-29X; 309.55-237.9 mbsf

Subunit II-C immediately overlies the Unit III-II boundary and is composed of mud-rich turbidites. Individual bed contacts are indistinguishable due to soft sediment deformation (Figure 23) and drilling-related disturbance but turbidite divisions are discernable. The entire subunit is made up of fine-grained turbidites (Figure 23) with scattered sandy medium-grained turbidites. Sandy beds in II-C are the thickest of all Unit II. Facies Classes E1.1 and D1.1 dominate with lesser Facies Class B2.1 (sandy beds).

II-B: Cores U1438B-29X to -25X; 237.9-199.1 mbsf

Subunit II-B is too disturbed by drilling and bioturbation (Figure 24) to confidently apply any classification scheme to depositional units. Unconsolidated ash and lapilli beds are present in the upper two cores of the subunit (U1438B-25X and -24X). Sandstone is rare – yielding to an increased proportion of bioturbated mudstone (Facies Class E1.1) and siltstone (Facies Class D1.1).

II-A: Cores U1438D-25X to -18X; 199.1-160.25 mbsf

Subunit II-A makes up the top portion of Unit II and transitions into the hemipelagic mud of Unit I. The bottom twelve meters consists of sand-rich turbidites (Facies Class B1.1 & 2.1) (Figure 25a) and a relatively high volcanic ash content. Drilling brecciation means fine-grained depositional units cannot be confidently interpreted. Sand content decreases up section. The top 17.5 meters consists of unlithified hemipelagic mud (E1.1) with altered ash and no visible structures other than burrows (Figure 25b).

Unit II-I Boundary

The Unit II-I boundary is a shift from sandstone-to-mudstone turbidites with hemipelagic mud in Unit II to massive and uninterrupted hemipelagic mud in Unit I. This occurs at 160.25 mbsf, within Core U1438B-18H.

Subunit Sediment Accumulation Rates

The sediment accumulation rate varies throughout the subunits of Unit III and Unit II. Rates were calculated using subunit thicknesses and by correlating depths with ages on the time-depth plot created by shipboard scientists using biostratigraphic and paleomagnetic datums (Arculus et al., 2015a, 2015b; Figure 26). At the bottom of Unit III, sediment accumulation rates are fairly consistent, ranging from 29.4 m/my (Subunit III-K) to 49.8 m/my (Subunit III-L). The first occurrence of debrites (Subunit III-I) corresponds to the most rapid depositional rate (480.6 m/my). Rates then gradually decrease to 46.8 m/my (Subunit III-B) before the final occurrence of debrites just before the Unit III-II boundary (144.7 m/my in Subunit III-A). The average sediment accumulation rate for Unit III is 113.2 m/my: 180.1 m/my for the debrite-rich subunits, and 71.4 m/my for the debrite-poor subunits (Table 3).

Unit II sediment accumulation rates decrease from 47.8 m/my (Subunit II-C) to 9.7 m/my (Subunit II-A) in only 7 million years. This is nearly as low as the average of overlying Unit I (7.1 m/my), which contains no sediment gravity flows.

Unit III Lobe Systems

Further interpretive organization of the stratigraphic section was made in Unit III. Twelve lobe systems were identified, based on lobe and channel facies criteria introduced by Mutti and Normark (1987; Figure 7). The base of each lobe system was defined as an interval of mud-rich

lobe fringe or distal lobe facies. Distal facies are generally overlain by intermediate to proximal lobe facies defined by increasing proportion of interbedded debrites. Channel facies are debrite-dominated and contain a fining-upward top. The 12 lobes are described below, from oldest to youngest, then discussed in a later section.

Lobe System 1 (Figure 27) spans from Subunit III-L to III-I and is 184 m thick. Subunit III-L is distinguished by its very thin fine-, medium-, and coarse-grained turbidites (lobe fringe) and muddy beds. The turbidites are classified as lobe fringe deposits and the muddy deposits as hemipelagites. Tuff bed proportion increases through Subunit K starting in Core U1438E-50R (~1310 mbsf), where tuff is 17 percent of the core, and dissipates above Core U1438E-47R (~1285 mbsf), where ash is 100 percent of the core. These tuff beds are separated by disturbed fine- and medium -grained turbidites, thicker than those in Subunit III-L. Throughout the system depositional unit thicknesses and grain sizes gradually increase and a coarsening-upward succession emerges. By the top of Subunit III-J, facies transition to proximal lobe deposits.

Lobe System 2 (Figure 28) begins within Subunit III-I and is only 15.5 meters thick, making it the second-thinnest lobe of Unit III. The sequence begins in Core U1438E-36R (~1180 mbsf) with intermediate lobe deposits capping the coarse transitional facies that top Lobe System 1. A transition from fine-grained turbidites to coarse-grained turbidites to debrites spans the top half of Core U1438E-36R and the bottom half of Core U1438E-35R (~1175 mbsf) before a sharp drop in grain size occurs at the top of the lobe.

Lobe System 3 (Figure 28) immediately overlies Lobe System 2 and is thicker than the average for Unit III. Lobe 3 spans 76 m from Core U1438E-35R to -27R (~1090 mbsf). There is a 7-m lobe buildup from distal lobe facies to transitional facies extending through the top ~60 m

of the system where channel facies occur. Within the transitional facies, two intervals of proximal lobe facies occur.

Lobe System 4 (Figure 28) spans 57 m from Core U1438E-27R to the top of Subunit III-I in Core U1438E-20R (~1025 mbsf). The sequence transitions into intermediate and proximal lobe deposits. Distal to channel facies transition until Core U1438E-22R (~1045 mbsf), above which channel deposits dominate.

Lobe System 5 (Figure 29) begins at the base of fine-grained turbidite-rich Subunit III-H, which is made up completely of lobe fringe facies. The top of the subunit, Core U1438E-16R (~985 mbsf), contains intermediate lobe facies that grade upward into proximal, transitional, then finally channel facies in Core U1438E-12R (~950 mbsf). The top of Core U1438E-12R, however, contains proximal lobe facies that coarsen upward into channel deposits. This occurs again in Core U1438E-9R (~920 mbsf), grading from proximal to transitional facies as the 124-m thick lobe system terminates.

Lobe System 6 (Figure 29) is the thinnest of all identified systems deposited at Site U1438 being 13.4-m thick. Between Cores U1438E-8R (~910 mbsf) and U1438E-7R (~900 mbsf) facies transition from distal lobe to channel. It is roughly defined using grain size within a highly-disturbed zone at the Hole E/Hole D overlap (between Core U1438D-72R (~890 mbsf) and Core U1438E-7R (~900 mbsf)).

Lobe System 7 (Figure 29) begins in a highly disturbed zone from the top of Core U1438D-72R to the top of Core U1438D-70R (~870 mbsf), at the bottom of drilled Hole D. The disturbed sediment appears to be fine-grained so it is assumed to be the distal facies of a lobe system and separate from the coarse material of Lobe System 6 directly below. Overlying the

disturbed sediment are proximal lobe and channel-lobe transition facies that fine upward unto the overlying Lobe System 8. Shipboard scientists (Arculus et al., 2015c) interpreted the disrupted zone as a product of normal faulting, so there may be missing section in this interval.

Lobe System 8 (Figure 29) is of similar thickness to Lobe System 7 (33.8 m). A thick sequence of very thinly-bedded turbidites makes up the majority of the system. An increasing content of interbedded coarse-grained intervals constitute a coarsening-upward transition of lobe facies. The thin-bedded intervals continue into channel-lobe transitional facies at the top of the sequence and then fine upward into the overlying Lobe System 9.

Lobe System 9 (Figure 30) spans from Subunit III-F to III-E (86 m). Subunit III-F contains proximal to intermediate lobe deposits where alternating medium- to coarse-grained turbidites and fine-grained turbidites form thin packages. Periodic thick (0.5 to 1 m) coarse turbidites are intermediate lobe facies. The overlying Subunit III-E consists of channel-lobe transition facies. Above the Subunit III-E-F boundary, facies transition upward to intermediate lobe facies, for a short interval, then coarsen-upward to channel facies. Following a thin channel-facies interval intermediate facies return before another facies sequence that terminates with channel-lobe transitional facies deposition.

Lobe System 10 (Figure 30) spans from Subunit III-D to III-C (106 m). Subunit III-D is made up of distal lobe fringe facies that transition to intermediate lobe facies at the top. The bottom of Subunit III-C continues the thick facies transition started in III-D. In cores U1438D-46R (~640 mbsf), -47R (~650 mbsf) and -48R (~660 mbsf) thick channel-facies debrites mark the top of the lobe system.

Lobe System 11 (Figure 30) is the second lobe that occurs within Subunit III-C and is much thinner (39 m versus 106 m). Above the thick debrites of Lobe System 10, distal, intermediate, and proximal lobe facies mark the base of Lobe System 11. In Core U1438D-44R (~620 mbsf) debrites mark the introduction of channel facies that terminate in core U1438D-42R (~600 mbsf). A short fining-upward sequence leads into Subunit III-B.

Lobe System 12 (Figure 31), the thickest (288 m) and most complex system deposited at Site U1438, comprises Subunits III-A and III-B. The base (Subunit III-B) contains intermediate to distal lobe facies with alternating medium-grained turbidites and disturbed fine-grained turbidites with few coarse turbidites and tuff beds. These pass upwards into intermediate lobe facies then to proximal lobe facies (core U1438D-34R (~520 mbsf)), then channel facies beginning at Core U1438D-33R. The top of Core U1438D-33R (~510 mbsf) and the bottom of Core U1438D-32R (~505 mbsf) contain thin and fine turbidites that lack Ta divisions, a characteristic of intermediate lobe facies. The top of Core U1438D-32R contains proximal lobe facies that grade up into channel facies by Core U1438D-31R (~495 mbsf). A thin interval of distal lobe facies (core U1438D-25R (~435 mbsf)) is abruptly overlain in core U1438D-24R (~425 mbsf) by thick debrites. Four meters of section were unrecovered between core U1438D-25R and -24R so the nature of the exact facies transition is unknown. Channelized debrites continue until core U1438D-16R (~350 mbsf), which contains thin turbidite and debrite interbeds. Core U1438D-16R displays a short transitional interval with channel facies debrites, overlain by an interval of thick debrites without turbidites. Given the massive debrites above and below the distal love facies, the sediment package was treated as one lobe system.

Discussion

General Downhole Trends

In general, the downhole patterns of grain sizes, facies and depositional unit types displayed in Figure 9 are similar. The calculated core-by-core distribution of grain size proportions is consistent with the general pattern of shipboard measurements of average grain sizes (Figure 3a), but provides more detail regarding the proportions of lithologies at any given core interval. The Pickering and Hiscott (1986) Facies Classes are, in turn, also roughly affiliated with certain grain sizes but with some exceptions outlined below (Figure 9). Typically, Facies Class E is associated with mudstone, however, inconsistencies between the shipboard lithologic descriptions and observations made from core images means that Facies Classes D and E are not directly correlative with siltstone and mudstone. Below 1200 mbsf, Facies Class C is prominent. Facies Class C is defined as couplets of sandstone and mudstone (Table 1), which in some cases are classified as alternating Facies Class B (sandstone) with Facies Class E (mudstone) or D (siltstone). Generally, turbidites correlate with mudstone (Facies Class E), siltstone (Facies Class D), and sandstone (Facies Classes B and C) and debrites correlate with gravelly sandstone (Facies Class A1.4) and conglomerate (Facies Class A1.1). Debrites may also contain Facies Class B sandstone in fine-grained intervals so grain sizes, Facies Classes, and depositional units (Figure 9) are not directly comparable in all cases.

Modern Analogues and Depositional Model

Modern analogues for the paleo-IBM Arc edifice are found along the present-day arc front. Anatahan Island, part of the Mariana Volcanic Arc (bottom-right of Figure 1), is an example (Chadwick et al., 2005). Anatahan Island is an arc volcano, which sheds volcaniclastic

material onto its own volcaniclastic apron as well as into a channel system that transports sediment into the backarc basin (Figure 32). This island and the associated sediment input is akin to the volcanoes of the paleo-IBM arc edifice.

Furthermore, the West Mariana Ridge is a younger analogue for the remnant Kyushu Palau Ridge. The West Mariana Ridge is a remnant arc formed by backarc spreading associated with rifting of the Mariana Arc to the southeast of the upper Kyushu Palau Ridge (Figure 1). The backarc basin appears to have been fed sediment by channel systems from multiple sources, some more distal than others (Figure 33). Due to rapid growth, interlayered weak rocks, and destabilizing volcanic activity, island arc volcanoes frequently experience catastrophic edifice slope-apron collapses and volcano sector collapse. Triggers may be magmatic (eruption-triggered) or nonmagmatic (seismic or gravitational). Slope failures generally produce debris flows and debris avalanches and may begin subaerially (Coombs et al., 2007). No distinct lobe morphology can be seen using the Google Earth images in Figure 33 but subtle lobe features may be masked by later hemipelagic sedimentation. Headless channels extending out into the backarc basin from the top of the ridge are evidence for dissection of the arc by rift-related normal faults from the active arc to the east (Figure 33). The circled area of Figure 33 denotes where Site U1438 might be situated given the approximate proximity of Site U1438 to the KPR. Present day depths of the three primary channels in the circled area are 60 m, as measured using Google Earth Pro. Bathymetric definition of similar channel (and lobe?) features in the ASB has been masked by subsequent hemipelagic sedimentation (Figure 1, inset), but may be defined in the subsurface using limited seismic data across the region (M. Gurnis, personal communication).

A depositional model for Site U1438 is shown in Figure 34 in three-dimensional perspective and in Figure 35 in plan view. It is based on the modern analogues (Figures 32 and 33) discussed above and submarine fan models like that pictured in Figure 8.

The Sedimentary Record of Arc Development at Site U1438

During the time frame of Unit IV deposition (~42 to ~55 Ma), the arc was young and a large volcanic edifice may not have yet formed (Waldman, 2015). The increase in coarse-grained material input and the increase in sediment accumulation rates immediately following the Unit IV-III boundary suggests that it was the commencement of arc edifice building (Figure 36). The shipboard-defined Unit IV-III boundary, which was defined using only grain size trends and mudstone radiolarian content, is further supported by this study. The Unit IV-III Boundary corresponds with depositional unit, facies, and lithologic changes. All turbidites are fine-grained within Unit IV, however, turbidites become more sand-rich, thicker, and exhibit more complete Bouma (1962) sequences above the boundary. Radiolarian content diminishes up-core in subunit III-L. A sharp decrease in apparent bed thicknesses also occurs upsection from Unit IV to Unit III. Rather than an abrupt Unit boundary, a relatively major facies change at about 1200 mbsf tops a thick interval that shows a gradational change from muddy Unit IV to a series of gravel-rich intervals likely associated with progradation of lobe-channel facies to the site.

Once the arc edifice building commenced, volcaniclastic material was shed from the paleo-IBM Arc (Kyushu-Palau Ridge) in submarine sediment gravity flows triggered by high-volume volcanic eruptions, tectonic/seismic activity, or dome or sector collapses (Brandl et al., in review), and transported via channels to form submarine lobes. Applying the facies criteria of Mutti and Normark (1987) shown in Figure 7, multiple lobe systems are apparent within Unit III. Detailed analyses of facies, deposit types, and grain sizes reveal at least 12 lobe systems between

the start of volcanic edifice building (Unit IV-III Boundary) and rifting of the paleo-IBM Arc (Unit III-II Boundary). The 12 lobe systems are interpreted as prograding lobe systems that migrated and overlapped each other to build a thick fan succession that makes up Unit III, similar to what is depicted in the column in Figure 8 from Covault (2011) after Mutti and Ricci Lucchi (1972).

Four groups (episodes) of stacked lobe systems and coarse sediment accumulation can be identified; these are separated by thick intervals of thin and fine-grained turbidites (Figure 36). Episode 1, which contains the top of Lobe System 1 as well as Lobe Systems 2, 3, and 4 (Figure 36), represents the first, and largest, period of edifice slope degradation/collapse within Unit III. Distal lobe fringe deposits (Lobe System 1), starting at the Unit IV-III Boundary, represent the initiation of IBM Arc edifice building and began a gradual lobe-facies progradation that deposited a large number of debris flows and began a sequence of tightly-packed prograding lobes. Episode 1 experienced an abnormally high sediment accumulation rate as a result of rapid sediment shedding from the arc.

The second episode of edifice slope degradation/collapse (Subunits III-G to III-E) contains the lowest debrite content of the episodes. No cores in this interval contain a debrite proportion greater than 50 percent and most lobes terminate during a channel-lobe transitional period and do not reach a channel-facies phase. This could mean that 1) the system stopped receiving coarse-grained material before the channel prograded to the site (meaning the slope degradation events or sector collapses are smaller or are at a greater distance), or 2) a different source began supplying sediment to the site on top of an already-prograding system.

The first, second, and fourth collapse episodes exhibit lobe systems that contain overlapping sequences of prograding lobe facies that do not contain distal lobe facies used to

define the base of a lobe system and differentiate it from others. The overlapping of lobes may be a result of distributary channel switching within the lobe system that results in finer and less mature lobe facies being deposited for short periods of time. Multiple tributary channel sources may have fed the system, similar to the coalescing tributary channel systems seen extending from the Mariana Ridge in Figure 33; these may have been the cause of the overlapping character of Lobe Systems 3, 5, 9, and 12.

All the sediment may have been sourced from the nearby KPR, or from a number of alternative sources, such as more distal portions of the KPR or from seamounts located west of Site U1438 (Figure 37). The more distal potential sources likely only provided fine-grained primary volcanic or mud gravity flows. Coarse debrite content likely correlated with volcano maturity (size) and/or proximity of the source arc edifice (Mutti and Normark, 1987), where larger volcanic edifices shed coarser material further into the basin. Sediment accumulation rate would therefore have been related to productivity of the arc volcanoes. High sediment accumulation rates correspond to more rapid shedding of material from arc volcanoes and, therefore, a closer spacing of events that triggered edifice slope failures.

The contact of Unit III (within core U1438D-12R) with Unit II (Figure 22) was not recovered, however it was interpreted as an abrupt change by shipboard scientists. This abrupt cessation of channel debrite deposits represents the shutoff of material feeding the system. This interpretation is supported by a decrease in sediment accumulation rate from 144.7 m/my in III-A to 47.8 m/my in II-C. This unit boundary likely represents the initiation of rifting of the paleo-IBM arc axis, leading to the creation of the Kyushu Palau Ridge remnant arc and the ultimate cessation of volcaniclastic gravity flow input to the Amami Sankaku Basin.

Following the initiation of rifting, debrites and coarse-grained facies were no longer deposited at Site U1438. Instead there is an abundance of fine-grained turbidites. The nature of the fine-grained turbidites in Unit II are masked by drilling disturbance, but a few interbedded medium-grained turbidites are distinguishable; within Subunit II-C nearly all medium-grained turbidites are Tbcde turbidites.

The proportions of hemipelagic mud and fine-grained turbidity current deposits increases up section throughout Unit II, until the Unit II-Unit I boundary where turbidity current input stopped. The gradually decreasing turbidity-current input throughout Unit II represents the eastward displacement of the paleo-IBM Arc. Additionally, the sediment accumulation rate gradually decreased from 47.8 m/my (Subunit II-C average, Table 3) to 9.7 m/my (Subunit II-A average, Table 3) in the 7 million-year Unit II rifting sequence. Because sediment gravity flows originated from the active arc front, sediment input decreased as the distance progressively increased as a result of the rifting and dissection of the arc edifice similar to that pictured in Figure 33.

Application of Facies and Depositional Models to Magmatic Studies

Brandl et al. (in review) correlated melt inclusion composition to volcanic output and arc evolution at Site U1438. Three-hundred-nineteen glass inclusions in pyroxene and plagioclase were chemically analyzed to uncover the progressive transition of melt compositions within the Site U1438 section. They discovered that melt compositions transitioned from boninites (infant arc), then to high-Mg andesites (juvenile arc), then finally to island arc tholeiites (mature arc) within Units IV and III. Boninite composition related to an infantile arc stage were discovered within forearc glass of an age similar to Unit IV, high-mg andesite compositions related to juvenile arcs were discovered within the primary arc edifice buildup, and island arc tholeiite

compositions related to mature arcs were discovered in glass inclusions of the remainder of Unit III (Brandl et al., in review; Figure 26). Consequently, this progression suggests a gradual increase in volcanic productivity – which is supported by the depositional history and facies data uncovered in this study, as well as in the pattern of sediment accumulation at the site (Table 3). The highest sediment accumulation rates at ~1000-1200 mbsf (Table 3) correspond to the change from high-Mg andesites to arc tholeiites (Figure 26), suggesting some potential correspondence between arc volcanism (pyroclastic production rate) and arc geochemical evolution (Brandl et al., in review).

Future Work

Potential future study of Site U1438 facies and depositional units would include a detailed analysis of bed thicknesses in intervals where they are intact and undisturbed. One might see trends in thickness that correlate with the depositional lobe division interpretations. Future work may introduce additional petrologic data that could be compared to trends described above. Constraining the source(s) of sediment would require future seismic work, to show geometry and paths of channels that once led to Site U1438. Petrographic work might provide insight into origin and depositional mechanisms of individual depositional units.

Conclusions

The series of sediment gravity flows deposited at Site U1438 contain evidence of arc edifice building and periodic slope-apron collapses. The shipboard hypothesis that Unit III and II represent sedimentation during building and rifting of the active paleo-IBM arc is supported by the detailed volcaniclastic sediment analysis of this study, along with the placement of the major Unit IV/III boundary.

The grain size, facies classes and depositional unit schemes developed for this study were effective for discerning downhole patterns in sedimentation. The subunit designations and patterns in gravity-flow deposit types aided in the detailed analysis and construction of the depositional model as a series of stacked lobe systems that collectively accumulated in the backarc basin, potentially with a fan geometry. The lobe subdivisions, in many cases, were a combination of a turbidite-dominated subunit and an overlying debris-flow subunit, with a transition of lobe facies between them.

The bottom of Unit III contains a thick (260m) coarsening-upward sequence that begins at the Unit IV-Unit III boundary. Distal lobe and lobe fringe facies were deposited, followed by thick volcanic ash deposition and then prograding submarine lobe facies. This period was the initial building of the arc edifice (Lobe System 1) and was followed by the first major coarse material accumulation.

Prograding debris flow-rich lobe-channel sequences can be grouped together into four episodes, each interpreted as edifice slope collapse deposits. Three of the episodes contain overlapping lobe facies that may have resulted from channel switching or input from a different

source. The progressive upsection coarsening of episodes and the increasing channel-facies thicknesses within each suggests progressively-prograding facies from a maturing arc.

The abrupt change from very thick and massive debris flows to fine-grained turbidites at the Unit III-Unit II boundary reflects arc rifting; turbidity current input progressively diminished in favor of hemipelagic mud settling, until turbidity currents waned marking the contact of Unit II with Unit I.

References

Allen, S. R., Hayward, B. W., and Matthews, E., 2007, A facies model for a submarine volcaniclastic apron: The Miocene Manukau Subgroup, New Zealand: GSA Bulletin, v. 119, p. 725-742.

Arculus, R.J., Ishizuka, O., Bogus, K., Aljahdali, M.H., Bandini-Maeder, A.N., Barth, A.P., Brandl, P.A., do Monte Guerra, R., Drab, L., Gurnis, M.C., Hamada, M., Hickey-Vargas, R.L., Jiang, F., Kanayama, K., Kender, S., Kusano, Y., Li, H., Loudin, L.C., Maffione, M., Marsaglia, K.M., McCarthy, A., Meffre, S., Morris, A., Neuhaus, M., Savov, I.P., Sena Da Silva, C.A., Tepley, F.J., III, van der Land, C., Yogodzinski, G.M., and Zhang, Z., 2015a, Expedition 351 summary. *In* Arculus, R.J., Ishizuka, O., Bogus, K., and the Expedition 351 Scientists, *Proceedings of the International Ocean Discovery Program, Expedition 351: Izu-Bonin-Mariana Arc Origins:* College Station, TX (International Ocean Discovery Program). Accessed 1 Feb 2014. **http://dx.doi.org/10.14379/iodp.proc.351.101.2015**

Arculus, R.J., Ishizuka, O., Bogus, K., Aljahdali, M.H., Bandini-Maeder, A.N., Barth, A.P., Brandl, P.A., do Monte Guerra, R., Drab, L., Gurnis, M.C., Hamada, M., Hickey-Vargas, R.L., Jiang, F., Kanayama, K., Kender, S., Kusano, Y., Li, H., Loudin, L.C., Maffione, M., Marsaglia, K.M., McCarthy, A., Meffre, S., Morris, A., Neuhaus, M., Savov, I.P., Sena Da Silva, C.A., Tepley, F.J., III, van der Land, C., Yogodzinski, G.M., and Zhang, Z., 2015b, Expedition 351 methods. *In* Arculus, R.J., Ishizuka, O., Bogus, K., and the Expedition 351 Scientists, *Proceedings of the International Ocean Discovery Program, Expedition 351: Izu-Bonin-Mariana Arc Origins:* College Station, TX (International Ocean Discovery Program). Accessed 1 Feb 2014. **http://dx.doi.org/10.14379/iodp.proc.351.102.2015**

Arculus, R.J., Ishizuka, O., Bogus, K., Aljahdali, M.H., Bandini-Maeder, A.N., Barth, A.P., Brandl, P.A., do Monte Guerra, R., Drab, L., Gurnis, M.C., Hamada, M., Hickey-Vargas, R.L., Jiang, F., Kanayama, K., Kender, S., Kusano, Y., Li, H., Loudin, L.C., Maffione, M., Marsaglia, K.M., McCarthy, A., Meffre, S., Morris, A., Neuhaus, M., Savov, I.P., Sena Da Silva, C.A., Tepley, F.J., III, van der Land, C., Yogodzinski, G.M., and Zhang, Z., 2015c, Site U1438. *In* Arculus, R.J., Ishizuka, O., Bogus, K., and the Expedition 351 Scientists, *Proceedings of the International Ocean Discovery Program, Expedition 351: Izu-Bonin-Mariana Arc Origins:* College Station, TX (International Ocean Discovery Program). Accessed 1 Feb 2014. **http://dx.doi.org/10.14379/iodp.proc.351.103.2015**

Arculus, R., Ishizuka, O., Bogus, K., Gurnis, M., Hickey-Vargas, R., Aljahdali, M., Bandini-Maeder, A., Barth, A., Brandl, P., Drab, L., do Monte Guerra, R., Hamada, M., Jiang, F., Kanayama, K., Kender, S., Kusano, Y., Li, H., Loudin, L., Maffione, Marsaglia, K., McCarthy, A., Meffre, S., Morris, A., Neuhaus, M., Savov, I., Sena, C., Tepley, F., van der Land, C., Yogodzinski, G., Zhang, Z., 2015d, A record of spontaneous subduction initiation in the Izu-Bonin-Mariana arc: Nature Geoscience, doi:10.1038/ngeo2515.

Boggs, S., 2012, Principles of Sedimentology and Stratigraphy, Fifth Edition: Upper Saddle River, New Jersey, Pearson Education, Inc., 585 p.

Bouma, A.H., 1962, Sedimentology of some Flysch deposits: A graphic approach to facies interpretation: Elsevier Publishing Company, 168 p.

Brandl, P.A., Hamada, M., Arculus, R.J., Johnson, K., Marsaglia, K.M., Ishizuka, O., and Savov, I., in review, The arc arises: The links between volcanic output, arc evolution, and melt composition: submitted to Earth and Planetary Science Letters.

Busby-Spera, C.J., 1987, Lithofacies of deep marine basalts emplaced on a Jurassic backarc apron, Baja California (Mexico): Journal of Geology, v. 95, p. 671–686.

Chadwick. W. W., Embley, R. W., Johnson, P. D., Merle, S. G., Ristau, S., and Bobbitt, A., 2005, The submarine flanks of the Anatahan Volcano, commonwealth of the Northern Mariana Islands: Journal of Volcanology, v. 146: p. 8-25.

Coombs, M. L., White, S. M., and Scholl, D. W., 2007, Massive edifice failure at Aleutian arc volcanoes: Earth and Planetary Science Letters, v. 256, p. 403-418.

Covault, J. A., 2011, Submarine Fans and Canyon-Channel Systems: A Review of Processes, Products, and Models: Nature Education Knowledge, v. 3(10).

Hiscott, R.N., Colella, A., Pezard, P., Lovell, M.A., and Malinverno, A., 1992, Sedimentology of deep-water volcaniclastics, Oligocene Izu-Bonin forearc basin, based on formation microscanner images: *In* Taylor, B., Fujioka, K., et al., Proceedings ODP, Scientific Results, 126: College Station, TX (Ocean Drilling Program), p. 75–96.

Ishizuka, O., Taylor, R.N., Yuasa, M., and Ohara, Y., 2011, Making and breaking an island arc: a new perspective from the Oligocene Kyushu-Palau arc, Philippine Sea: Geochemistry, Geophysics, Geosystems, v. 12(5): Q05005. Accessed 1 Mar 2016. **http://dx.doi.org/10.1029/2010GC003440**

Johnson, K., Waldman, R., and Marsaglia, K.M., in prep., Data Report: Sedimentary Columns with Facies and Bedding for Units II-IV at IODP Site U1438: will submit to Proceedings of the International Ocean Discovery Program, v. 351.

Klein, G. D., 1985, The control of depositional depth, tectonic uplift, and volcanism on sedimentation processes in the back-arc basins of the western Pacific Ocean: The Journal of Geology, v. 93, p. 1-25.

Lowe, D., 1982, Sediment gravity flows: II: Depositional models with special reference to the deposits of high-density turbidity currents: Journal of Sedimentary Petrology, v. 52, p. 279-297.

Marsaglia, K.M., 1995, Chapter 8, Interarc and backarc basins, in Busby, C. and Ingersoll R.V., eds., Tectonics of Sedimentary Basins, Blackwell, p. 299-329.

Marsaglia, K.M., and Devaney, K.A., 1995, Tectonic and magmatic controls on backarc basin sedimentation: The Mariana Region re-examined: In Taylor, B., ed., Backarc Basins: Tectonics and Magmatism, Plenum, New York, p.497-520.

Mutti, E. and Normark, W.R., 1987, Comparing examples of modern and ancient turbidite systems: problems and concepts: In: Leggett, J.K. and Zuffa, G.G., eds., Marine Clastic Sedimentology, London: Graham & Trotman, p. 1-38.

Mutti, E. and Ricci Lucchi, F., 1972, Le torbiditi dell'Appennino settentrionale; introduzione all' analisi di facies: Bollettino Societa Geologica Italiana, v. 11, p. 161-199.

Normark, W.R., 1978, Fan valleys, channels, and depositional lobes on modern submarine fans: characters for recognition of sandy turbidite environments: AAPG Bulletin, v. 62, p. 912-931.

Pickering, K.T., Hiscott, R.N. and Hein, F.J., 1989, Deep Marine Environments: Clastic Sedimentation and Tectonics: Unwin Hyman Ltd., 416 p.

Pickering, K.T., and Hiscott, R.N., 2016, Deep Marine Systems, Processes, Deposits, Environments, Tectonics and Sedimentation, John Wiley and Sons, 672p.

Pickering, K., Stow, D., Watson, M., and Hiscott, R., 1986, Deep-water facies, processes and models: A review and classification scheme for modern and ancient sediments: Earth Science Reviews, v. 23, p. 75-174.

Stow, D.A.V., and Shanmugam, G., 1980, Sequence of structures in fine-grained turbidites: comparison of recent deep-sea and ancient flysch sediments: Sedimentary Geology, v. 25, p. 23-42.

Tamaki, K. and Honza, E., 1991, Global tectonics and formation of marginal basins: role of the western Pacific: Episodes, v. 14, p. 224-230.

Tamura, Y., Busby, C., and Blum, P., 2013. Izu-Bonin-Mariana Rear Arc: the missing half of the subduction factory. International Ocean Discovery Program Scientific Prospectus, 350. Accessed 1 Sep 2014 **http://dx.doi.org/10.2204/iodp.sp.350.2013**

Taylor, B., Fujioka, K., et al., 1990. Proceedings of the Ocean Drilling Program, Initial Reports, Vol. 126: College Station, TX (Ocean Drilling Program).

Waldman, R., 2015, Early subduction and depositional history of the Izu-Bonin Mariana Arc back-arc system, western Pacific Ocean, Unpublished BS thesis, California State University Northridge.

Waldman, R., Marsaglia, K.M., and Johnson, K., in prep., Early depositional history of the Eocene Izu-Bonin Mariana Arc back-arc system, western Pacific Ocean: will be submitted to Geology.

APPENDIX A: FIGURE CAPTIONS

Figure 1. Bathymetric map of the Philippine Sea region. Location of Site U1438 within the Amami Sankaku Basin (ASB) is marked by a purple star. ODP Site 1201 is represented by the smaller purple star. Figure from Arculus et al. (2015a). Inset map of ASB is courtesy of Osamu Ishizuka with location of Site U1438 and ages of dredge samples as indicated: KPR = Kyushu Palau Ridge and AP = Amami Plateau.

Figure 2. Four-stage model of sedimentation patterns during magmatic arc rifting and backarc basin opening in the Mariana Arc region from Marsaglia and Devaney (1995). Numbered sediment packages refer to shifts and relative timing of volcaniclastic sedimentation during backarc spreading.

Figure 3. a) Preliminary schematic stratigraphic column of the cored interval at Site U1438 holes A, B, D, and E on Expedition 351 from Arculus et al. (2015a) with a plot of average grain size in 5-m bins (cl = clay; si = silt; ms-vcs = medium to very coarse sand; and gr = gravel), b) example of core-scale stratigraphic column produced in this study (see Supplemental Material file), with reference to location on full-scale column, and c) example of section-scale stratigraphic columns and their respective locations on the core-scale column. The latter will be published online as part of Johnson et al. (in prep.). See text and Figures 4 and 5 for explanation.

Figure 4. Key for symbols used to depict textures, sedimentary structures, and contacts on the core-scale stratigraphic columns in the Supplemental Material file and Figure 3.

Figure 5. Schemes used to classify bedding types within the core. Sources of three upper schemes are as indicated, the remainder were created for this study. See text for more discussion. Core images of examples of each are given in Figure 6.

Figure 6. Example core images of: a) nearly complete Stow and Shanmugam (1982) fine-grained turbidite sequence in Section U1438E-15R-1; b) complete Bouma (1962) medium-grained turbidite sequence in Section U1438E-34R-5; c) complete Lowe (1982) S coarse-grained turbidite sequence in Section U1438E-26R-4; d) M_1 hemipelagic mudstone in Section U1438E-52R-1; e) D_2 debrite in Section U1438D-12R-3; and f) V_1 primary tuff in Section U1438E-48R-1. Note scales in centimeters on left of each core image. Gravity-flow elements marked on images are defined in Figure 5.

Figure 7. Field characteristics of channel, channel-lobe transition, and proximal to distal lobe deposits from Mutti and Normarck (1987). 1a = erosional channel; 1b = depositional channel; 1c = zone of roughness; 1d = lobe relief; 2a = beds truncate against channel margin; 2b = beds converge toward channel edge; 2c = bedding irregularity resulting from scours and large-scale bedforms; 2d = parallel bedding planes; 3a = clast-supported lag conglomerate; 3b = mud-supported conglomerate (debrite); 3c = thin-bedded overbank deposits; 3d and 3e = coarse-grained, internally-stratified sandstones; 3f = complete and base-missing Bouma sequences; 4a = deep and relatively narrow scours associated with bedrock clasts; 4b = armored mud clasts; 4c = mud-draped scours; 4d = broad scours locally associated with mud clasts; 4e = tabular scours invariably associated with mud rip-up clasts from underlying deposits; 4f = ‘nests’ of mud clasts commonly showing inverse

grading and evidence of being plucked from the substrate; 5a = slump units; and 5b = scours and deformation produced by clast impacts.

Figure 8. Ancient submarine fan model of Mutti and Ricci Lucchi (1972); figure is from Covault (2011).

Figure 9. Downhole distributions of grain size, facies classes, and depositional units, on a core-by-core basis. Subunits of Unit III outlined in this study are defined to the right, along with shipboard-defined units and ages (Arculus et al., 2015a, 2015c). The key for facies classes refers to classes in Table 1: disorganized mud = E1, organized mud = E2, disorganized silt = D1, organized silt = D2, sand and mud couplets = C2, disorganized sand = B1, organized sand = B2, disorganized gravel = A1, and sandy gravel = A2. Bin size is one 9.5 m core interval (9.5m or less recovery).

Figure 10. Images of core examples from Subunit III-L: a) thin turbidites in Section U1438E-54R-2; and b) one of many unstructured hemipelagic mud beds examined in this study; this example present in Section U1438E-52R-1. Note scales in cm on left of core images.

Figure 11. Core image examples from Subunit III-K: a) part of the thick primary tuff bed in Section U1438E-47R-1; and b) medium-grained turbidite from Section U1438E-48R-4. Note scales in cm on left of core images. Gravity-flow elements marked on images are defined in Figure 5.

Figure 12. Core image examples from Subunit III-J: a) primary tuff bed from Section U1438E-42R-1; and b) Tbce turbidite in Section U1438E-40R-1. Note scales in cm on left of core images. Gravity-flow elements marked on images are defined in Figure 5.

Figure 13. Core image examples from Subunit III-I: a) an example turbidite interval that lies between thick debrite beds (out of image area). Sedimentary structures are likely overprinted and distorted by secondary alteration to zeolites. Core image from Section U1438E-24R-4; and b) the base of a thick debrite bed found in Section U1438E-25R-5. Note scales in cm on left of core images. Gravity-flow elements marked on image are defined in Figure 5.

Figure 14. Core image example from Subunit III-H: This is a typical Subunit III-H turbidite sequence, from Section U1438E-18R-3. Note scale in cm on left of core image. Gravity-flow elements marked on image are defined in Figure 5.

Figure 15. Core image examples from Subunit III-G: a) a portion of the highly disturbed and microfaulted zone at the base of Hole D, Section U1438D-71R-2; b) part of a turbidite interval situated between debrites, from Section U1438E-14R-4; and c) the typical appearance of debrites found in Subunit III-G, from Section U1438E-8R-1. Note scales in cm on left of core images. Gravity-flow elements marked on image are defined in Figure 5.

Figure 16. Core image example from Subunit III-F shows a typical turbidite from thin Subunit III-F, within Section U1438D-64R-1. Note scale in cm on left of core image. Gravity-flow elements marked on image are defined in Figure 5.

Figure 17. Core image examples from Subunit III-E: a) the typical appearance of Subunit III-E debrites, in Section U1438D-63R-1; and b) turbidites deposited within debrite intervals, in Section U1438D-60R-7. Note scales in cm on left of core images. Gravity-flow elements marked on images are defined in Figure 5.

Figure 18. Core image examples from Subunit III-D: a) fine- and medium- grained turbidites in Section U1438D-50R-5; and b) coarse-grained turbidites in Section U1438D-49R-6. Note scales in cm on left of core images. Gravity-flow elements marked on image are defined in Figure 5.

Figure 19. Core image examples from Subunit III-C: a) part of the 16-meter debrite bed that makes up the bottom of the subunit in Section U1438D-47R-2; and b) one of many Tbcde turbidites in Subunit III-C, in Section U1438D-43R-2. Note scales in cm on left of core images. Gravity-flow elements marked on image are defined in Figure 5.

Figure 20. Core image examples from Subunit III-B: a) thin medium-grained turbidites in Section U1438D-39R-3; and b) 0.75m-thick Tbcde turbidite in Section U1438D-39R-5. Top is not shown. Note scales in cm on left of core images. Gravity-flow elements marked on images are defined in Figure 5.

Figure 21. Core image examples from Subunit III-A: a) part of the debrite bed immediately below the Unit III-II boundary in Section U1438D-12R-3. b) A fine-grained turbidite in Section U1438D-25R-5 from the fine- and medium-grained turbidite interval that makes up Core U1438D-25R. Note scales in cm on left of core images. Gravity-flow element marked on image is defined in Figure 5.

Figure 22. The Unit III-Unit II boundary in Section U1438D-12R-3. Note the contact was not recovered but drawn in rubble zone where lithlogies change from mudstone to conglomerate. Note scale in cm on left of core image.

Figure 23. Core image example from II-C: This is an example of the prominent convoluted fine-grained turbidite in Section U1438D-9R-2. Note scale in cm on left of core image.

Figure 24. Core image from Subunit II-B: This is an example of drilling disturbance (brecciation) in fine-grained heavily bioturbated beds within this subunit from Section U1438B-28X-3. Note scale in cm on left of core image.

Figure 25. Core image examples from Subunit II-A: a) the final turbidites deposited at Site U1438. This turbidite is from Section U1438B-23X-2; and b) hemipelagic mud and dark, fining-upward primary ash in Section U1438B-18H-2. Note scales in cm on left of core images. Gravity-flow elements marked on image are defined in Figure 5.

Figure 26. The time-depth plot for Site U1438 was modified from Arculus et al. (2015d) to include interpretations of compositional data from Brandl et al. (in review). Ages were determined using micro-paleontological and paleomagnetic datums. High sediment accumulation rates occurred during the time of arc volcanism (Units II and III) and there is a significant decrease after arc rifting and KPR abandonment (Unit I). Colors distinguish paths of different sediment accumulation rates (slopes) at the bottom of Unit III, where datum points are sparse. Pairs of lines reflect

uncertainty in ages. Note that the recovery column is white where the section is not recovered

Figure 27. A detailed look at Lobe System 1, which is interpreted as the first buildup of the arc edifice following arc initiation. The darker colors correspond with intervals of coarser material, where debrites are black and fine-grained turbidites are the lightest gray. White intervals are tephra or hemipelagic mud. Width of lobe systems in this visualization corresponds to facies outlined in Figure 35 (distal lobe, intermediate lobe, proximal lobe, channel-lobe transition, and channel facies), where distal lobe facies are narrow intervals and the widest portions of the column are channel facies. See Supplemental Material for core summary column details.

Figure 28. A detailed look at Lobe Systems 2-4, which were deposited during the first edifice failure episode. The darker colors correspond with intervals of coarser material, where debrites are black and fine-grained turbidites are the lightest gray. White intervals are tephra or hemipelagic mud. Width of lobe systems in this visualization corresponds to facies outlined in Figure 35 (distal lobe, intermediate lobe, proximal lobe, channel-lobe transition, and channel facies), where distal lobe facies are narrow intervals and the widest portions of the column are channel facies. See Supplemental Material for core summary column details.

Figure 29. A detailed look at Lobe Systems 5-8, which define a second major edifice-failure episode. The darker colors correspond with intervals of coarser material, where debrites are black and fine-grained turbidites are the lightest gray. White intervals are tephra or hemipelagic mud. Width of lobe systems in this visualization corresponds to facies outlined in Figure 35 (distal lobe, intermediate lobe, proximal

lobe, channel-lobe transition, and channel facies), where distal lobe facies are narrow intervals and the widest portions of the column are channel facies. See Supplemental Material for core summary column details.

Figure 30. A detailed look at Lobe Systems 9-11, which define the second and third edifice failure episodes; these are separated by the ~50m distal lobe interval in Subunit III-D. The darker colors correspond with intervals of coarser material, where debrites are black and fine-grained turbidites are the lightest gray. White intervals are tephra or hemipelagic mud. Width of lobe systems in this visualization corresponds to facies outlined in Figure 35 (distal lobe, intermediate lobe, proximal lobe, channel-lobe transition, and channel facies), where distal lobe facies are narrow intervals and the widest portions of the column are channel facies. See Supplemental Material for core summary column details.

Figure 31. A detailed look at Lobe System 12, which is the last before arc rifting thought to have begun at the Unit III-Unit II boundary at the top of the system. The darker colors correspond with intervals of coarser material, where debrites are black and fine-grained turbidites are the lightest gray. White intervals are tephra or hemipelagic mud. Width of lobe systems in this visualization corresponds to facies outlined in Figure 35 (distal lobe, intermediate lobe, proximal lobe, channel-lobe transition, and channel facies), where distal lobe facies are narrow intervals and the widest portions of the column are channel facies. See Supplemental Material for core summary column details.

Figure 32. Digital elevation model for Anatahan Island, a modern analogue for Kyushu Palau Ridge sediment accumulation. The white circle represents the volcaniclastic apron

and black arrows denote the travel direction of slope-apron failures. Location within Mariana Arc (Figure 1) is indicated on right. Figures slightly modified from Chadwick et al. (2005).

Figure 33. An analogue for Site U1438 depositional setting is shown on the left Google Earth image (source of data in center, and scale on lower left) from the West Mariana Ridge, a channelized submarine ridge that rifted from the active Mariana arc. Scaled map of Anatahan Island and location map on right are the same as those shown in Figure 32 from Chadwick et al. (2005). Note that red star on map approximates the location of Google image.

Figure 34. Schematic block-diagram model for depositional processes of Site U1438 sediment. Vertical scale is exaggerated.

Figure 35. Schematic distribution of lobe facies based on descriptions by Mutti and Normark (1987) in Figure 7, and applied in Figures 27-31 and 36. Letters are Pickering and Hiscott (1986) facies classes affiliated with each lobe facies.

Figure 36. Overview of the distribution of identified Unit III channel-lobe systems and their correlated facies and subunits. The darker colors correspond with intervals of coarser material, where debrites are black and fine-grained turbidites are the lightest gray. White intervals are tuff or hemipelagic mudstone. Width of lobe systems in this visualization corresponds to facies outlined in Figure 35 (distal lobe, intermediate lobe, proximal lobe, channel-lobe transition, and channel facies), where distal lobe facies are narrow and the widest portions of the column are channel facies. Each lobe system is detailed further in Figures 27-31. On the right

side is the developmental and depositional timeline for Site U1438 and lines correlate to the stratigraphic location.

Figure 37. Map showing possible sources of sediment deposited at Site U1438. A is from seamounts to the southwest of U1438. B and C are two possible input directions from the nearest segment of the Kyushu Palau Ridge (KPR). D and E potential input directions are from distal portions of the KPR. Map is courtesy of Osamu Ishizuka with ages of dredge samples as indicated.

APPENDIX B: FIGURES

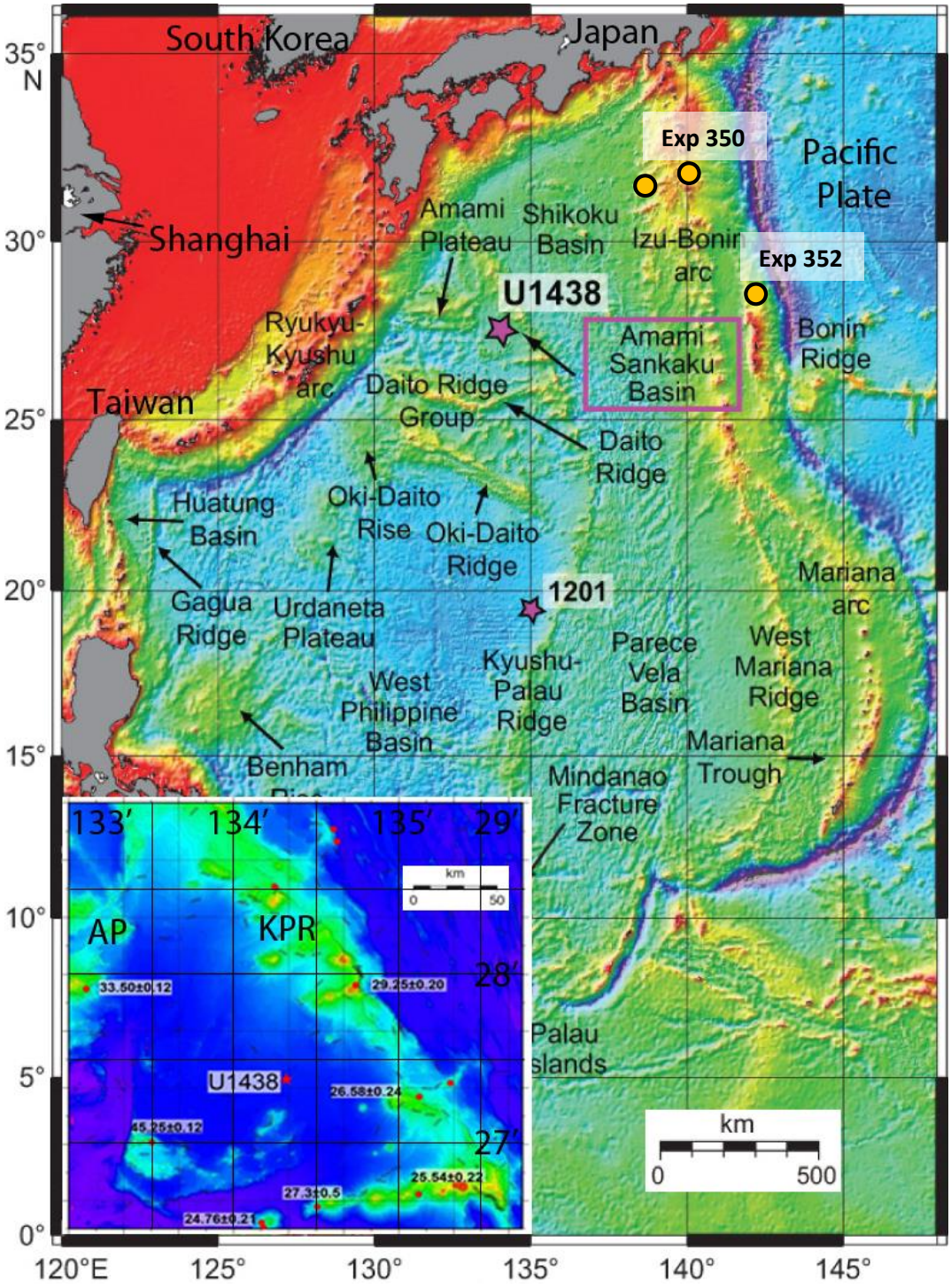

Figure 1

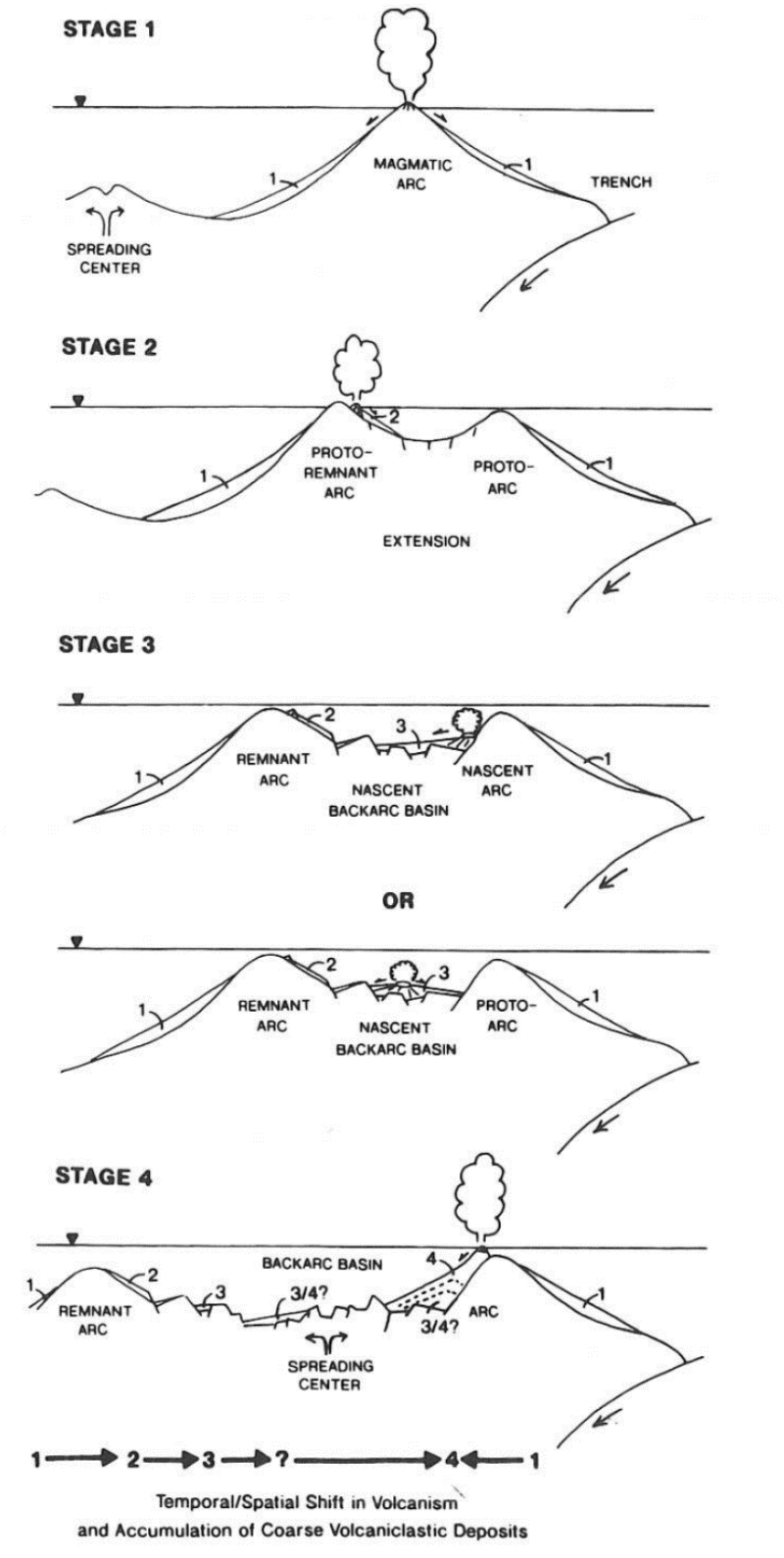
STAGE 1
MAGMATIC ARC
TRENCH
SPREADING CENTER
STAGE 2
PROTO-REMNANT ARC
PROTO-ARC
EXTENSION
STAGE 3
REMNANT ARC
NASCENT BACKARC BASIN
NASCENT ARC
OR
REMNANT ARC
NASCENT BACKARC BASIN
PROTO-ARC
STAGE 4
BACKARC BASIN
REMNANT ARC
3/4?
3/4?
ARC
SPREADING CENTER
1 → 2 → 3 → ? → 4 ← 1
Temporal/Spatial Shift in Volcanism
and Accumulation of Coarse Volcaniclastic Deposits

Figure 2

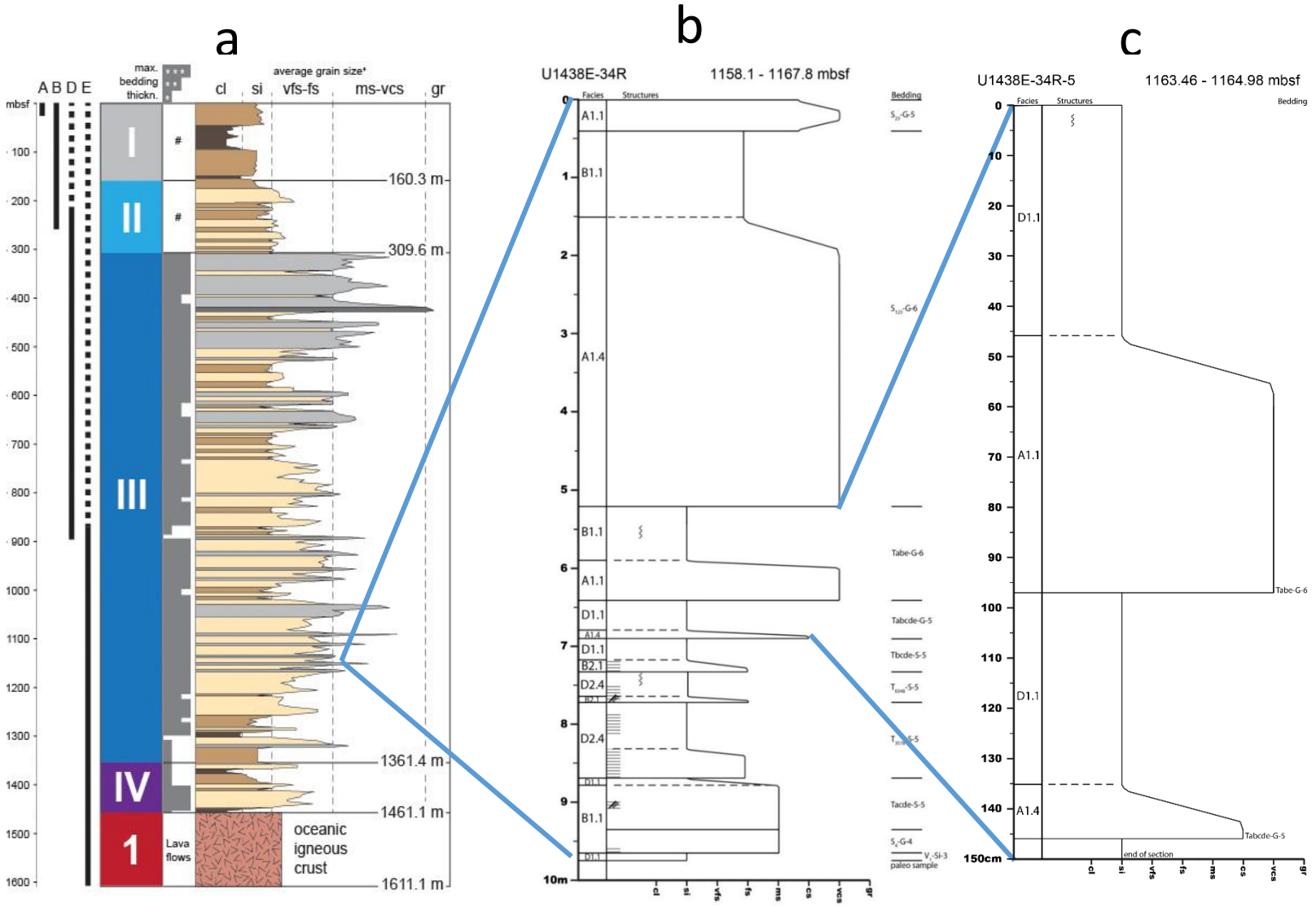
a
b
c
A B D E
max. bedding thickn.
average grain size*
cl
si
vfs-fs
ms-vcs
gr
mbsf
I
II
III
IV
1
Lava flows
160.3 m
309.6 m
1361.4 m
1461.1 m
1611.1 m
oceanic igneous crust
U1438E-34R
1158.1 - 1167.8 mbsf
Facies
Structures
Bedding
A1.1
B1.1
A1.4
D1.1
B2.1
D2.4
10m
U1438E-34R-5
1163.46 - 1164.98 mbsf
Tabe-G-6
Tabcde-G-5
Tbcde-S-5
Tacde-S-5
S2-G-4
paleo sample
end of section
150cm

Figure 3

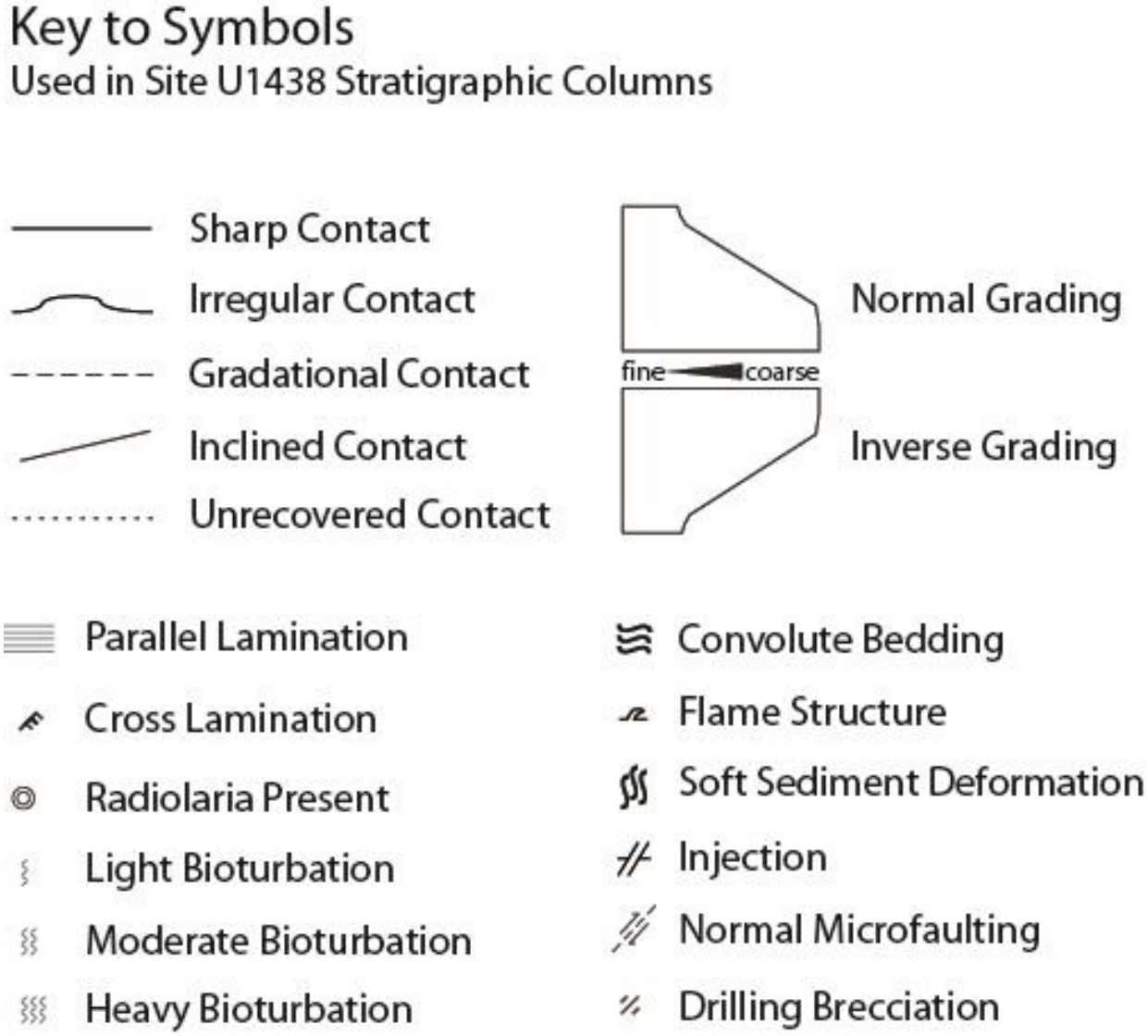
Key to Symbols
Used in Site U1438 Stratigraphic Columns
Sharp Contact
Irregular Contact
Gradational Contact
Inclined Contact
Unrecovered Contact
fine
coarse
Normal Grading
Inverse Grading
Parallel Lamination
Cross Lamination
Radiolaria Present
Light Bioturbation
Moderate Bioturbation
Heavy Bioturbation
Convolute Bedding
Flame Structure
Soft Sediment Deformation
Injection
Normal Microfaulting
Drilling Brecciation

Figure 4

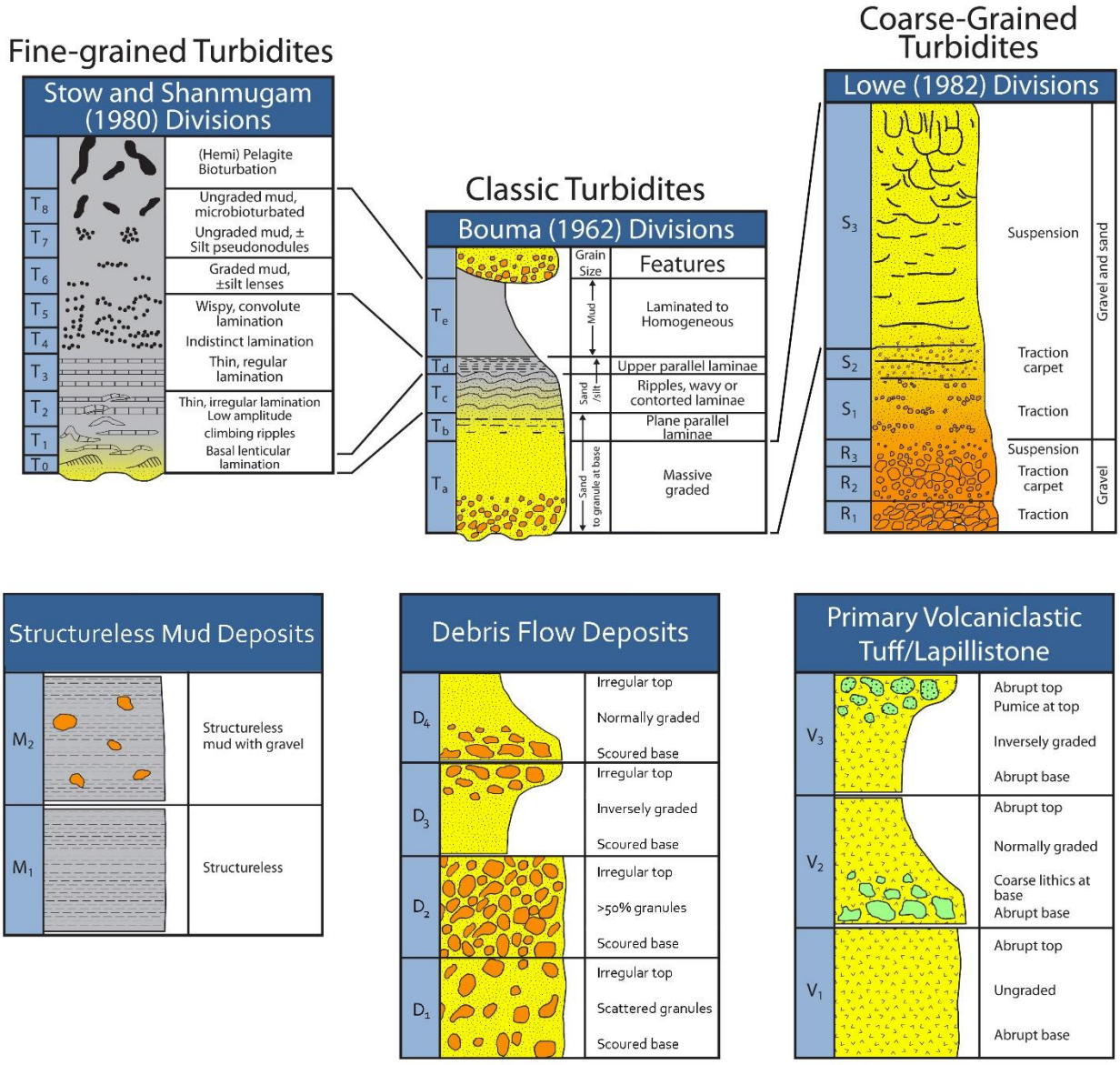
Fine-grained Turbidites
Stow and Shanmugam (1980) Divisions
(Hemi) Pelagite Bioturbation
T8
T7
T6
T5
T4
T3
T2
T1
T0
Ungraded mud, microbioturbated
Ungraded mud, ± Silt pseudonodules
Graded mud, ±silt lenses
Wispy, convolute lamination
Indistinct lamination
Thin, regular lamination
Thin, irregular lamination
Low amplitude climbing ripples
Basal lenticular lamination
Classic Turbidites
Bouma (1962) Divisions
Grain Size
Features
Te
Td
Tc
Tb
Ta
Mud
Sand /silt
Sand to granule at base
Laminated to Homogeneous
Upper parallel laminae
Ripples, wavy or contorted laminae
Plane parallel laminae
Massive graded
Coarse-Grained Turbidites
Lowe (1982) Divisions
S3
S2
S1
R3
R2
R1
Suspension
Traction carpet
Traction
Suspension
Traction carpet
Traction
Gravel and sand
Gravel
Structureless Mud Deposits
M2
M1
Structureless mud with gravel
Structureless
Debris Flow Deposits
D4
D3
D2
D1
Irregular top
Normally graded
Scoured base
Irregular top
Inversely graded
Scoured base
Irregular top
>50% granules
Scoured base
Irregular top
Scattered granules
Scoured base
Primary Volcaniclastic Tuff/Lapillistone
V3
V2
V1
Abrupt top
Pumice at top
Inversely graded
Abrupt base
Abrupt top
Normally graded
Coarse lithics at base
Abrupt base
Abrupt top
Ungraded
Abrupt base

Figure 5

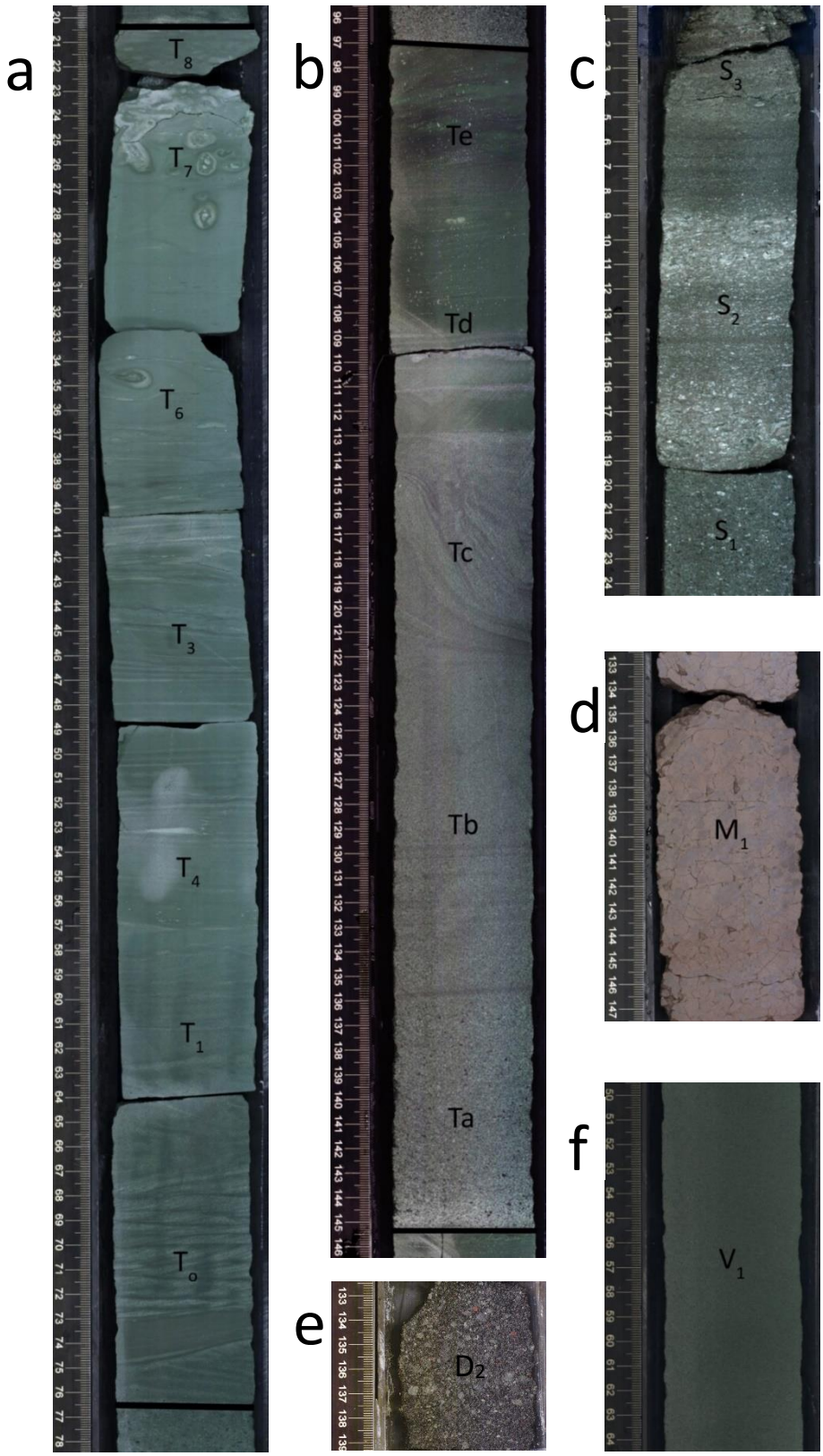

Figure 6

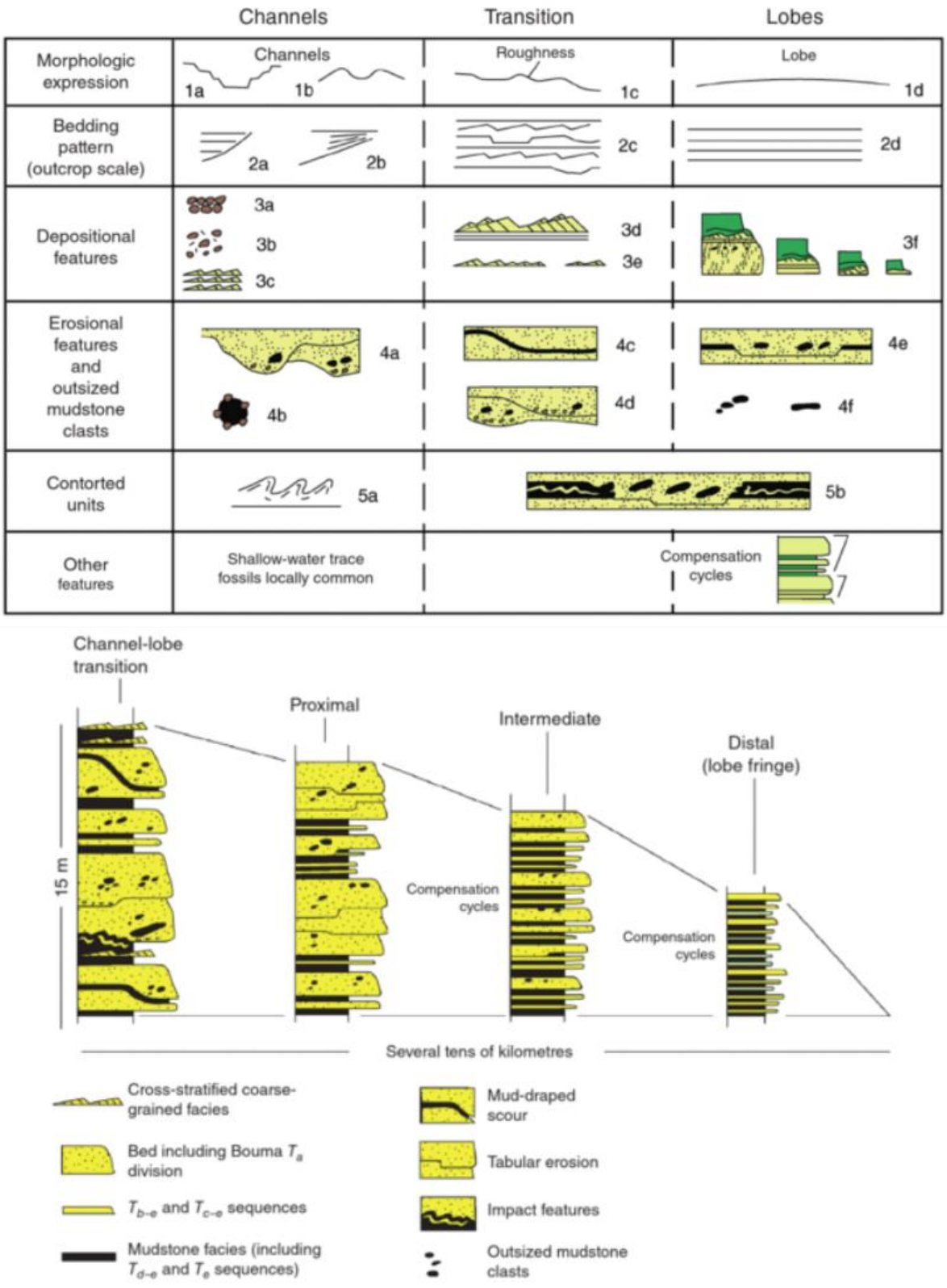
Channels
Transition
Lobes
Morphologic expression
Channels
Roughness
Lobe
1a
1b
1c
1d
Bedding pattern (outcrop scale)
2a
2b
2c
2d
Depositional features
3a
3b
3c
3d
3e
3f
Erosional features and outsized mudstone clasts
4a
4b
4c
4d
4e
4f
Contorted units
5a
5b
Other features
Shallow-water trace fossils locally common
Compensation cycles
Channel-lobe transition
Proximal
Intermediate
Distal (lobe fringe)
15 m
Compensation cycles
Compensation cycles
Several tens of kilometres
Cross-stratified coarse-grained facies
Bed including Bouma T_a division
T_{b-e} and T_{c-e} sequences
Mudstone facies (including T_{d-e} and T_e sequences)
Mud-draped scour
Tabular erosion
Impact features
Outsized mudstone clasts

Figure 7

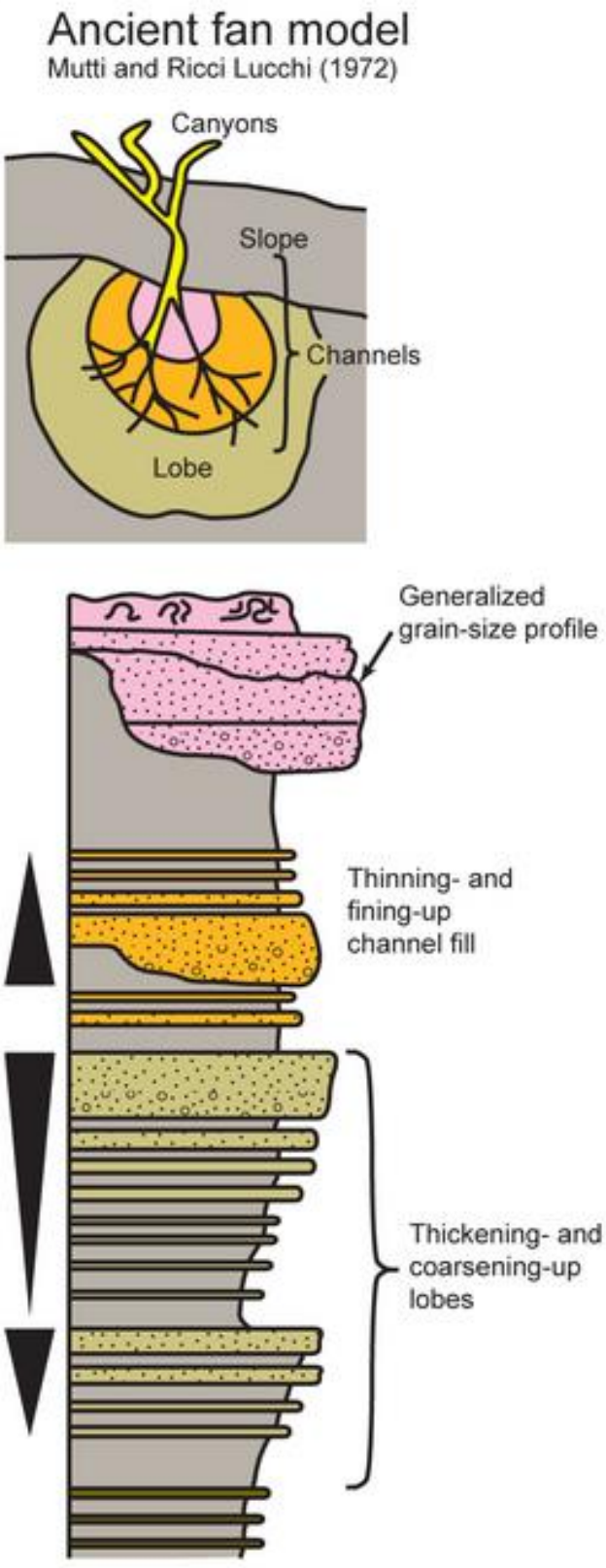
Ancient fan model
Mutti and Ricci Lucchi (1972)
Canyons
Slope
Channels
Lobe
Generalized
grain-size profile
Thinning- and
fining-up
channel fill
Thickening- and
coarsening-up
lobes

Figure 8

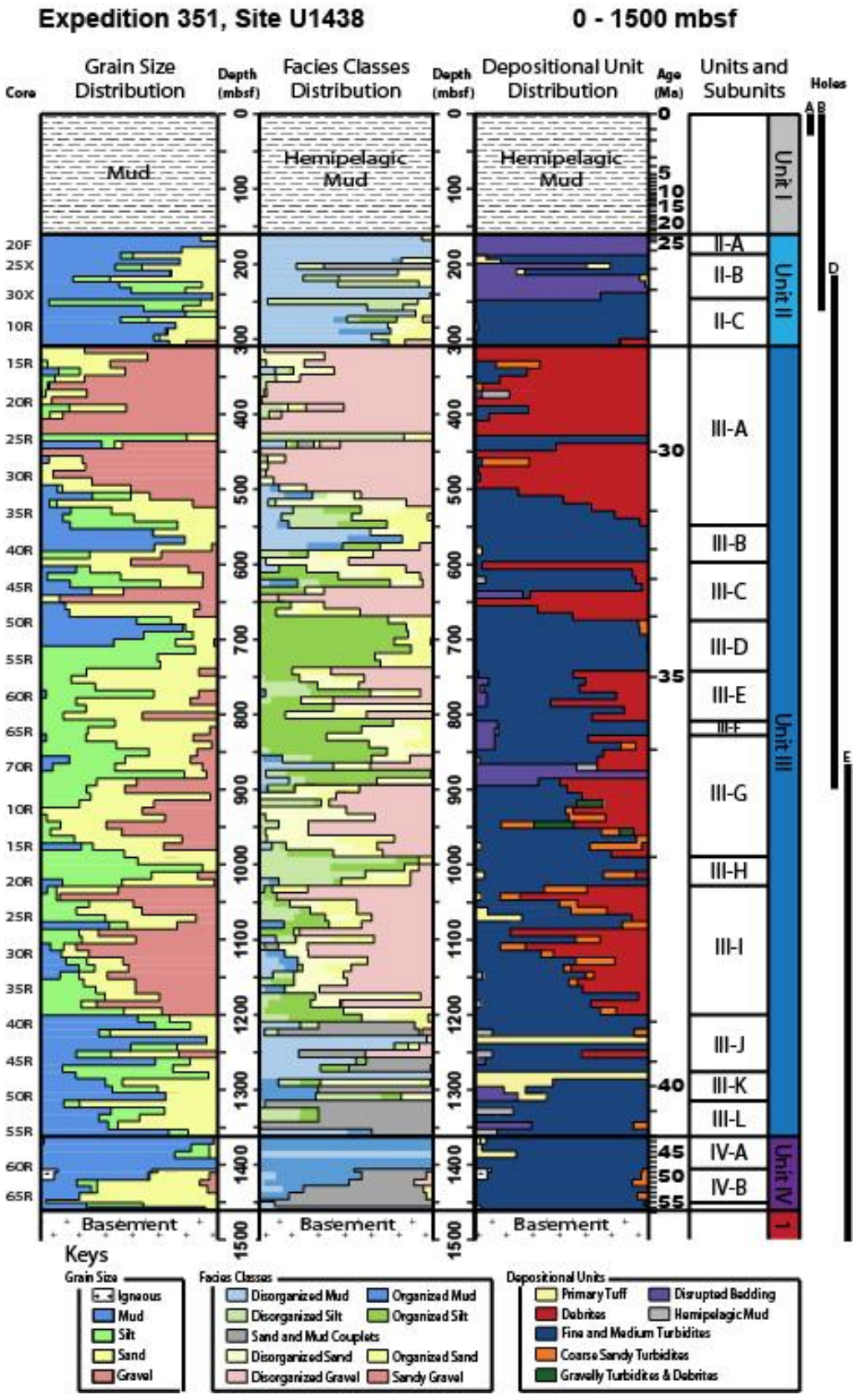
Expedition 351, Site U1438
0 - 1500 mbsf
Core
Grain Size Distribution
Depth (mbsf)
Facies Classes Distribution
Depth (mbsf)
Depositional Unit Distribution
Age (Ma)
Units and Subunits
Holes
Mud
Hemipelagic Mud
Hemipelagic Mud
Unit I
Unit II
Unit III
Unit IV
II-A
II-B
II-C
III-A
III-B
III-C
III-D
III-E
III-F
III-G
III-H
III-I
III-J
III-K
III-L
IV-A
IV-B
Basement
Basement
Basement
Keys
Grain Size
Igneous
Mud
Silt
Sand
Gravel
Facies Classes
Disorganized Mud
Organized Mud
Disorganized Silt
Organized Silt
Sand and Mud Couplets
Disorganized Sand
Organized Sand
Disorganized Gravel
Sandy Gravel
Depositional Units
Primary Tuff
Disrupted Bedding
Debrites
Hemipelagic Mud
Fine and Medium Turbidites
Coarse Sandy Turbidites
Gravelly Turbidites & Debrites

Figure 9

Subunit III-L

a

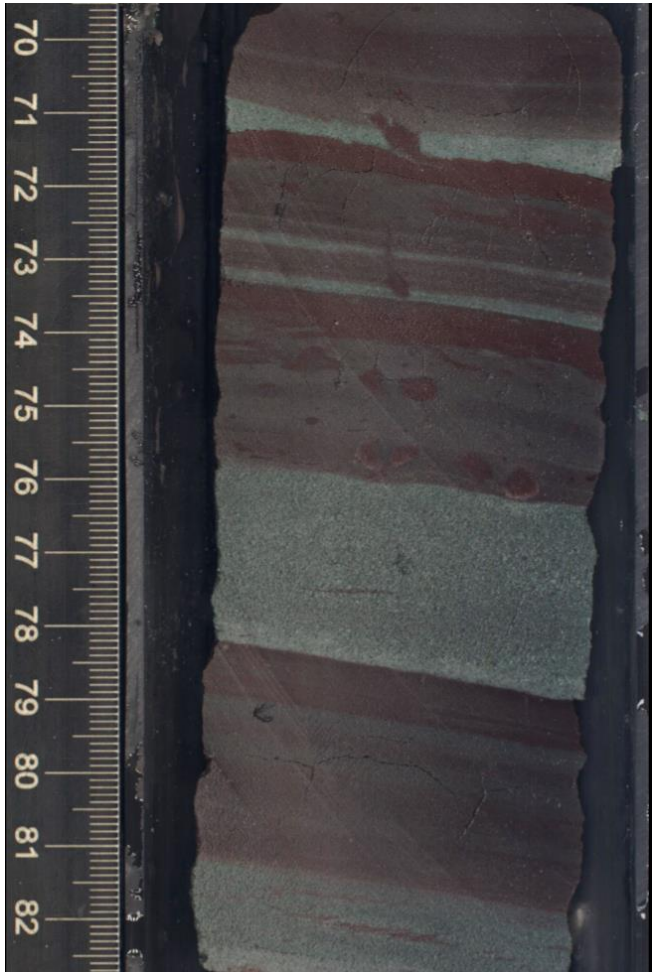

b

Figure 10

Subunit III-K

a

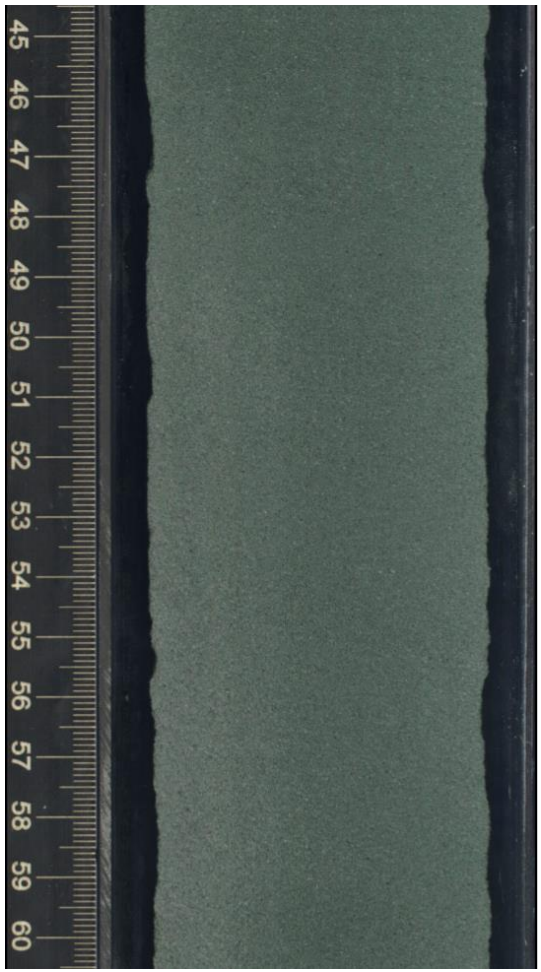

b

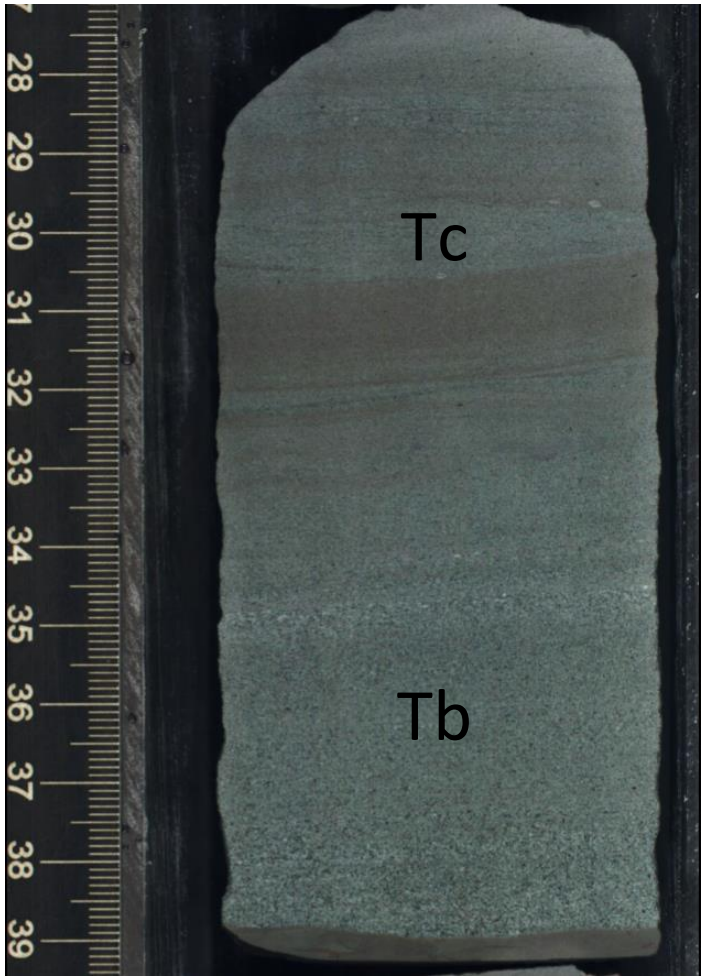

Figure 11

Subunit III-J

a

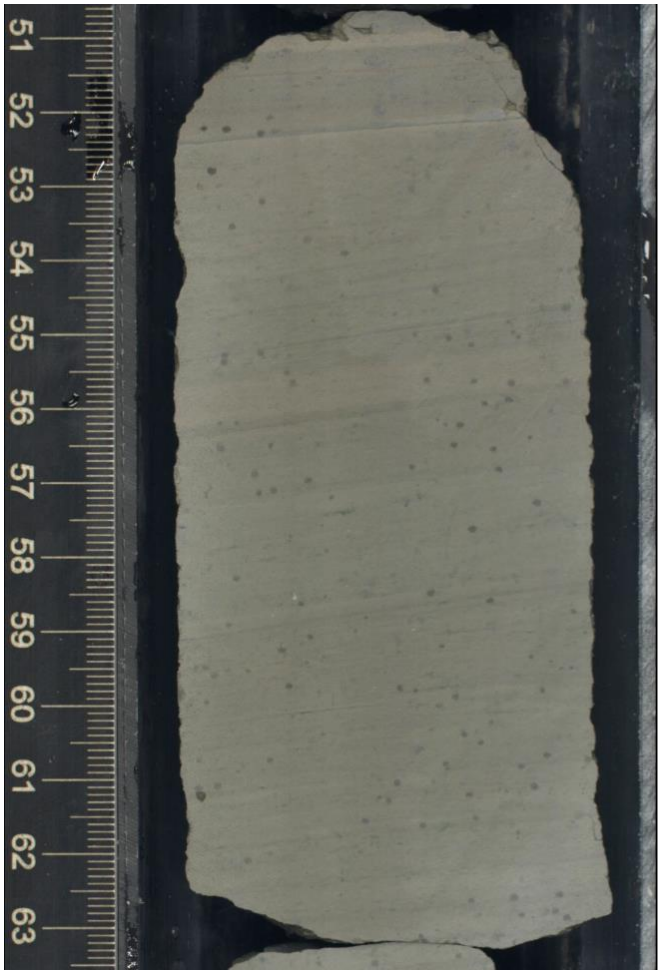

b

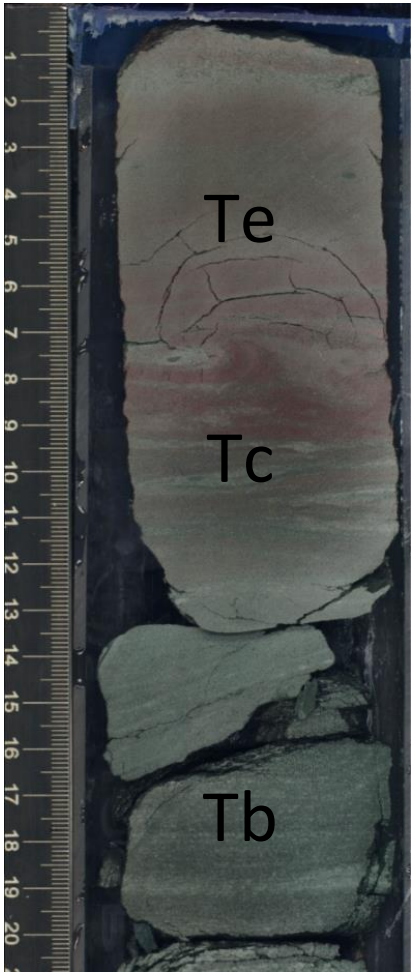

Figure 12

Subunit III-I

a

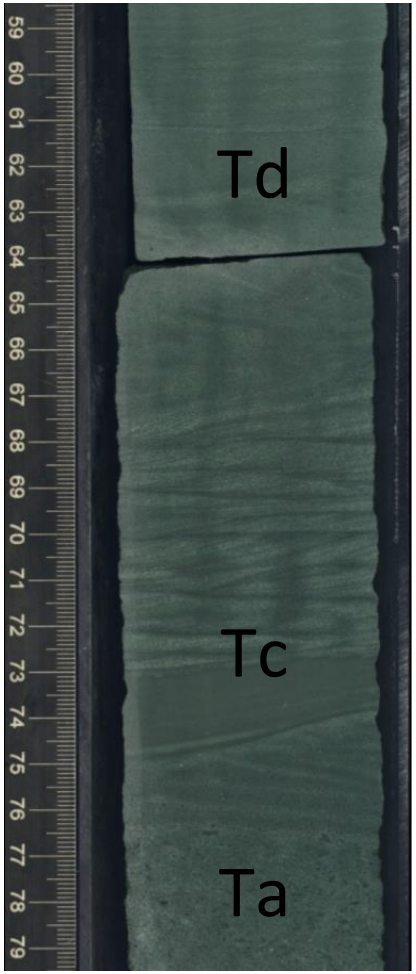

b

Figure 13

Subunit III-H

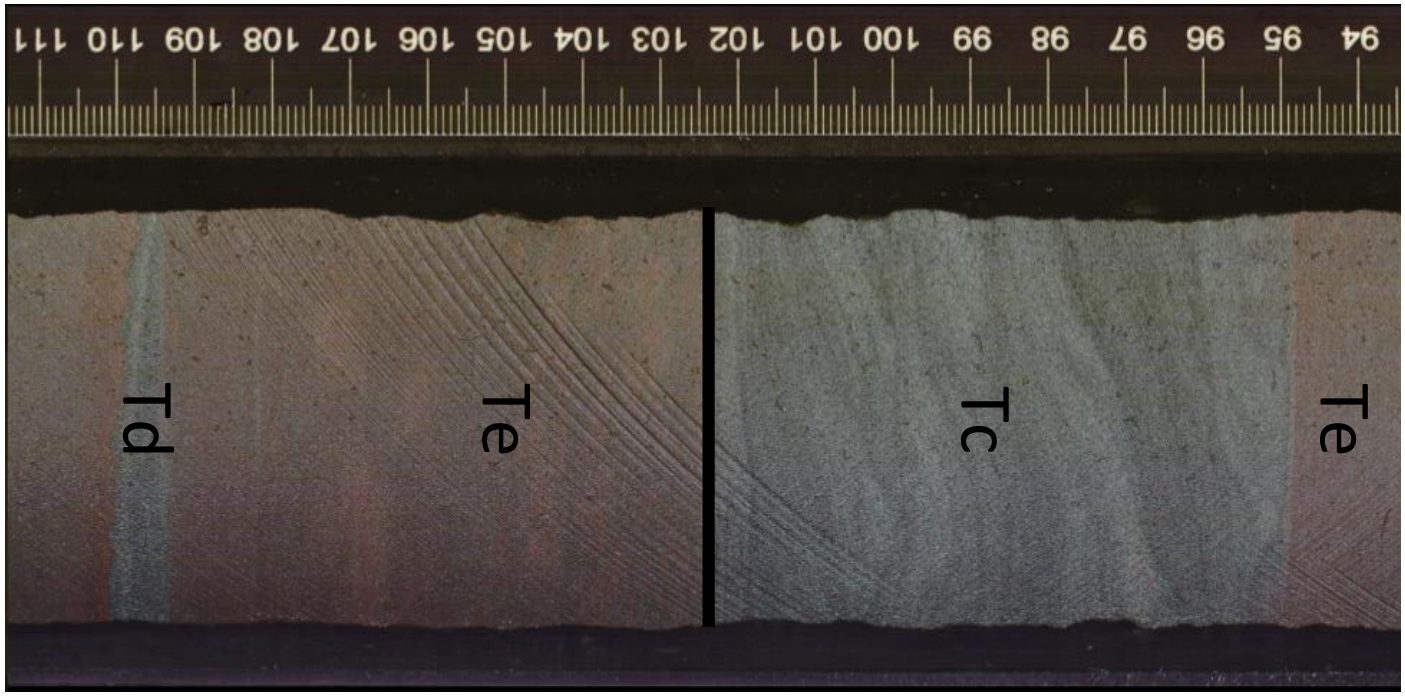

Figure 14

Subunit III-G

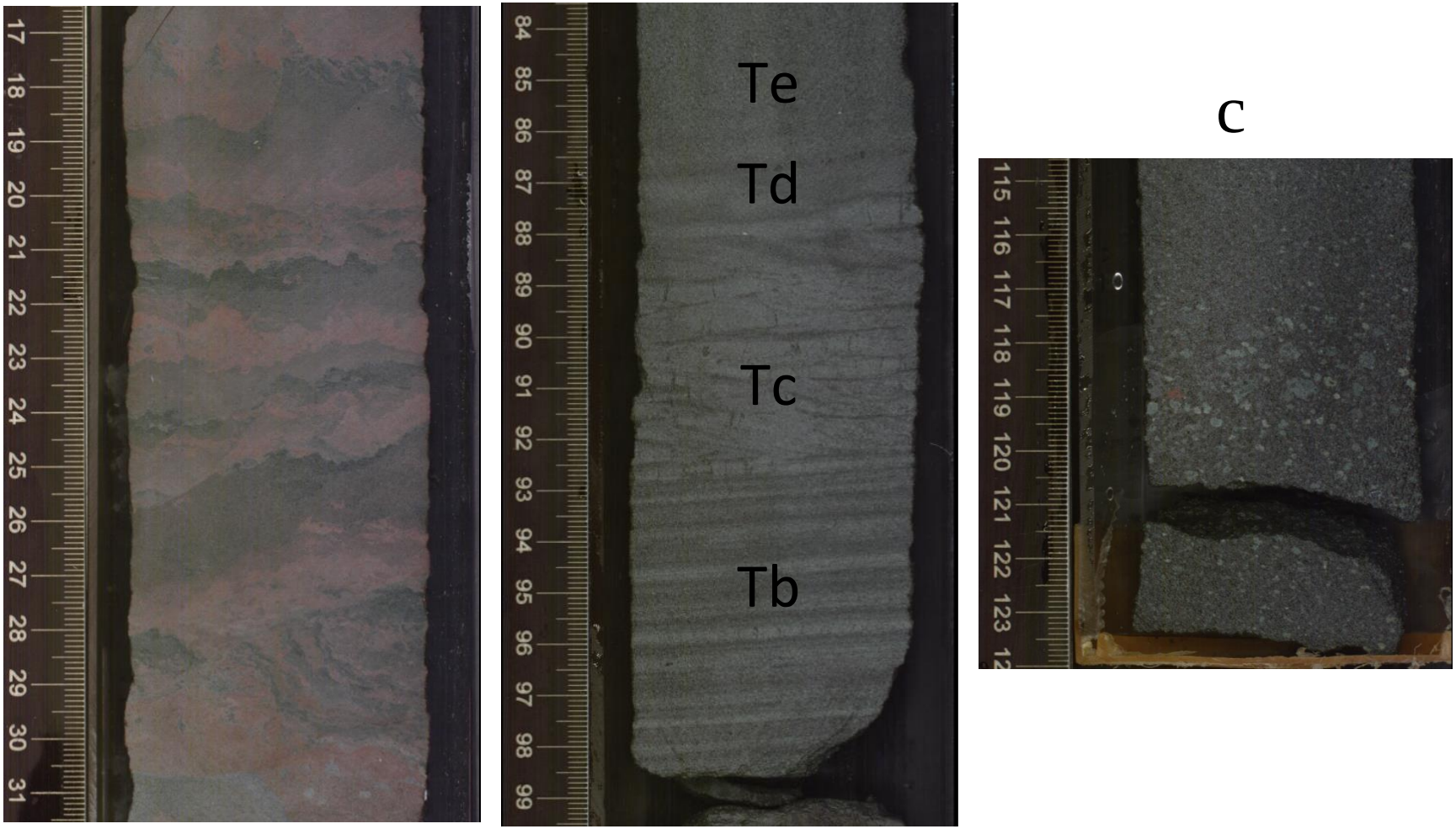

Figure 15

Subunit III-F

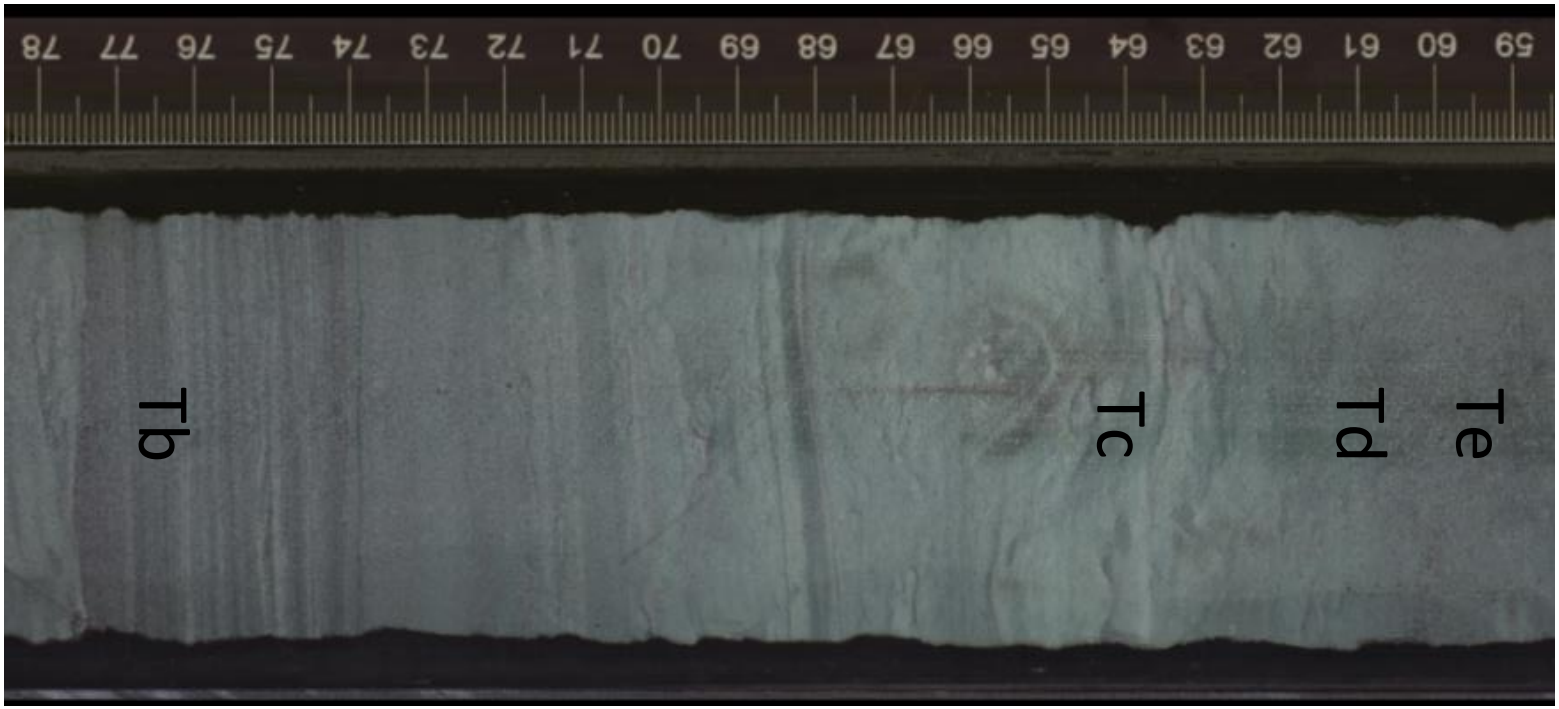

Figure 16

Subunit III-E

a

b

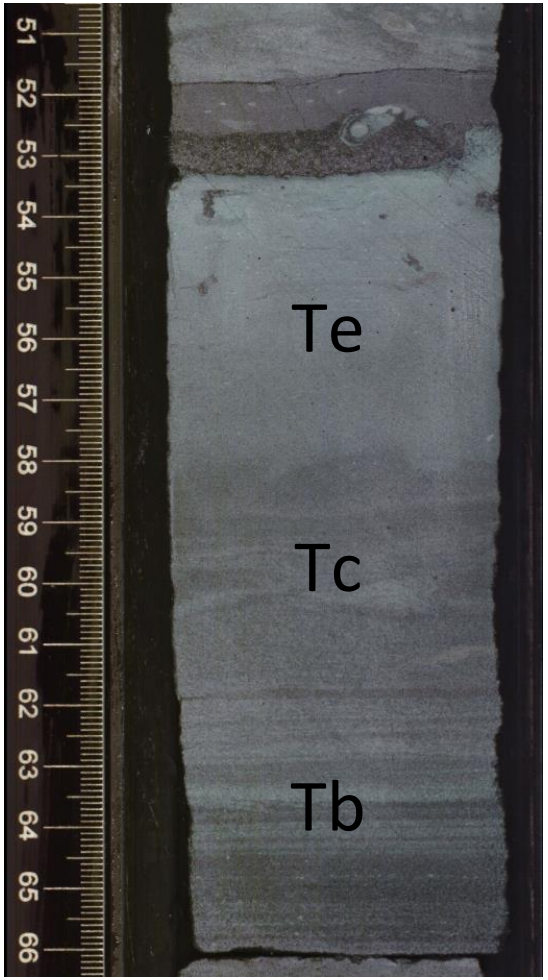

Figure 17

Subunit III-D

a

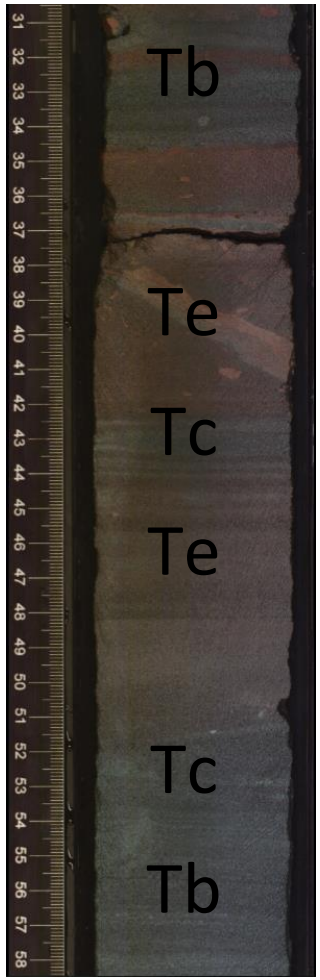

b

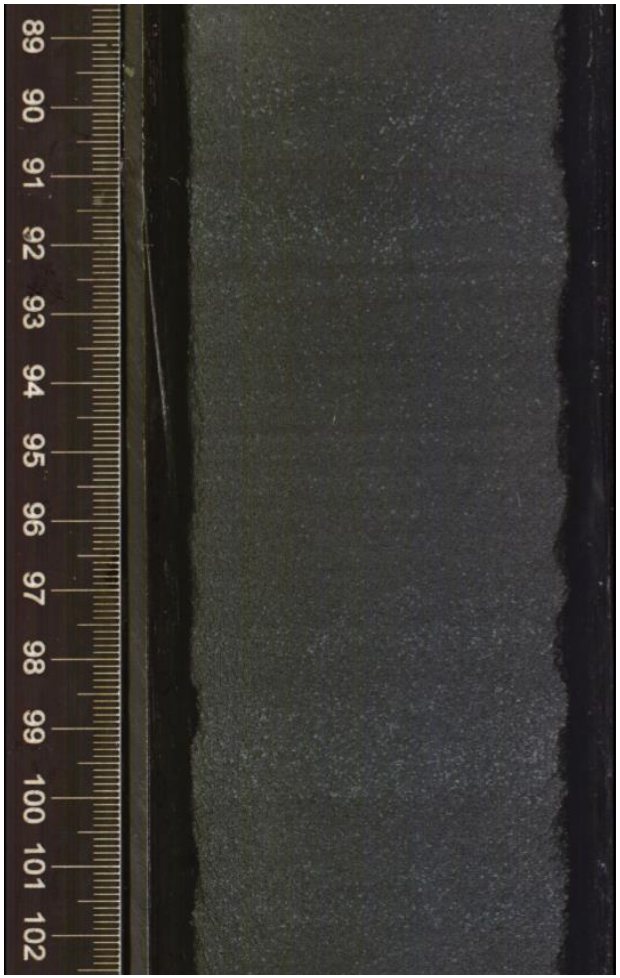

Figure 18

Subunit III-C

a

b

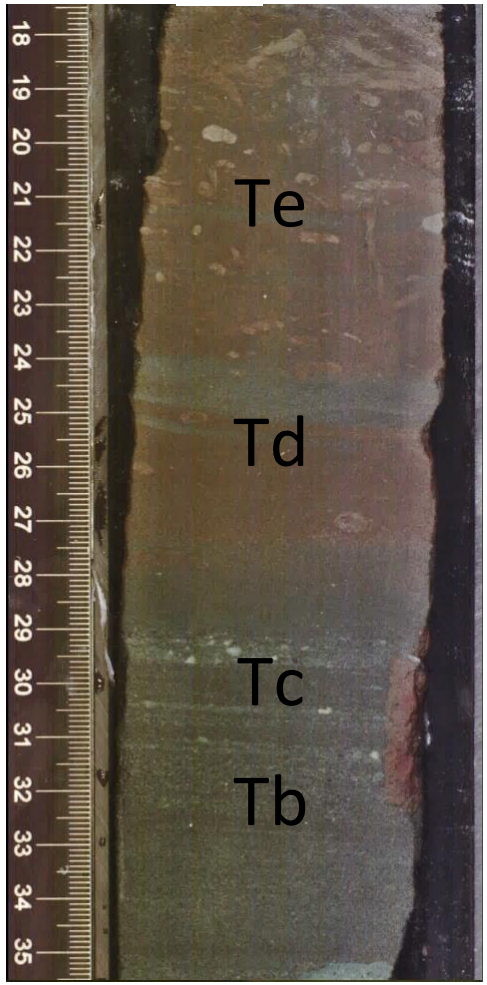

Figure 19

Subunit III-B

a

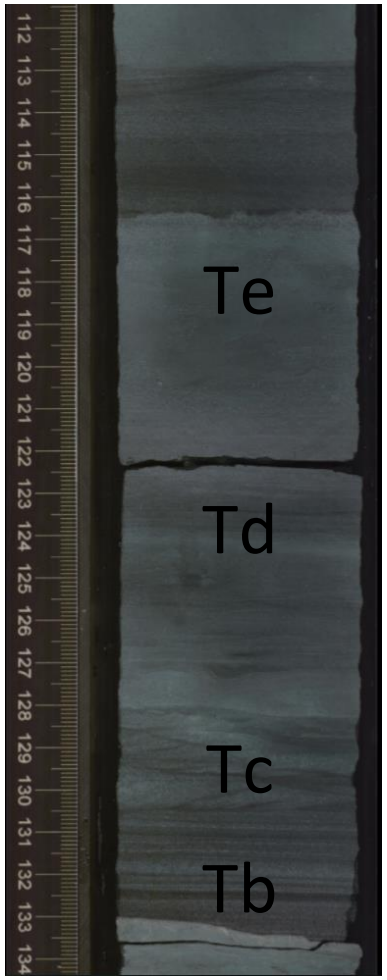

b

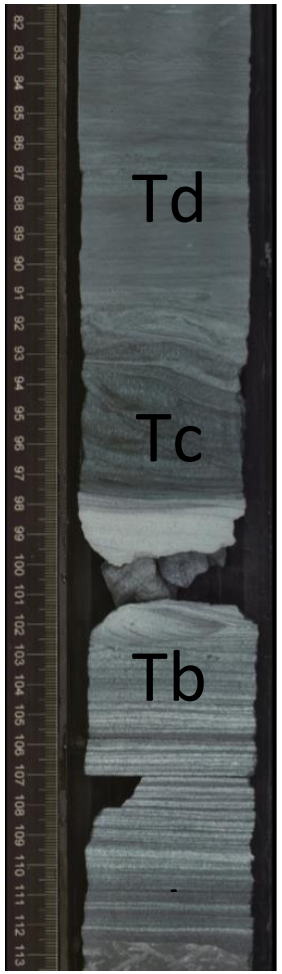

Figure 20

Subunit III-A

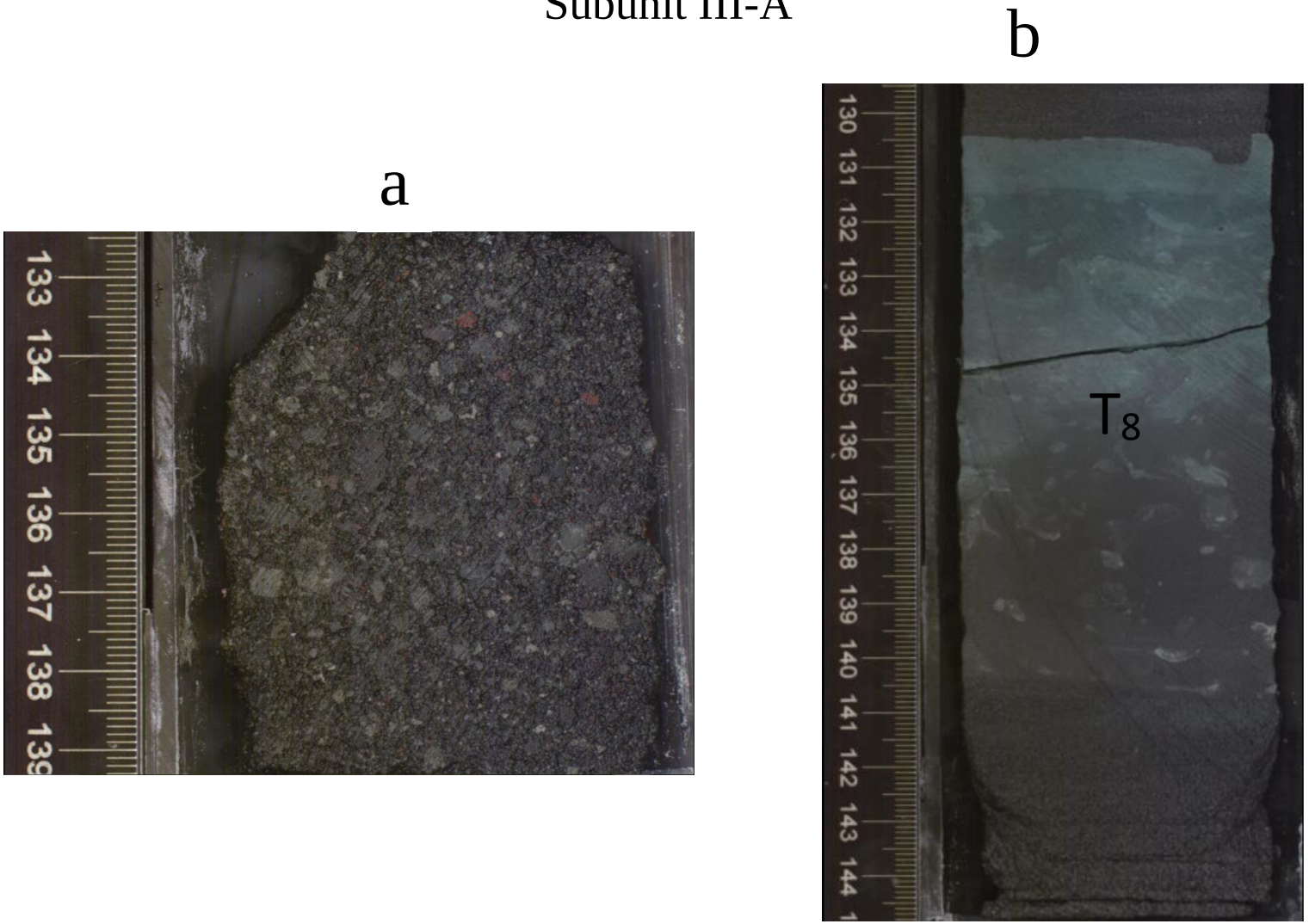

Figure 21

Unit III – Unit II Boundary

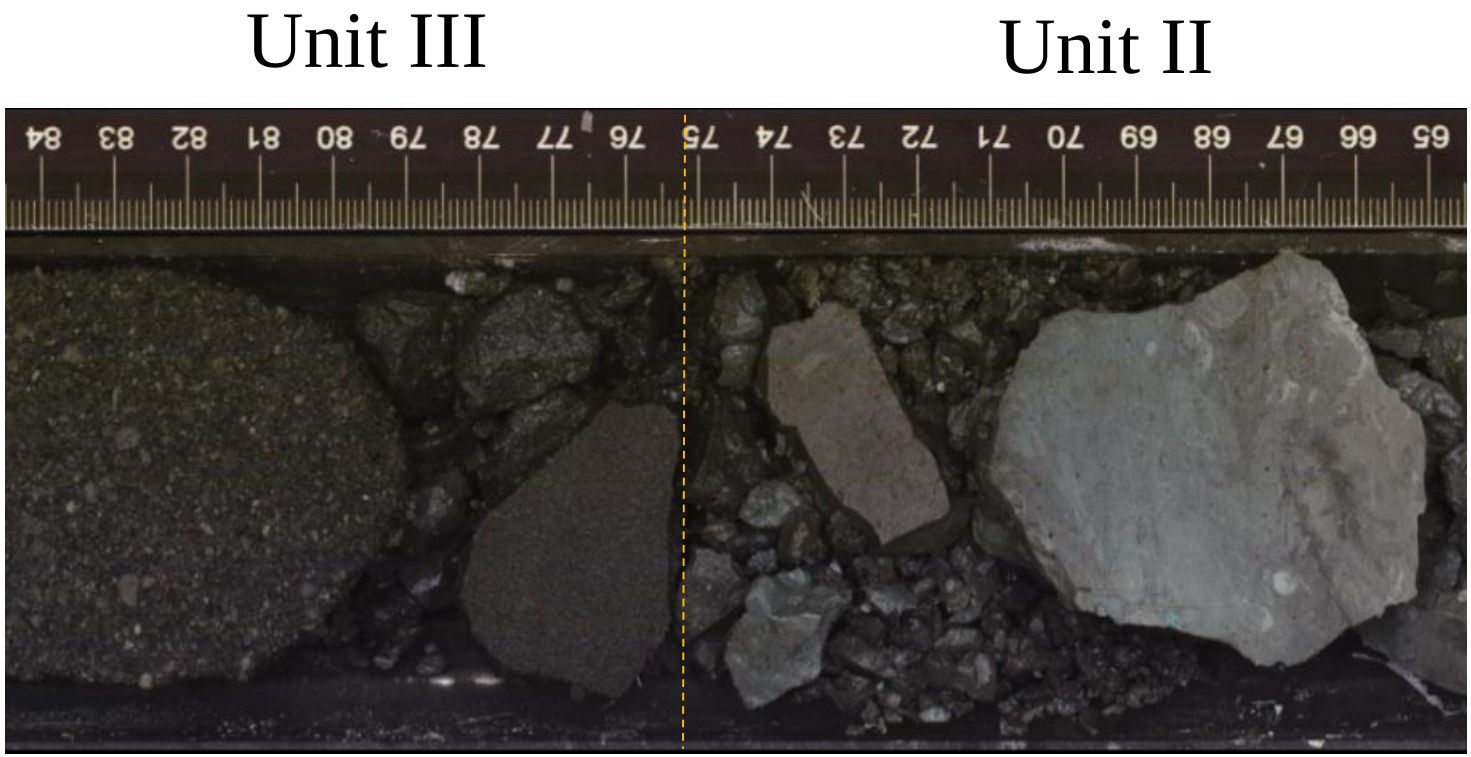

Figure 22

Subunit II-C

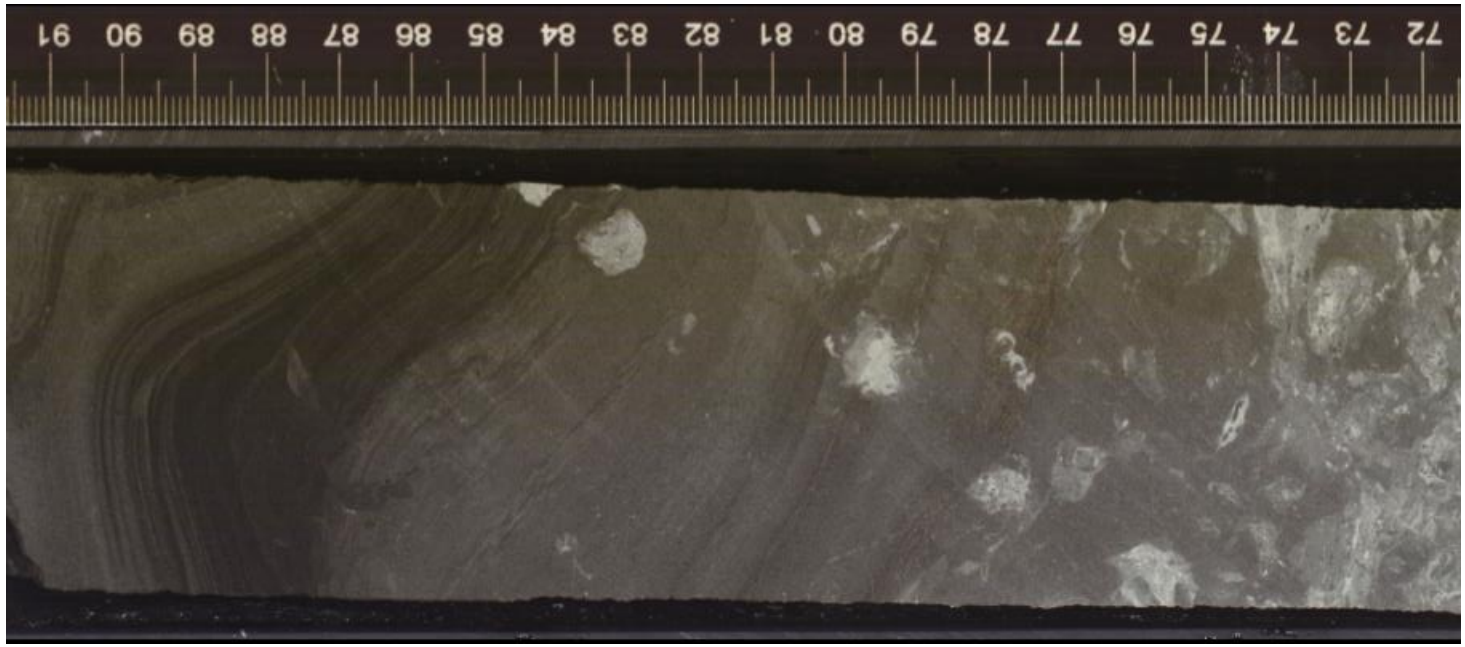

Figure 23

Subunit II-B

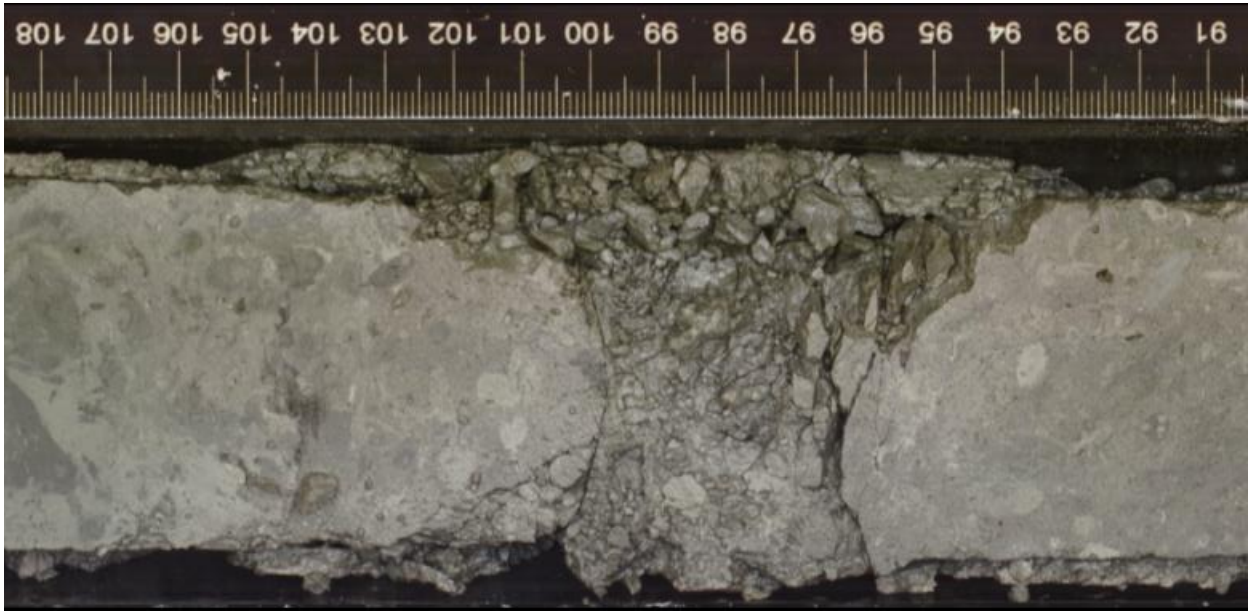

Figure 24

Subunit II-A

a

b

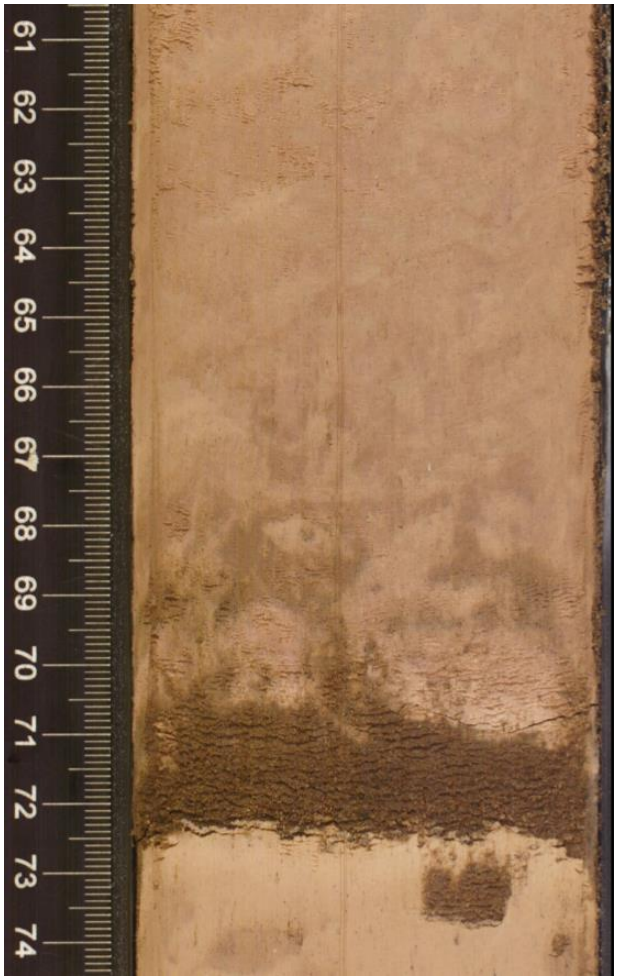

Figure 25

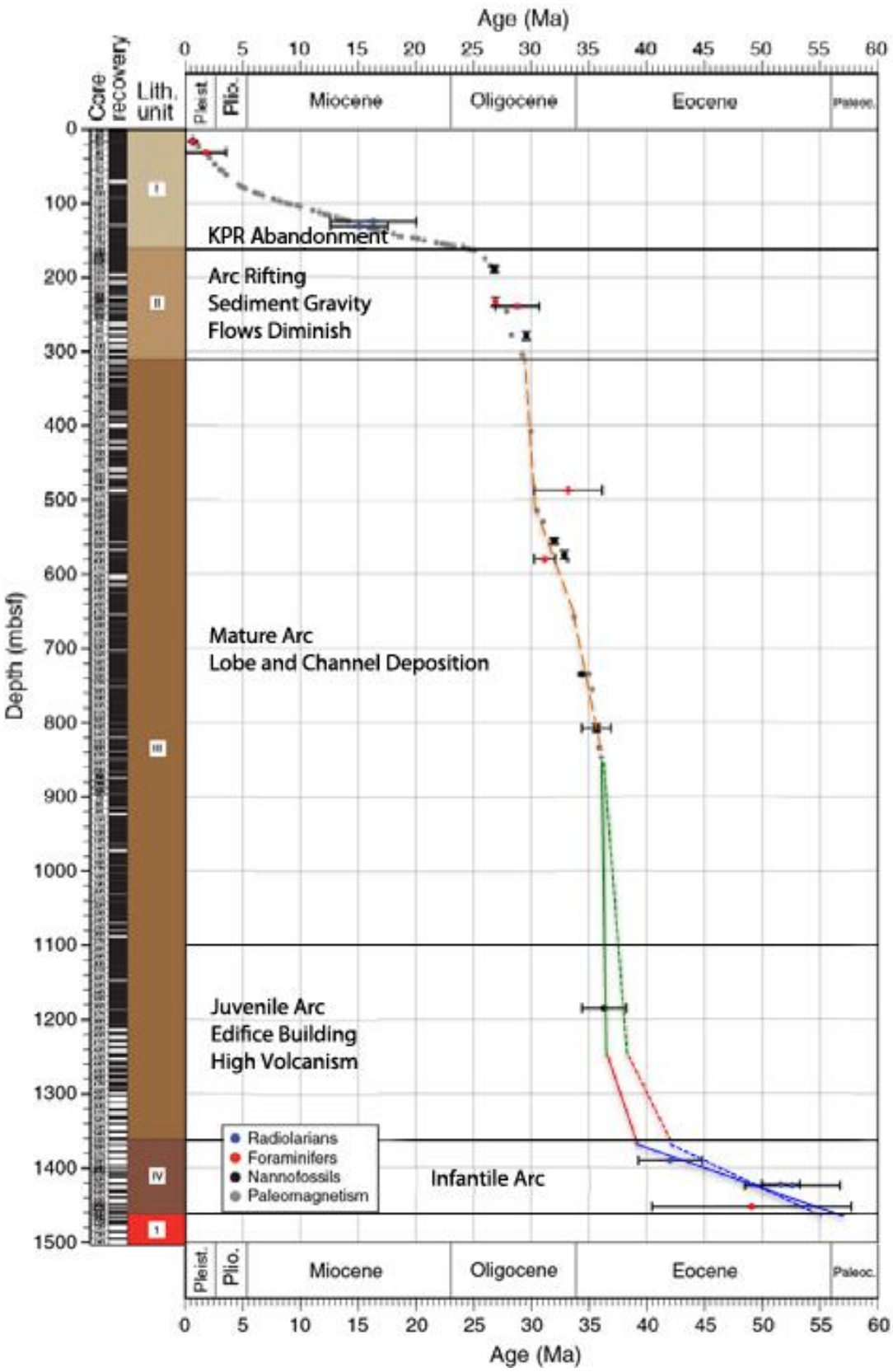
Age (Ma)
Core recovery
Lith. unit
Pleist.
Plio.
Miocene
Oligocene
Eocene
Paleoc.
KPR Abandonment
Arc Rifting
Sediment Gravity
Flows Diminish
Mature Arc
Lobe and Channel Deposition
Juvenile Arc
Edifice Building
High Volcanism
Infantile Arc
Radiolarians
Foraminifers
Nannofossils
Paleomagnetism
Depth (mbsf)

Figure 26

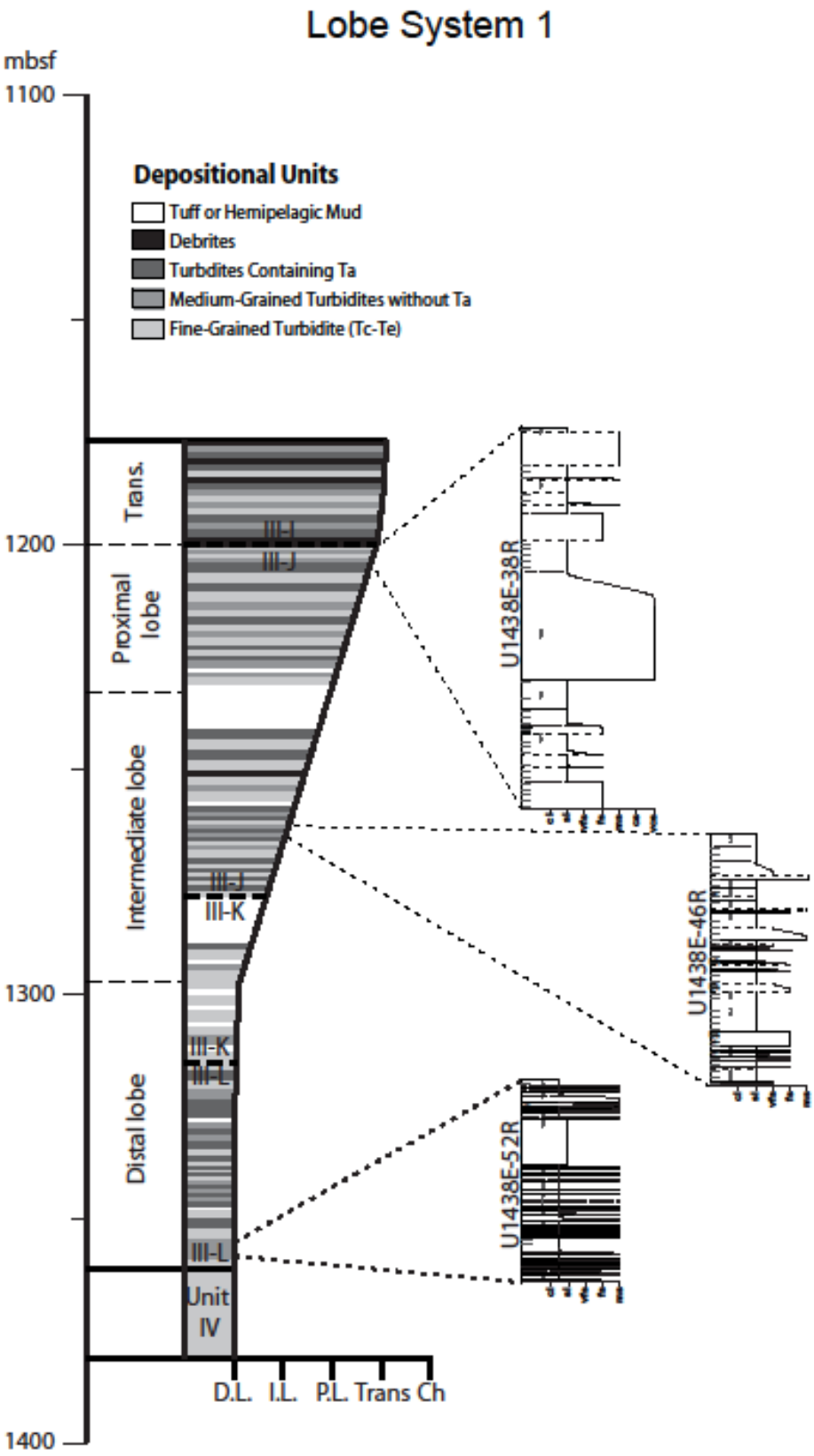
Lobe System 1
mbsf
1100
1200
1300
1400
Depositional Units
Tuff or Hemipelagic Mud
Debrites
Turbdites Containing Ta
Medium-Grained Turbidites without Ta
Fine-Grained Turbidite (Tc-Te)
Trans.
Proximal lobe
Intermediate lobe
Distal lobe
III-I
III-J
III-J
III-K
III-K
III-L
III-L
Unit IV
U1438E-38R
U1438E-46R
U1438E-52R
D.L.
I.L.
P.L.
Trans
Ch

Figure 27

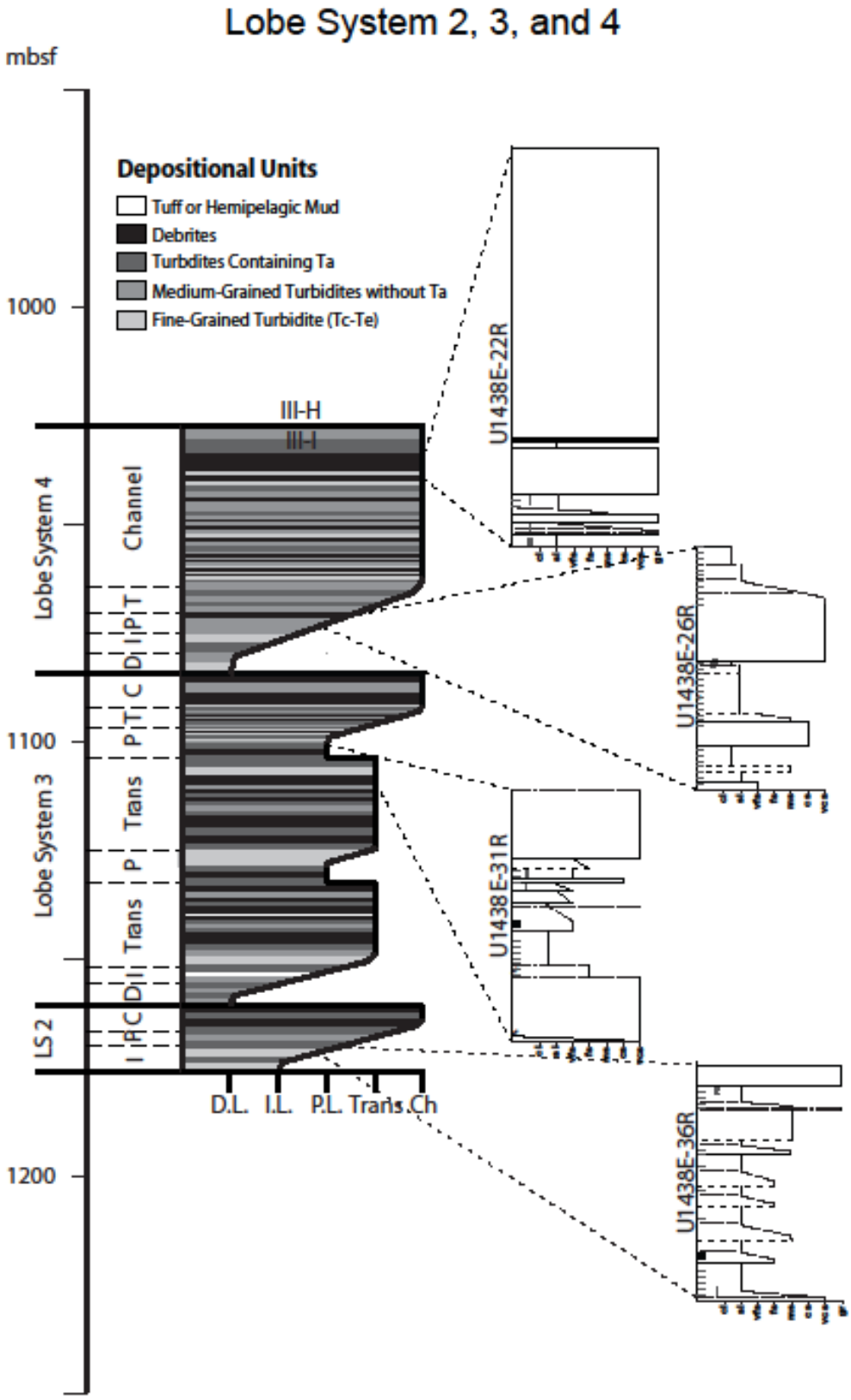
Lobe System 2, 3, and 4
mbsf
Depositional Units
Tuff or Hemipelagic Mud
Debrites
Turbdites Containing Ta
Medium-Grained Turbidites without Ta
Fine-Grained Turbidite (Tc-Te)
1000
1100
1200
III-H
III-I
Lobe System 4
Channel
T
P
D
Lobe System 3
C
T
P
Trans
P
Trans
D
I
LS 2
C
P
I
D.L.
I.L.
P.L.
Trans.
Ch
U1438E-22R
U1438E-26R
U1438E-31R
U1438E-36R

Figure 28

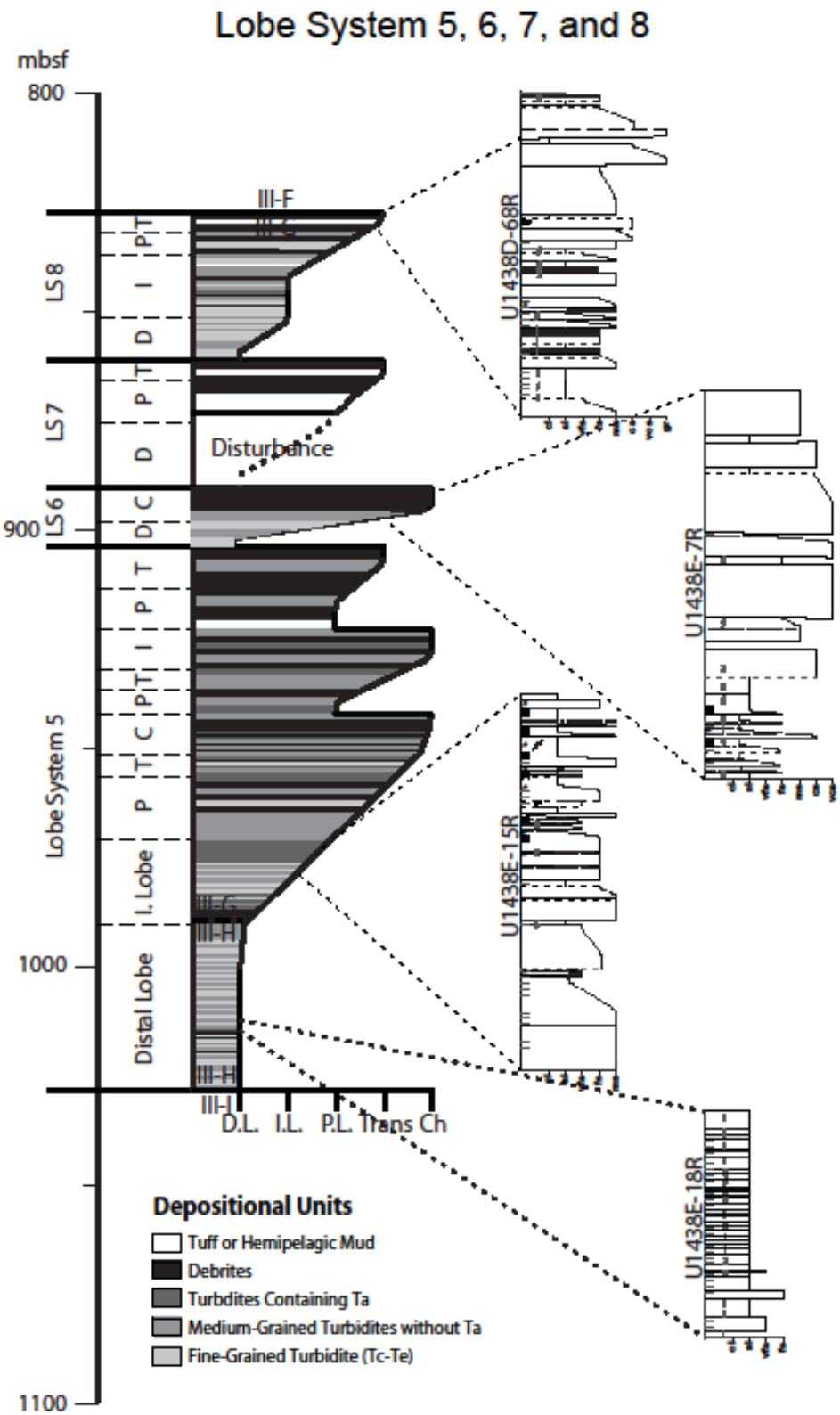
Lobe System 5, 6, 7, and 8
mbsf
800
900
1000
1100
LS8
LS7
LS6
Lobe System 5
I. Lobe
Distal Lobe
III-F
III-G
III-H
III-I
Disturbance
U1438D-68R
U1438E-7R
U1438E-15R
U1438E-18R
D.L.
I.L.
P.L.
Trans
Ch
Depositional Units
Tuff or Hemipelagic Mud
Debrites
Turbdites Containing Ta
Medium-Grained Turbidites without Ta
Fine-Grained Turbidite (Tc-Te)

Figure 29

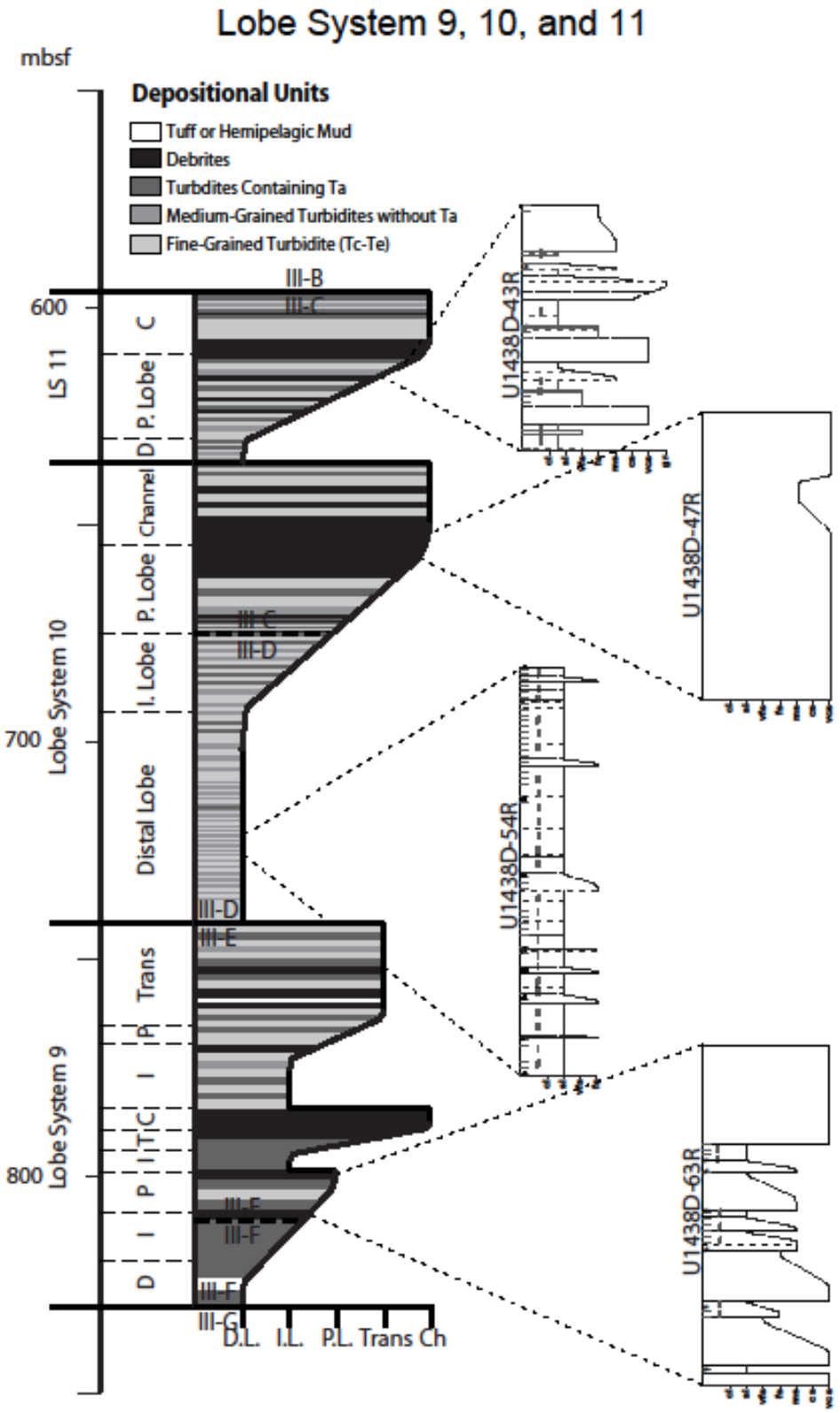
Lobe System 9, 10, and 11
mbsf
Depositional Units
Tuff or Hemipelagic Mud
Debrites
Turbdites Containing Ta
Medium-Grained Turbidites without Ta
Fine-Grained Turbidite (Tc-Te)
600
700
800
LS 11
Lobe System 10
Lobe System 9
C
P. Lobe
D
Channel
P. Lobe
I. Lobe
Distal Lobe
Trans
P
I
C
T
I
P
I
D
III-B
III-C
III-C
III-D
III-D
III-E
III-E
III-F
III-F
III-G
D.L. I.L. P.L. Trans Ch
U1438D-43R
U1438D-47R
U1438D-54R
U1438D-63R

Figure 30

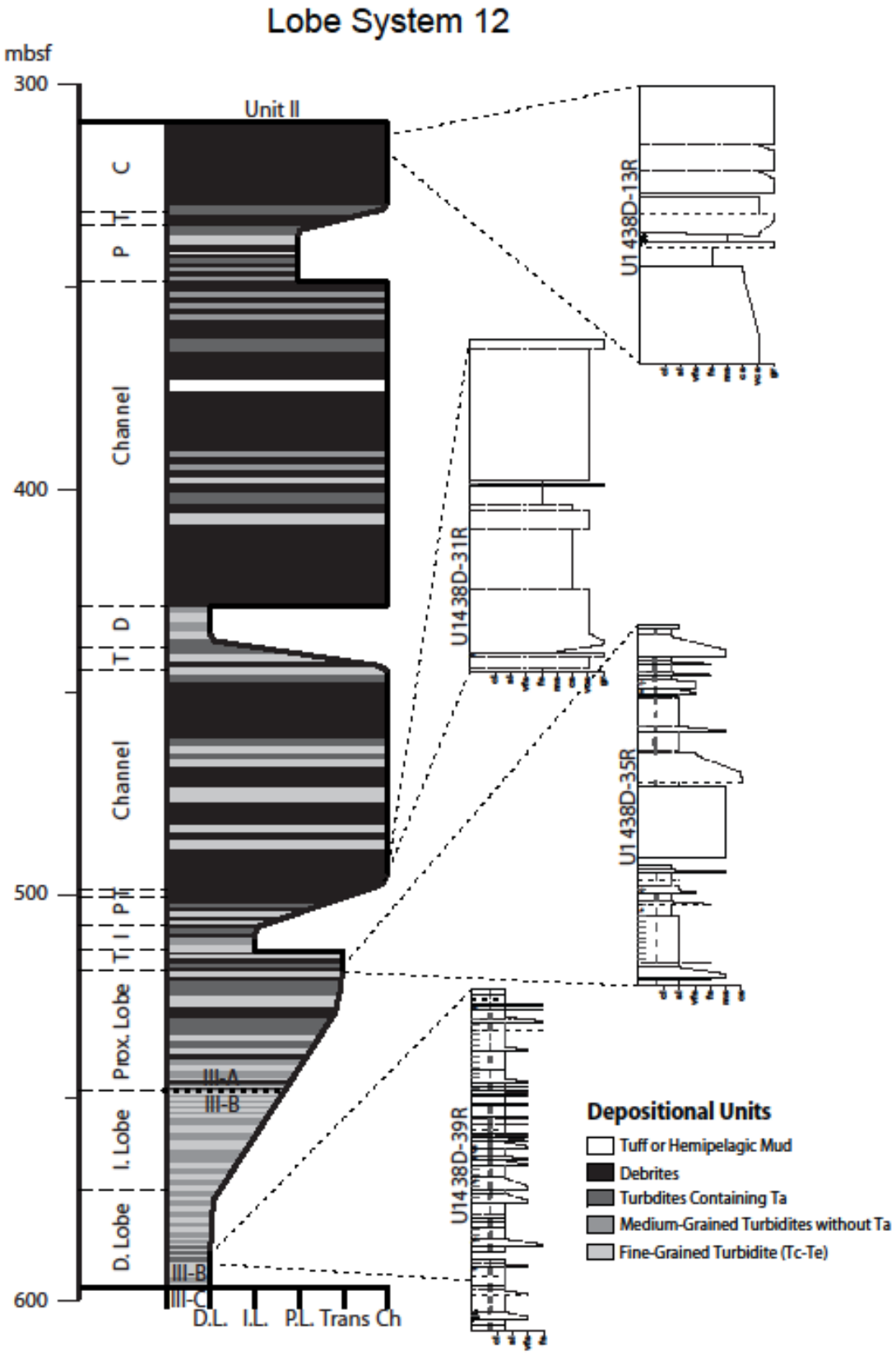
Lobe System 12
mbsf
300
400
500
600
Unit II
C
T
P
Channel
T
D
Channel
T
P
T
I
Prox. Lobe
III-A
III-B
I. Lobe
D. Lobe
III-B
III-C
D.L.
I.L.
P.L.
Trans Ch
U1438D-13R
U1438D-31R
U1438D-35R
U1438D-39R
Depositional Units
Tuff or Hemipelagic Mud
Debrites
Turbdites Containing Ta
Medium-Grained Turbidites without Ta
Fine-Grained Turbidite (Tc-Te)

Figure 31

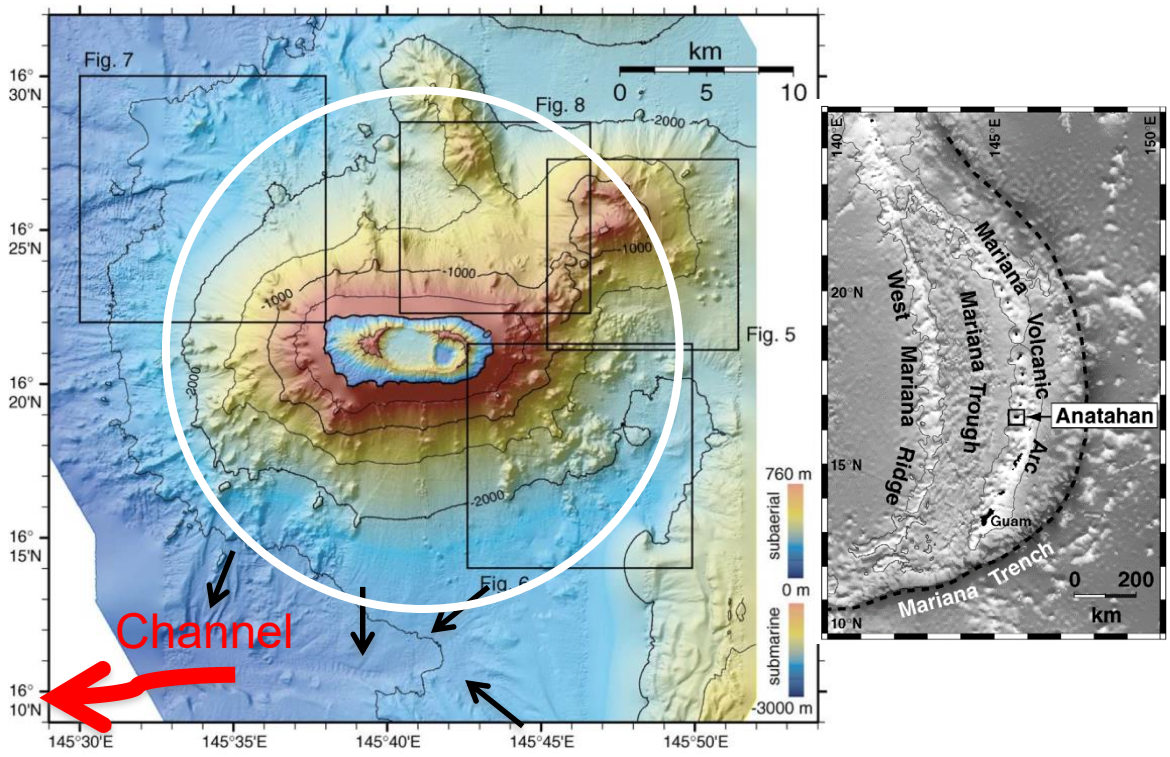

Figure 32

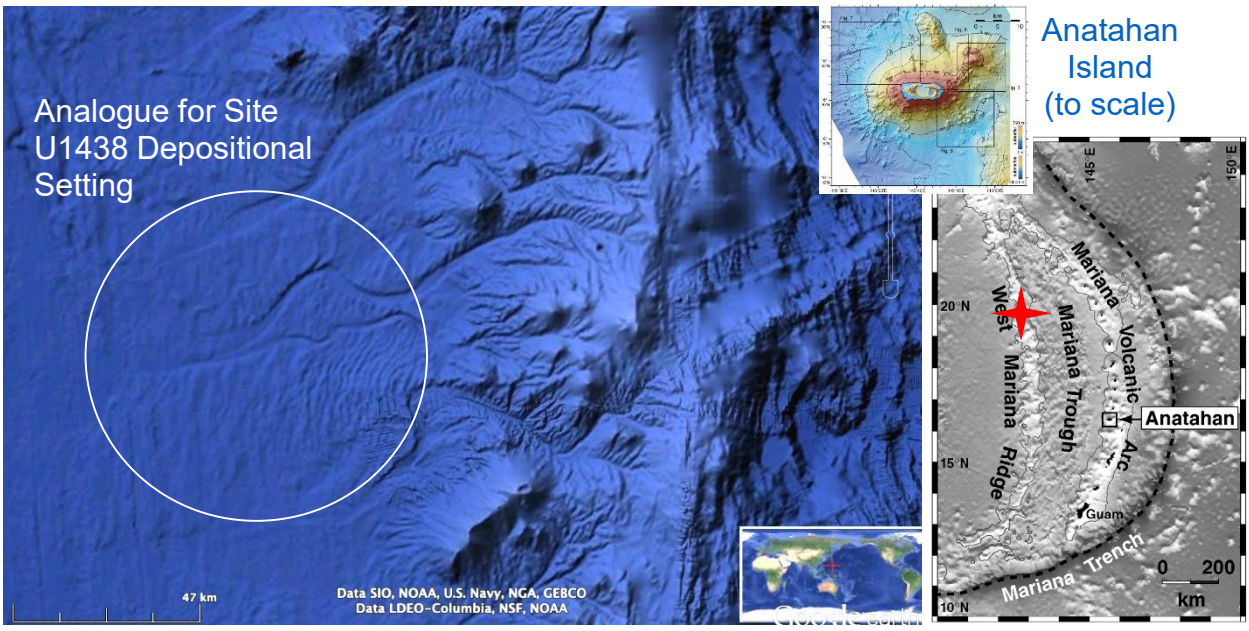

Figure 33

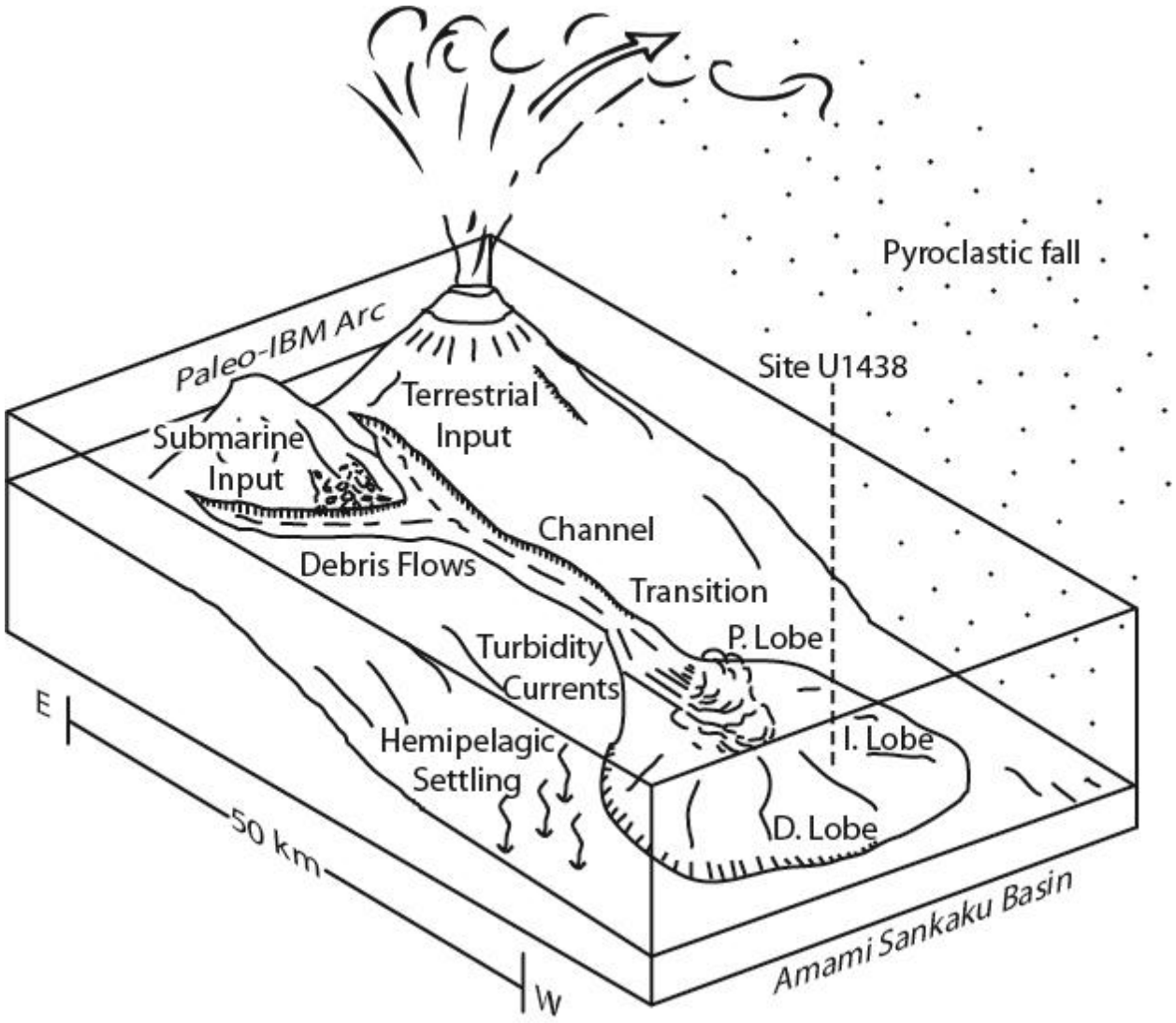
Pyroclastic fall
Paleo-IBM Arc
Site U1438
Terrestrial
Input
Submarine
Input
Channel
Debris Flows
Transition
P. Lobe
Turbidity
Currents
I. Lobe
Hemipelagic
Settling
D. Lobe
E
50 km
W
Amami Sankaku Basin

Figure 34

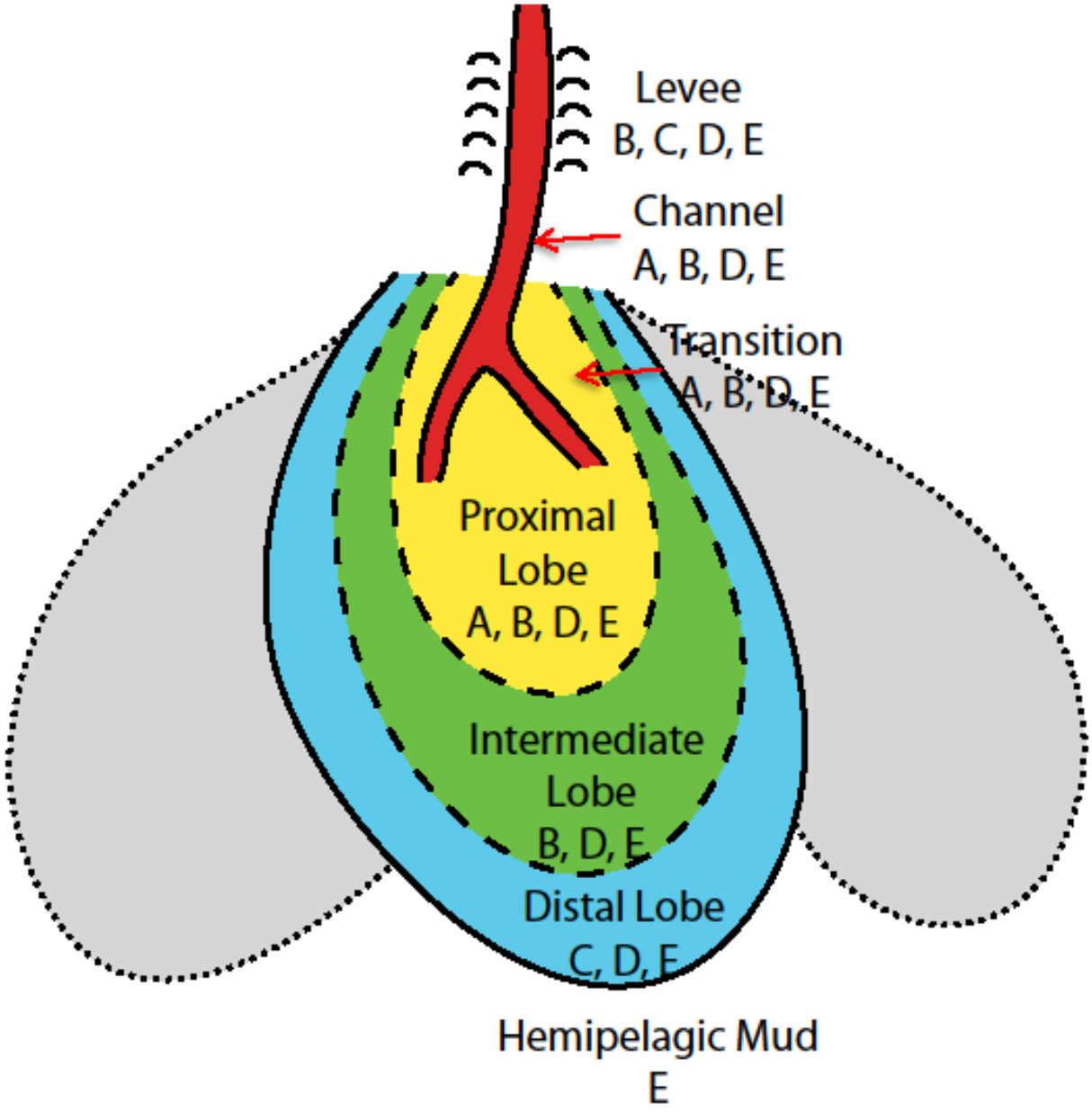
Levee
B, C, D, E
Channel
A, B, D, E
Transition
A, B, D, E
Proximal
Lobe
A, B, D, E
Intermediate
Lobe
B, D, E
Distal Lobe
C, D, E
Hemipelagic Mud
E

Figure 35

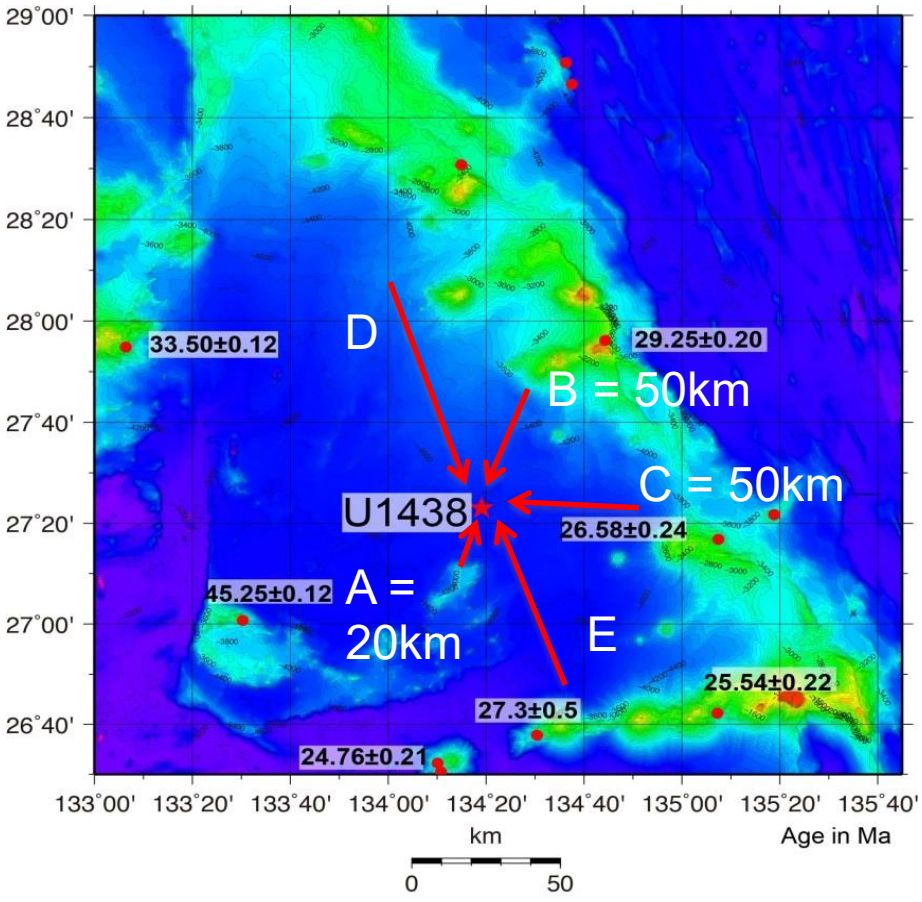
29°00'
28°40'
28°20'
28°00'
27°40'
27°20'
27°00'
26°40'
133°00'
133°20'
133°40'
134°00'
134°20'
134°40'
135°00'
135°20'
135°40'
km
0
50
Age in Ma
33.50±0.12
29.25±0.20
26.58±0.24
45.25±0.12
25.54±0.22
27.3±0.5
24.76±0.21
U1438
D
B = 50km
C = 50km
A = 20km
E

Figure 36

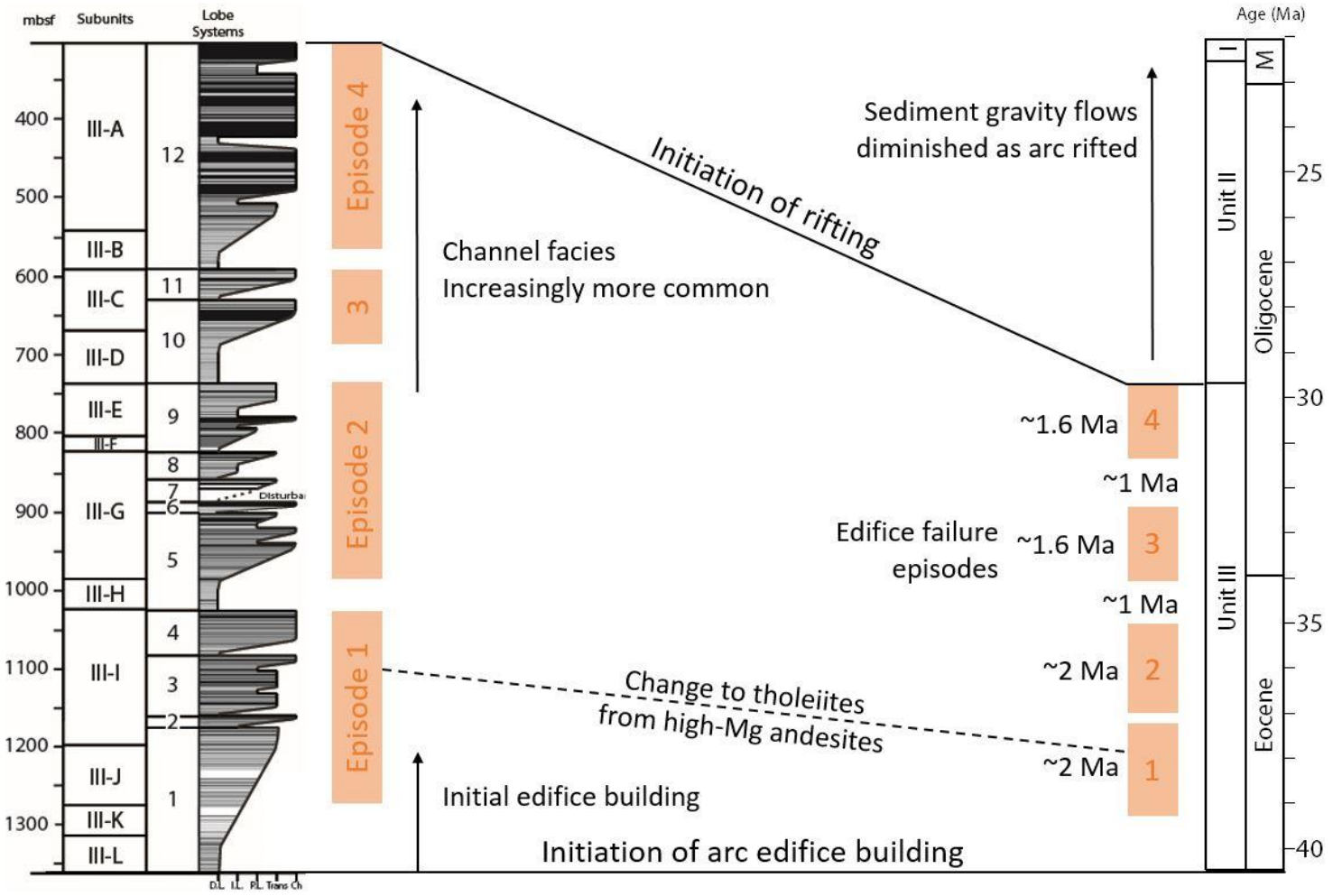
mbsf
Subunits
Lobe Systems
400
500
600
700
800
900
1000
1100
1200
1300
III-A
III-B
III-C
III-D
III-E
III-F
III-G
III-H
III-I
III-J
III-K
III-L
12
11
10
9
8
7
6
5
4
3
2
1
Episode 4
3
Episode 2
Episode 1
Channel facies
Increasingly more common
Initiation of rifting
Sediment gravity flows
diminished as arc rifted
~1.6 Ma
4
~1 Ma
Edifice failure
episodes
~1.6 Ma
3
~1 Ma
~2 Ma
2
Change to tholeiites
from high-Mg andesites
~2 Ma
1
Initial edifice building
Initiation of arc edifice building
Age (Ma)
I
M
Unit II
Unit III
Oligocene
Eocene
25
30
35
40

Figure 36

APPENDIX C: TABLES

Class	Description	Class	Description
A1.1	Disorganized gravel	C2.4	Sand and mud couplets, 80% mud
A1.4	Disorganized pebbly sand	D1.1	Structureless silt
A2.7	Graded pebbly sand	D2.4*	Laminated silt
B1.1	Disorganized sand	D2.5*	Silt with sandy injections
B2.1	Parallel-stratified sand	E1.1	Structureless mud
B2.2	Cross-stratified sand	E1.2	Varicolored mud
C2.1	Sand and mud couplets, >30cm	E2.1	Graded mud
C2.2	Sand and mud couplets, 10-30cm	E2.2	Laminated mud
C2.3	Sand and mud couplets, <10cm		

Scheme modified from Pickering et al. (1986). * = Facies classes created for this study. See text for additional information.

Table 1

Designator	Thickness	Name
1	0-1 cm	Lamination
2	1-3 cm	Very thin bed
3	3-10 cm	Thin bed
4	20-30 cm	Medium bed
5	30-100 cm	Thick bed
6	> 100 cm	Very thick bed

Designator	Max Grain Size
M	Mud
Si	Silt
S	Sand
G	Gravel

Table 2

Site U1438			Age (Ma)		Depth (mbsf)							Dep. Rate (m/Myr)
Hole	Unit	Subunit	top	bottom	top	bottom	Hole/Core	Lithologies	Facies Classes	Thicknesses	Depositional Units	
Hole A/B	I		0	22.5	0	160.25	A1H-B17H	Mud			Hemipelagic Mud and Ash	7.1
Hole B	II	II-A	22.5	26.5	160.25	199.1	B18H-B25X	Mud and ash	E1.1 with minor B1.1 and B2.1	Disturbed	Hemipelagic Mud and Ash	9.7
		II-B	26.5	28	199.1	237.9	B25X-B29X	Mudstone, Siltstone	E1.1, D1.1	Disturbed	Hemipelagic Mud, Turbidites, and Ash	25.9
		II-C	28	29.5	237.9	309.55	B29X-D12R	Mudstone, Sandstone	E1.1, D1.1	Disturbed	Fine-Grained Turbidites and Minor Medium-Grained Turbidites	47.8
Hole D	III	III-A	29.5	31.1	309.55	541	D12R-D36R	Conglomerate, Sandstone, Siltstone	A with minor B and D	10cm to 50cm and >100cm, One 20m	Debrites and Fine- and Medium-Grained Turbidites	144.7
		III-B	31.1	32	541	583.11	D36R-D40R	Mudstone, Siltstone, Sandstone	D, E, B1.1, B2,1	<30cm	Fine- and Medium-Grained Turbidites	46.8
		III-C	32	33.5	583.11	665.16	D40R-D49R	Conglomerate, Sandstone, Siltstone	A, B, D2.5, D2.4	<100cm and One 16m Bed	Debrites with Fine- and Medium-Grained Turbidites	54.7
		III-D	33.5	34.8	665.16	743.2	D49R-D57R	Siltstone, Sandstone	D2.5, B1.1, B2.1	10cm to 75cm	Fine-, Medium-, and Coarse-Grained Turbidites	60.0
		III-E	34.8	35.6	743.2	809	D57R-D63R	Conglomerate, Sandstone, Siltstone	A, B, D	<30cm to >100cm	Debrites with Fine- and Medium-Grained Turbidites	82.2
		III-F	35.6	36	809	831.2	D64R-D66R	Sandstone, Siltstone	D2.5, B1.1	<10cm to >30cm	Medium-Grained Turbidites	55.5
		III-G	36	37.1	831.2	983.5	D66R-E16R	Conglomerate, Sandstone, Siltstone	A, B with minor C, D, E	<10cm to >100cm	Debrites with Fine- and Medium-Grained Disturbed Turbidites	138.5
Hole E		III-H	37.1	37.4	983.5	1034.5	E16R-E21R	Siltstone, Sandstone	D with minor A, B	10cm to >50cm	Fine- and Medium-Grained Turbidites	170.0
		III-I	37.4	37.75	1034.5	1202.7	E21R-E38R	Conglomerate, Sandstone, Siltstone	A, B	30cm to >50cm	Debrites with Fine-, Medium-, and Coarse-Grained Turbidites	480.6
		III-J	37.75	39.5	1202.7	1283	E38R-E47R	Mudstone, Siltstone, Sandstone	E with minor B, C, D, E	10cm to >50cm	Fine- and Medium-Grained Turbidites with Ash/Lapillistone	45.9
		III-K	39.5	40.5	1283	1312	E47R-E50R	Mudstone, siltstone, sandstone	B, C, D, E	>30cm	Fine- and Medium-Grained Turbidites with Ash/Lapillistone	29.0
		III-L	40.5	41.5	1312	1361.9	E50R-E55R	Sandstone, Mudstone	C2.2, C2.3	10cm	Fine- and Medium-Grained Turbidites	49.9
	IV	IV-A	41.5	45.5	1361.9	1405.9	E56R-E61R	Mudstone			Turbidites with Ash	11.0
		IV-B	45.5	54	1405.9	1453.7	E61R-E67R	Mudstone, Sandstone			Medium- and Coarse-Grained Turbidites	5.6
		IV-C	54	55	1453.7	1459.3	E68R	Mudstone			Turbidites with Hemipelagic Mud	5.6
											Unit III Average	113.1
											Debrite-Rich Average	180.1
											Debrite-Poor Average	71.3

Table 3